High-speed MSM photomixers for spectroscopy applications

Moreno-Losana, Antonio

Award date:
2006

Awarding institution:
University of Bath

High-Speed MSM Photomixers for Spectroscopy Applications

Antonio Moreno-Losana

A thesis submitted for the degree of Doctor of Philosophy
Department of Physics
University of Bath
September 2006

ProQuest LLC
789 East Eisenhower Parkway
P.O. Box 1346
Ann Arbor, MI 48106-1346

to my parents, my brothers and my friends

Acknowledgements

I would like to thank my family and all the people in the Physics department and outside it that helped me with their technical and personal support to complete this PhD. I would also like to acknowledge EPSRC for their financial support.

Abstract

Coherent Raman Electron Spin Resonance (CRESR) is an optical spectroscopy technique that relies on an optical heterodyne detection system for the accurate estimation of the gyro-magnetic ratios of electrons in semiconductor and biological samples. The use of higher frequencies leads to an enhancement in the resolution of the system. Due to the limited availability of commercial photodetectors at frequencies higher than 50 GHz, the aim of this project was to develop detectors for operation up to 200 GHz.

In this thesis the successful development of various families of MSM photomixers has been presented. Modelling for the estimation of the optimum dimensions of different MSMs for operation at frequencies up to 50 GHz was performed. Various fabrication processes were developed and optimised for improving the yield and the repeatability of the method, as well as reducing dramatically the amount of material required (and therefore the cost). Such prototypes were successfully used for the determination of the g-factors of a diluted ruby sample in the CRESR spectroscopy experiment.

Modelling and fabrication processes for monolithic and non-monolithic prototypes were developed for operation at 100 GHz and 200 GHz. Two different lines of research for the optimisation of devices were explored: membrane-supported / thin-film device structures and buried metallic contacts. The advantages of membrane devices are lower capacitance and the possibility of back illumination (improvement of external quantum efficiency by avoiding shadowing effects). The buried contacts reduce the spread in the travelling distance of carriers generated at different depths and improve the quantum efficiency allowing collection of carriers generated deeper within the semiconductor. As was demonstrated, such improvements were achieved without incurring a degradation of the dark current and the capacitance of the devices.

Table of contents

Chapter 1

Introduction

Photodetectors have been the subject of intense research over the past decades for a broad range of applications in optical networks, spectroscopy, astrophysics and telecommunications. The work described in this thesis comprises the development of high-speed photomixers for their application in spectroscopy, particularly for its implementation in a Coherent Raman Electron Spin Resonance (CRESR) experiment.

CRESR is an optical spectroscopy technique developed in the University of Bath by the Optical Spectroscopy group that relies on an optical heterodyne detection system for measuring the coherent changes induced in a Raman scattered laser beam at magnetic resonance. Such a system, operating at frequencies up to 34 GHz has been successfully applied in the estimation of the gyro-magnetic ratios of semiconductor and biological samples. As will be demonstrated in the following chapter, the use of higher frequencies leads to an enhancement in the resolution of the system. The aim of this project was the development of photodetectors for operation at frequencies up to 200 GHz given the unavailability of commercial detectors at such frequencies.

This work focused in the design, modelling, fabrication and testing of Metal-Semiconductor-Metal (MSM) photomixers. The first three sections of Chapter 2 cover the theoretical background of semiconductor physics, photodetection and mixing theory. The last two sections of Chapter 2 analyse in detail the CRESR system and provides an introduction to MSM photodetectors. Chapter 3 is the literature review of MSM PDs from early developments to advanced applications. In Chapter 4 all the fabrication techniques developed during the course of the research are introduced. In Chapter 5 a detailed description of the development monolithically integrated MSMs for operation at frequencies up to 60 GHz are presented. One of the fabricated prototypes was successfully used in the CRESR system at 33 GHz for the analysis of a diluted ruby sample.

Chapters 6 and 7 present the two families of prototypes for high speed operation, namely monolithical and non-monolithical. The difficulties that arose when developing the fabrication process for monolithical prototypes motivated the development of non-monolithical prototypes. The fabrication processes for the three families of prototypes were developed including features for optimising the MSMs, maximising the yield and minimising the waste of material.

Chapter 8 covers the development of membrane-supported and thin-film MSMs. Such type of devices presents two main advantages: firstly the reduced capacitance, improving the frequency response; and secondly the possibility of back illumination of the MSM, improving the quantum efficiency. In Chapter 9 the conclusions of the research are presented together with a concept MSM including many of the optimisation features considered during the project.

Chapter 2

Theoretical Background

This chapter covers an introduction to all the basic theory required for the understanding of the concepts used throughout this thesis. The first section is an overview of some basic semiconductor physics, including optical absorption, carrier transport and the continuity equation. Section 2.2 covers an analysis of the three most prominent photodetectors, namely photoconductor, photodiode and Schottky barrier photodiode. Section 2.3 analyses how the characteristics of the photodiodes result in the photomixing effect in these devices and some basic mixer configuration and noise considerations. Section 4 reviews the CR ESR spectroscopy system, the original motivation for this research, and the role of the photomixers developed in such setup. Finally, Section 5 is an introduction to metal-semiconductor-metal photomixers and a basic analysis for understanding their performance. The subject matter covered in the first three sections is standard text book material, a bibliography is included in Appendix 1.

2.1 Introduction to semiconductor physics

A semiconductor is a crystalline structure in which a unit cell is repeated in all directions (ideally, if defects are not taken into account). In the Kronig-Penney model, each of the atoms in the crystal structure is assigned a potential box. This model results in some bands of allowed energy states, separated by bands of forbidden energies.

In solids, the lower bands are full and the two higher bands are called *valence* and *conduction* band; the difference between the valence and the conduction bands is referred as the *energy bandgap*. The electrons in the lattice that have energy enough to be in the conduction band are free to move around the crystal contributing to the conductivity of the material.

The probability of a particular energy level E being occupied by an electron in a solid $F(E)$ is represented by the Fermi-Dirac distribution:

$$F(E) = \frac{1}{\exp((E - E_F)/kT) + 1}, \tag{2.1}$$

where k is the Boltzmann constant and T the temperature. The Fermi level E_F is the energy level below which all states are occupied and above which all levels are empty at absolute zero temperature. The Fermi level is a very important concept that will be used later on in the discussion. In an intrinsic semiconductor the Fermi level lies just in the middle of the bandgap, between the valence and the conduction band.

Consider now a group IV semiconductor that is doped with group V atoms. It will be an n-type semiconductor as there is an excess of electrons in the system. Such excess will make the Fermi level to get closer to the conduction band. On the other hand, if the semiconductor is doped with atoms of the group III, there will be a deficit of electrons in the system, as they will fill the holes of the atoms of the dopant. Therefore, in this case the Fermi level will get closer to the valence band.

In a semiconductor there are three basic types of interaction between the photon and the electron. These are absorption, spontaneous emission and stimulated emission.

2.1.1 Optical Absorption and Carrier Generation

Optical absorption is the type of light-semiconductor interaction that photodetection makes use of. Consider the simple model of a semiconductor with two energy levels taking part in the process; the photon simply promotes an electron from the lower energy band to the upper, creating a electron-hole pair. This phenomenon will occur only if the photon has the same or higher energy than the energy gap between the levels.

Now assume that the semiconductor is illuminated by photons of energy ($h\nu$) greater than the energy gap E_g and photon flux ϕ_o (number of photons per unit area per unit time). As the light travels through the material a fraction of light will be absorbed.

This fraction will be proportional to the intensity of the incident light, consequently the absorbed photons in a differential distance Δx will be equal to $\alpha\phi(x)\Delta x$. Using the condition of continuity of the photon flux with respect to the distance travelled by the photons, Eq.(2.2) is obtained:

$$\frac{d\phi(x)}{dx} = -\alpha\phi(x), \tag{2.2}$$

where α is the absorption coefficient. Applying the boundary condition of absorption, the photon flux in the illuminated surface of the material (x=0) is ϕ_0, the differential equation can be solved, giving as solution Eq.(2.3):

$$\phi(x) = \phi_0 e^{(-\alpha x)}. \tag{2.3}$$

The absorption coefficient is function of the wavelength. Figure 2.1 shows this dependence for different semiconductors:

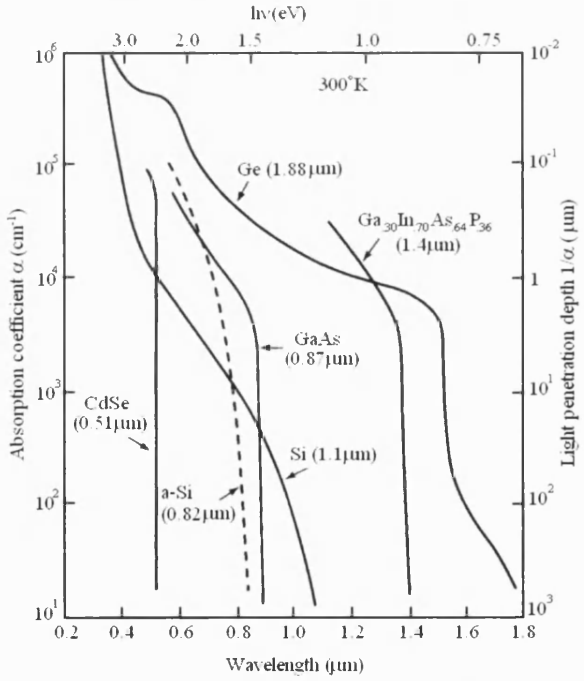

Figure 2.1 Optical absorption coefficient vs. wavelength for different semiconductors, the cut-off wavelength is indicated between parenthesis [1].

It is important to note that the absorption coefficient decreases drastically for frequencies smaller than the energy bandgap; this frequency is called the *cut-off* frequency. For higher frequencies all the light will be absorbed with less depth as α increases. It will be seen later on how this absorption at different depths is one of the key factors in photodetector design.

The *generation rate* per unit volume is defined as the number of carriers generated within the material per second. If the incident optical power density is P_{opt}, the photon flux will be given by:

$$\phi = \frac{P_{opt}}{h\nu}. \tag{2.4}$$

where h is the Plank constant. If those photons have higher energy then the energy bandgap, and assuming that each photon generates one electron-hole pair when absorbed in the semiconductor, the generation rate can be approximated:

$$G = \phi\alpha = \frac{\alpha P_{opt}}{h\nu}. \tag{2.5}$$

The excited state of the electron described above is unstable. That is, after a short time, the electron will recombine with the hole emitting a photon with the energy of the energy gap between levels. This process is called *recombination*, and the *recombination rate* is the number of carriers that fall to the lower level per second. This leads to the concept of *carrier lifetime*, which is defined as the average time that a carrier can survive in a semiconductor before recombining.

2.1.2. Carrier Transport

2.1.2.1 Drift transport:

Consider a n-type semiconductor; the extra electrons will be moving randomly inside the bulk of the semiconductor colliding with each other in such a way that the total average velocity is zero. The average distance and time between collisions are the *mean free path (l)* and the *mean free time* (τ_c). When an electric field ($\mathcal{E}$, in general a vector quantity) is applied across the semiconductor, the net velocity will be aligned

with the direction of the field. This component to the velocity is called *drift* (v_n). The drift velocity can be obtained by a balance equation of momentum of the electron as shown in Eq.(2.6):

$$-q\,\mathcal{E}\,\tau_c = m_n\,v_n\,, \tag{2.6}$$

where the left side of the equation is the momentum given by the field, and the right part the momentum gained by the carriers. Thus, the velocity is proportional to the applied field by a proportionally factor of $q\tau_c/m_n$. Defining such factor as the *electron mobility* (μ_n) the equation is rearranged:

$$v_n = \mu_n\,\mathcal{E}. \tag{2.7}$$

This linear relationship between mobility and carrier velocity is valid for moderate applied fields. For some semiconductors, like Si and Ge, the electron velocity saturate at high fields (typically of the order of 10^4 V/cm) see Figure 2.2. For others, like GaAs, the carrier velocity reaches a maximum and then decreases for higher fields. This phenomenon is due to its band structure, that allows conduction electrons to be transferred to a low mobility higher energy satellite valley.

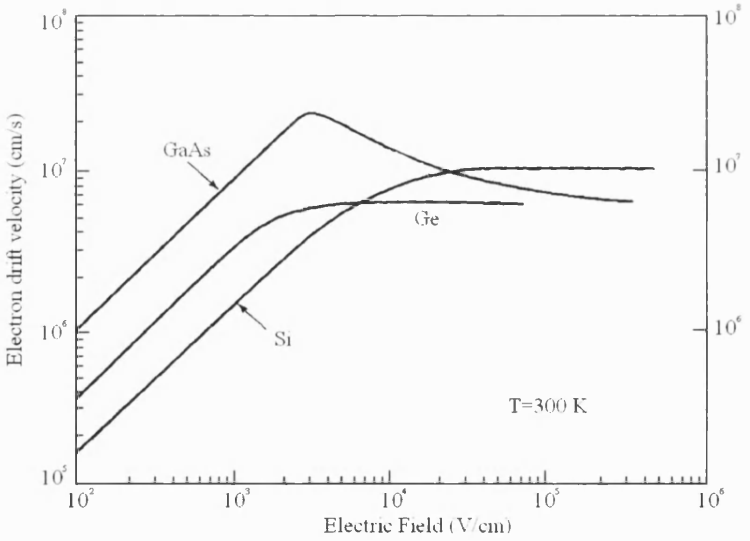

Figure 2.2 Drift velocity of electrons as function of external applied field for different semiconductors after [2] [3] [4].

The mobility is a parameter that governs how freely the electrons or holes can move in the direction of the applied field and it is strongly related to the scattering processes that occur during the drift of the electrons. Those scattering processes are mainly *lattice scattering* and *impurity scattering*. The former is due to thermal vibration and the latter is due to electrons travelling past an ionised dopant impurity. Then the mobility can be expressed as:

$$\frac{1}{\mu} = \frac{1}{\mu_l} + \frac{1}{\mu_i}, \tag{2.8}$$

where μ_l and μ_i are the mobility components due to impurity and lattice scattering. In samples with low concentration of impurities, the lattice scattering dominates, meanwhile for heavily doped samples, the impurity scattering is more dominant at low temperatures where the vibration of the lattice is lower.

The next step in our discussion is to analyse the current flow due to the drift, referred as *Drift Current*. Consider again a slab of semiconductor of area A, length l, with an applied field $\mathcal{E}$. The electron and hole current density (J, in general a vector quantity) will be:

$$\begin{aligned} J_n &= \mathrm{q}\, n\, \mu_n \mathcal{E}, \\ J_p &= \mathrm{q}\, p\, \mu_p \mathcal{E}, \end{aligned} \tag{2.9}$$

where q is the charge, n and p are the number of carriers per unit volume and μ_n and μ_p are the electron and hole mobility respectively. Therefore, the total current density will be the sum of both currents:

$$J = J_n + J_p = q\,(n\,\mu_n + p\,\mu_p)\,\mathcal{E}. \tag{2.10}$$

And defining the conductivity as shown in the equation:

$$J = \sigma\,\mathcal{E} \rightarrow \sigma = \mathrm{q}\,(n\,\mu_n + p\,\mu_p). \tag{2.11}$$

Note that the above discussion is only applicable for moderate applied electric fields. For the case of high applied fields (>100 kV/cm) the semiconductor suffers a breakdown due to a higher number of carriers that can participate in conduction. This effect has two different origins: impact ionization and Zener tunnelling. A more detailed description of these effects can be found in the Appendix.

2.1.2.2 Diffusion transport:

The diffusion transport is due to a variation in the concentration of carriers within the semiconductor. Those carriers will tend to move from regions with high densities to regions with lower density.

Consider a semiconductor at constant temperature, the electron density at different depths is shown in Figure 2.3. Because of the finite temperature the carriers at the position x=0 will have a thermal velocity (v_{th}) and a *mean free path* (l). Consider the electrons that are in x = -l; they will have equal probability of moving left or right, therefore half of them will move across x=0.

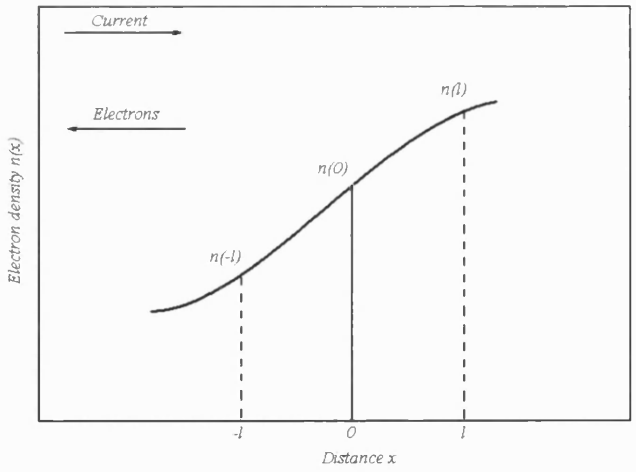

Figure 2.3 Electron concentration vs. distance, where l is the mean free path.

Hence, the average rate of electrons crossing x=0 from left to right and from right to left are F_1 and F_2 respectively, and the total current flow will be the difference:

$$F_1 = n(-l)\, v_{th} / 2 \quad \rightarrow F = F_1 - F_2,$$
$$F_2 = n(l)\, v_{th} / 2. \tag{2.12}$$

Defining the *diffusivity* as $D_n = v_{th} l$, the *diffusion current* for electrons is obtained:

$$J_n = -q F = q D_n (dn / dx). \tag{2.13}$$

Now that drift and diffusion processes have been analysed, the total current density due to diffusion and drift mechanisms is expressed for electrons and holes is given by the equations:

$$J_n = q \mu_n \mathcal{E} + q D_n (dn / dx),$$
$$J_p = q \mu_p \mathcal{E} + q D_p (dp / dx). \tag{2.14}$$

2.1.2.3 Continuity Equation:

The *continuity equation* is the equation that condenses the described mechanisms of *generation, recombination, drift* and *diffusion*. Consider the slice of semiconductor shown in Figure 2.4:

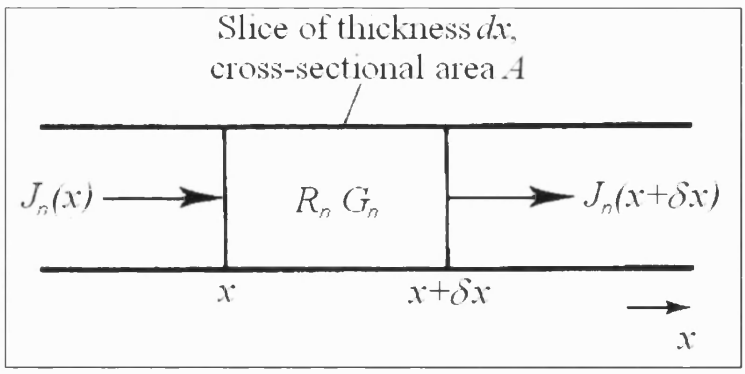

Figure 2.4 Current flux within a slab of semiconductor.

The expression for the net carrier density can be obtained by taking into account the number of carriers flowing into the slice, flowing out of the slice, carriers generated within the slice and carriers recombining in the slice. Applying the continuity condition to the flow of carriers, the following equation is obtained for electrons:

$$\frac{\delta n}{\delta t}\mathrm{d}x = \left[\frac{J_n(x+\mathrm{d}x) - J_n}{\mathrm{q}}\right] + (G_n - R_n)\mathrm{d}x, \qquad (2.15)$$

where G_n and R_n are respectively the generation and recombination rates of electrons. Approximating the term $J(x+\mathrm{d}x)$ by Taylor series, the continuity equations are obtained:

$$\frac{\delta n}{\delta t} = \frac{1}{\mathrm{q}}\frac{\delta J_n(x)}{\delta x} + G_n - R_n \qquad \text{for electrons,}$$

$$\frac{\delta p}{\delta t} = \frac{1}{\mathrm{q}}\frac{\delta J_p(x)}{\delta x} + G_p - R_p \qquad \text{for holes,} \qquad (2.16)$$

where G_p and R_p are respectively the generation and recombination rates of holes.

2.2 Photodetection

Photodetectors are semiconductor devices that are able to convert optical signals into electrical signals. There are mainly two types of photodetectors: photoconductors and photodiodes; both are based in the same physical processes of absorption and carrier transport by an external bias, but with some substantial differences. The understanding of the different ways in which photodetection is achieved is necessary for the analysis of the photomixing effect described in Section 3.

2.2.1 Photoconductor

The photoconductor is the simplest design of optical detector, consisting of a slab of semiconductor in which the photons generate electron-hole pairs that are collected by applying an external bias. The photoconductor is connected to the circuit via *ohmic contacts*, that provide little obstacle to the current flow. The basic detection circuit is shown in Figure 2.5:

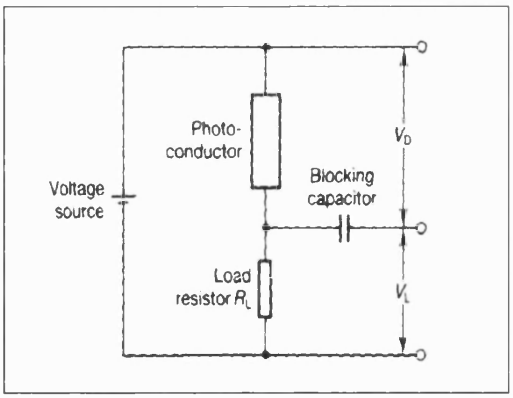

Figure 2.5 Basic Detection Circuit for a Photoconductor.

Consider a n-i-n structure (n-type semiconductor, insulator, n-type semiconductor) where in the illuminated state thermally generated electron-hole pairs are balanced by the corresponding recombination. For detector thicknesses (d) much larger than the penetration depth of the incident light, the generation rate can be expressed in terms of optical power (P_{opt}) and quantum efficiency (η):

$$R = G = \Delta n / \tau_p = \frac{\eta(P_{opt} / h\nu)}{wdl}, \tag{2.17}$$

where R is the recombination rate, G is the photogeneration rate, τ_p is the recombination time and w ,d and l are the dimensions of the slab of semiconductor. The conductivity (σ) for the non-illuminated state is given by Eq.(2.11) which, under illumination will become:

$$\sigma = q\,[\mu_n (n_0 + \Delta n) + \mu_p (p_0 + \Delta p)], \tag{2.18}$$

where Δn and Δp are the excess carrier densities due to illumination and obviously they are equal, as for each photogenerated electron there is a corresponding photogenerated hole. The change in conductance ($\Delta\sigma$) when there is incident energy is the key for the detection mechanism, and it can be obtained by subtracting Eq.(2.11) from Eq.(2.18):

$$\Delta\sigma = q\,\Delta p\,(\mu_n + \mu_p). \tag{2.19}$$

This increase in conductivity (decrease of resistivity) can be related to a change in the current density. In presence of an applied electric field, the photocurrent (I) is expressed:

$$I = JA = q\,\Delta p\,(\mu_n + \mu_p)A\,\mathcal{E}, \tag{2.20}$$

where A ($=wd$) is the cross-sectional area of the semiconductor and the electric field is in the direction of the length of the semiconductor (l). By applying Eq.(2.17) for substituting Δp in Eq.(2.20):

$$I = q\,\tau_p\,G\,(\mu_n + \mu_p)\,A\,\mathcal{E}. \tag{2.21}$$

In the case of moderate bias, the velocity of the carriers is dependent on the applied electric field as was shown in Eq.(2.7). Under these conditions, the transit time of the carriers along the travelling distance l can be expressed as:

$$t_{tr} = l / (\mu_n\,\mathcal{E}). \tag{2.22}$$

Substituting in Eq.(2.21):

$$I = q\,G\,(\tau_p/t_{tr})\,(1+(\mu_p/\mu_n))\,wdl. \tag{2.23}$$

The primary photocurrent is defined as the current that results when each electron-hole pair contributing a single charge to it (gain equal to zero). It is expressed as:

$$I_{pr} = qGAl. \tag{2.24}$$

The gain is defined as the ratio I/I_{pr}, giving:

$$Gain = I / I_{pr} = (\tau_p / t_{tr})\,(1+(\mu_p/\mu_n)). \tag{2.25}$$

For the case of semiconductors where $\mu_p << \mu_n$, the second term of Eq.(2.25) can be approximated to unity, obtaining the simplified expression for the gain:

$$Gain = \tau_p / t_{tr}. \tag{2.26}$$

2.2.2 Photodiode

The photodiode works on the same physical basis as the photoconductor in the sense that it depends on the photogeneration of electron-hole pairs. Instead of a simple slab of semiconductor, the photodiode consists of a p-n junction. The band diagrams of the n-type and p-type are shown in Figure 2.6:

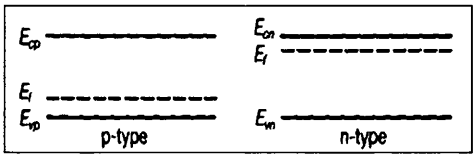

Figure 2.6 Energy band diagrams for p-type and n-type semiconductor.

In Figure 2.6 E_{cp} and E_{cn} are respectively the energy levels of the conduction bands for p-type and n-type semiconductor; E_{vp} and E_{vn} are the energy levels of the valence bands for p-type and n-type semiconductor and E_f is the Fermi level.

When both materials are brought together the majority carriers flow due to the carrier concentration distribution; they redistribute until equilibrium is reached. In such steady state the probability of occupancy of the electrons (and holes) must be constant along the whole device, the energy bands bend as shown in Figure 2.7:

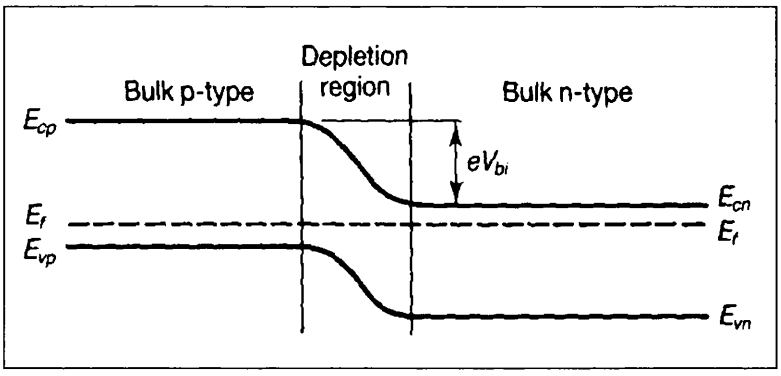

Figure 2.7 Energy band diagram for a p-n junction.

Compared with photoconductors, the most important difference is that the pn diode has a potential barrier. This barrier prevents the diffusion of carriers across the junction except for a small amount that have greater energy than the height of the

barrier. Majority carriers diffuse, being balanced by an equal number of minority carriers that drift due to the built-in electric field across the junction. The result is no net current under zero illumination.

Under illuminated conditions electron-hole pairs can be produced in any of the three regions:

p region (near the barrier)- The hole is immobile due to the potential barrier, but the electron can diffuse to the depletion region. Once in there, due to the internal field, it can drift across the barrier contributing to the signal current or it simply recombines.

n region (near the barrier)- The electron is immobile but the hole can diffuse to the depletion region. It can drift across the barrier contributing to the signal current or it simply recombines.

Depletion region- The electrons and holes drift in opposite directions, contributing both to the signal current.

Now consider an applied voltage across the diode. The *I-V* characteristics of the device is given by Eq.(2.31) and represented in Figure 2.8:

$$I = I_s [\exp (-qV / kT) - 1], \tag{2.31}$$

where I_s is the saturation current, q is the electronic of charge, V is the voltage across the junction, k is the Boltzmann constant and T is the temperature.

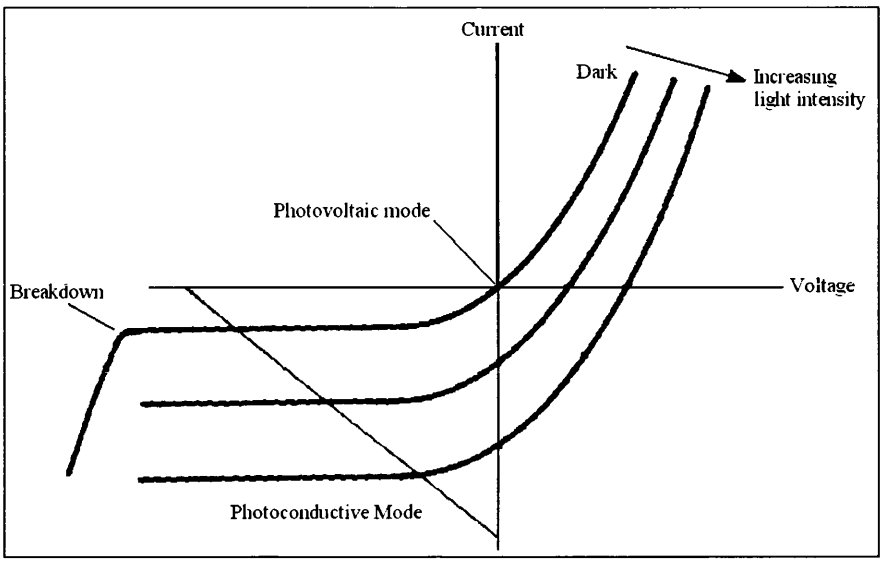

Figure 2.8 Current-Voltage characteristics of a photodiode.

As shown in Figure 2.8 two modes of operation can be distinguished: *Photovoltaic Mode* and *Photoconductive Mode.*

Photovoltaic Mode:

If there is no bias, then the device is said to be operating in photovoltaic mode. The main disadvantage of the photovoltaic mode is that the relation between incident light intensity and the output signal current is not linear. Another disadvantage is that most of the carriers detected are drifting to the contacts so the speed response is generally slow and dependent on the dimensions of the device.

Photoconductive Mode:

If the p-n junction is reversed biased, it is said to be operating in photoconductive mode. Under this condition the potential across the depletion region is increased, which causes an increase in the width of the depletion region. The consequence of this is that the barrier gets higher, thus the resistance across the junction is increased. This can be seen in the band diagram shown in Figure 2.9:

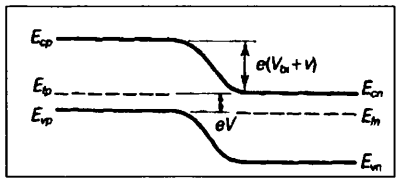

Figure 2.9 Energy band diagram for a p-n diode under reverse bias

One important feature is that the reverse bias prevents carriers from outside the depletion region diffusing across the junction. This means that the mechanism of gain described in Section 2.2.1 for the photoconductor is not possible in this situation. Under reverse bias and increasing the illumination, the curve in Figure 2.8 shifts down producing the linear change in current. The point at which the curve intercepts the voltage axis gives the voltage drop across the open circuit diode. The photoconductive operation results in a faster response than the photovoltaic operation, as the slope is greater and the carriers can cross the region in less time.

2.2.3 Schottky Barrier Photodiode

A Schottky barrier is formed when a semiconductor and a metal are brought together creating a junction region between them. Consider the metal, n-type and band diagram shown in Figure 2.10:

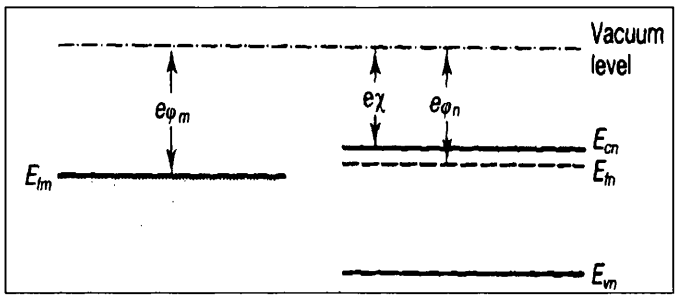

Figure 2.10 Energy band diagram for a metal and n-type semiconductor.

In the figure, $e\varphi_m$ and $e\varphi_n$ represent respectively the workfunctions of the metal and the n-type semiconductor, and $e\chi$ is the electron affinity measured from the bottom of the conduction band.

In the same way that described for the p-n junction, when brought together, electrons will flow from the semiconductor to the metal until the Fermi energies are levelled. In Figure 2.11 the resulting band structure is shown when a metal is brought to contact with an n-type and a p-type semiconductor:

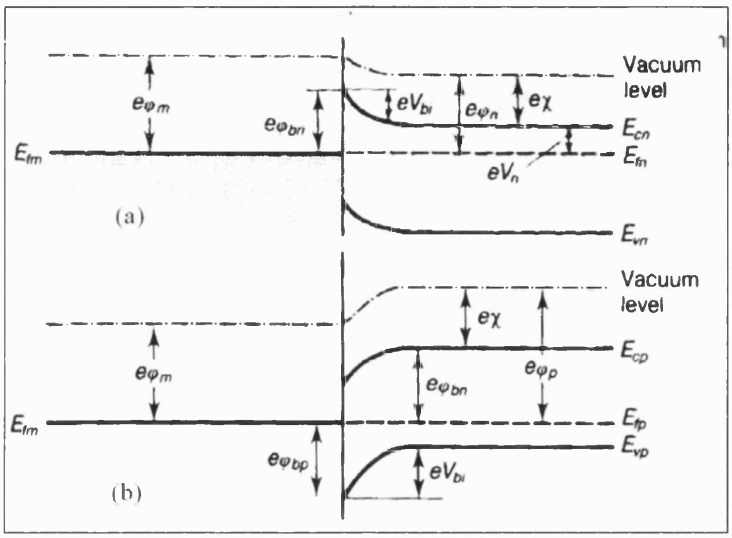

Figure 2.11 Energy band diagrams of Schottky contact between a metal and a) n-type semiconductor b) p-type semiconductor.

In Figure 2.11, the built-in potential of the Schottky contact is represented by V_{bi}. The *Schottky barrier* is defined as the height of the barrier at the metal semiconductor contact, $e\varphi_{bn}$ and $e\varphi_{bp}$ in Figure 2.11, and it is calculated as the energy difference between the semiconductor conduction band and the Fermi level of the metal.

When an external bias is applied to the structure, the relative position of the Fermi level will be altered, consequently changing the bending of the barrier. Consider the case of a p-type semiconductor. For $V_{bias} > 0$ the built-in potential is lowered by the biasing potential meanwhile φ_{bn} is unaltered. In the same way when $V_{bias} < 0$, the built-in potential is raised by the bias and again φ_{bn} is maintained. This can be seen in Figure 2.12:

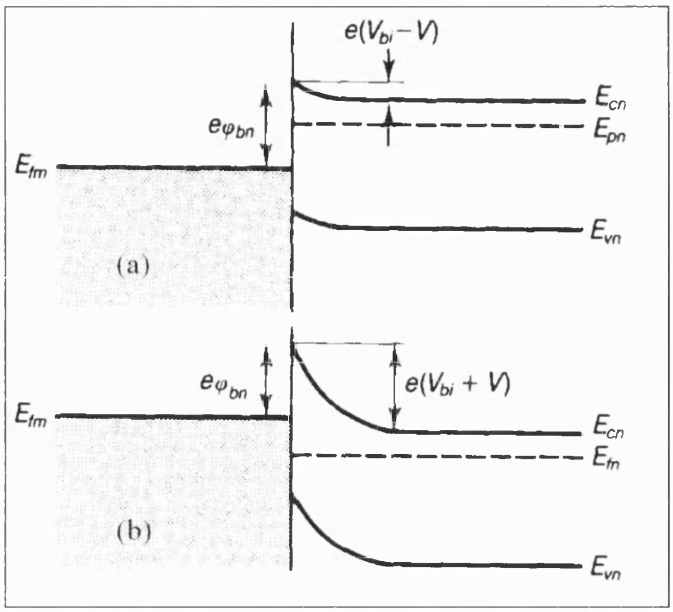

Figure 2.12 Band diagram of the Schottky barrier between a metal and an n-type semiconductor for a) forward bias conditions and b) reverse bias conditions.

The barrier height is a very important parameter, as its size will determine at what applied bias significant conduction will occur.

Due to higher electron mobility, n-type semiconductors are commonly used for Schottky diodes, presenting lower resistance and higher cut-off frequency. This combined with the fact that the depletion region in this device is generally quite thin (<1μm), result in Schottky diodes being able to operate at very high frequencies.

The *I-V* characteristics of the Schottky diode is shown in Eq.(2.32):

$$I = I_s[\exp(-qV / kT) - 1]. \tag{2.32}$$

This equation is identical to the expression for the current density for a p-n junction Eq.(2.31). Such rectifying characteristics, that is, exponential relationship for forward bias and almost constant value of *I* for reverse bias, are the key for mixing signals as will be discussed in the next section.

2.3. Mixer theory

As noted in the previous section the p-n diode and Schottky diode both have rectifying characteristics, Eqs.(2.31) and (2.32), that allow them to perform as mixers by frequency conversion.

Consider a Schottky diode with the voltage $V=V_0+v$ applied across it, where V_0 is the dc bias and v the ac signal voltage. The expression for the current can be expanded in a Taylor series around the dc bias voltage value giving the equation:

$$I(V) \approx I_0 + v\,(dI/dV)\big|_{v0} + v^2/2\,(d^2I/dV^2)\big|_{v0} + \ldots \qquad (2.33)$$

Using just the first three terms is known as the *small signal approximation*. The first derivative can be calculated from Eq.(2.32) giving:

$$(dI/dV)\big|_{v0} = (q/\eta kT)\,I_s \exp(\alpha V_0) = (q/\eta kT)\,(I_0 + I_s) = G_d, \qquad (2.34)$$

where η is the ideality factor and the G_d is known as the *dynamic conductance* of the diode. The second derivative is calculated in the same way, and defining $\alpha=(q/\eta kT)$, it can be expressed as:

$$(d^2I/dV^2)\big|_{v0} = (dG_d/dV)\big|_{v0} = \alpha^2 I_s \exp(\alpha V_0) = \alpha^2(I_0 + I_s) = \alpha\, G_d. \qquad (2.35)$$

Defining $G_d' = \alpha\, G_d$, the small signal approximation expression is rearranged to give:

$$I(V) \approx I_0 + j = I_0 + vG_d + (v^2/2)\,G_d' + \ldots \qquad (2.36)$$

This equation shows how the diode converts a fraction of a radio frequency signal to dc voltage (rectification). Applying the sinusoidal expression for V in the small signal approximation:

$$v = v_0 \cos \omega_0 t, \qquad (2.37)$$

$$I(V) \approx I_0 + v_0\, G_d \cos \omega_0 t + (v_0^2/2)\,G_d' \cos^2 \omega_0 t + \ldots \qquad (2.38)$$

$$I(V) \approx I_0 + (v_0^2/4)\,G_d' + v_0\, G_d \cos \omega_0 t + (v_0^2/4)\,G_d' \cos 2\omega_0 t + \ldots \qquad (2.39)$$

The first two terms are the dc current components; the first is the bias current and the $(v_0^2/4)\ G_d'$ term is the rectified current. The rest of the terms are ac signals at frequencies corresponding to ω_0, $2\omega_0$...

Now consider two signals incident upon the diode at the same time: generally the weaker signal is the *Radio frequency Signal* (RF) and the stronger is the *Local Oscillator* (LO). Consider those signals represented in their sinusoidal form as shown in the equations:

$$V_{RF}(t) = v_{RF} \cos(\omega_{RF} t + \phi_R)), \tag{2.40}$$

$$V_{LO}(t) = v_{LO} \cos(\omega_{LO} t + \phi_L)), \tag{2.41}$$

where ϕ are the phases constant for each signal. Applying these equations to the Taylor series approximation of the diode current, the output will include a dc current plus terms in v, that will give rise to components at the RF and LO frequencies, and terms in v^2 that generate components corresponding to $2\omega_{RF}$, $2\omega_{LO}$, ω_{RF}-ω_{LO} and $\omega_{RF}+\omega_{LO}$, and terms for higher orders of v. Those generated frequencies can be expressed as:

$$\omega = m\ \omega_{RF} + n\ \omega_{LO}, \tag{2.42}$$

where n and m are integers between $-\infty$ and ∞. Most of those frequencies will have negligible power. This is because they correspond to signal generated by terms of the order of v^3 and higher. As the amplitudes of those signals are generally very low with respect to the LO signal, the terms corresponding to v^3 or higher can be neglected. The power distribution for the different frequencies generated in the diode is shown in Figure 2.13:

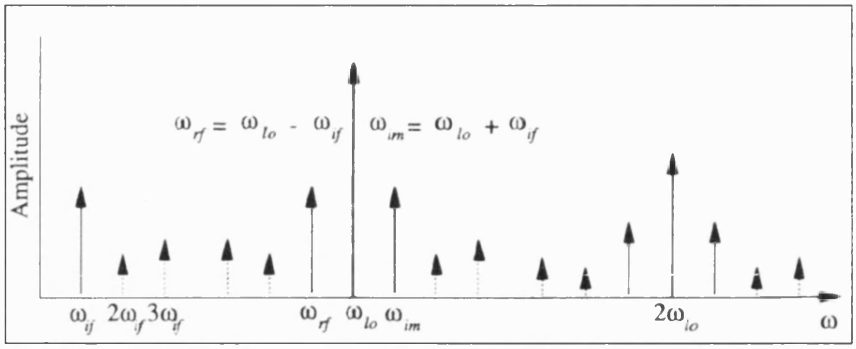

Figure 2.13 Distribution of power of the different frequencies generated in the mixing process where ω_{lo}, ω_{rf} , ω_{IF} and ω_{im} are respectively the local oscillator, radio signal, intermediate and image frequencies.

The difference between the RF frequency and the LO frequency is referred to as the *Intermediate Frequency* (IF):

$$\omega_{IF} = \omega_{RF} - \omega_{LO}. \tag{2.43}$$

From Figure 2.13 it can be seen that there are two different radio frequencies, $(\omega_{LO} - \omega_{IF})$ and $(\omega_{LO} + \omega_{IF})$, that will mix with ω_{LO} to produce an output at ω_{IF}. The signal at $\omega_{im} = (\omega_{LO} + \omega_{IF})$ is termed *image response.*

In practice, the IF output will consist of a signal covering a range of frequencies, centered on ω_{IF}, with a bandwidth determined by that of the IF amplification chain that follows the mixer. The components in frequency corresponding to $\omega_{LO}+\omega_{IF}$ is called *upper sideband*, meanwhile the component in $\omega_{LO}-\omega_{IF}$ is called *lower sideband.* The system can be classified as a *single sideband system* if removal of one sideband is performed or *double sideband system* if it retains both sidebands.

For frequencies of several THz, direct detection of the signal is problematic, but using an heterodyne detection system such high frequencies can be mixed with a reference signal (LO) and converted down to the intermediate frequency (IF). At this lower range of frequencies, there is equipment available to manage the signals. This is the most important feature of mixers, together with their ability of keep spectral information, that direct detectors do not.

A photomixer is a mixer where the LO and RF signals are at optical frequencies. The above description is valid for photomixers with the exception that this type of device cannot support currents at optical frequencies, but can support them at the (millimeter-wave) difference frequency.

An important parameter in mixers performance is the *Conversion Loss*. It is defined as:

$$L = \text{available input RF power / IF output power} \tag{2.44}$$

Typically the LO power must have a value of around 10 dBm to minimize the conversion loss in a mm wave mixer. This power is high enough to invalidate the small signal approximation. Therefore, the non linear equation of the diode characteristics must be solved numerically for precise design and modelling of the mixer.

The power losses in the system can be analysed depending on the physical mechanisms that give rise to them. The main sources of losses are:

-L_0: due to absorption in the diode barrier resistance
-L_H: due to power lost to harmonic sidebands
-L_R: due to power lost due to series resistance
-L_{IF}: due to power lost in reflections at the mixer output

The next step in the mixer analysis is to consider the noise present in the system. Microwave systems have mainly four sources of noise:

1- Johnson noise (also called *thermal noise*). Thermal energy induces a random motion in the carriers in a conductive medium. This random motion will lead to a fluctuation in the current flow. The expression that relates the voltage fluctuation present in a conductive medium of resistance R and within a bandwidth B at temperature T is given by:

$$V_n = (4kTBR)^{1/2}. \tag{2.45}$$

Rearranging this equation, the expression for the noise power is found to be:

$$P_n = v_n^2 / 4R = kTB. \tag{2.46}$$

It is important to point out the characteristics of the distribution of noise within a bandwidth. The noise power for a giving operating temperature and a given bandwidth has a constant value independently of the frequency of operation of the device. This is said to be a *white noise source.*

2- Shot noise. Shot noise is present in devices that operate with carriers having to cross a potential barrier. This mechanism does not present a uniform behaviour, as it is composed of a sum of independent random events. Therefore the average current flowing through the barrier will fluctuate. The value of the noise current for the simple example of a diode dc biased at I_d is given by the equation:

$$J_n = (2\, q\, I_d B)^{1/2}, \tag{2.47}$$

where B is the bandwidth and q is the electronic charge. This kind of noise is again a *white noise* for having a constant value along the spectrum of frequencies.

3- Generation Recombination Noise. The generation-recombination processes that occur in semiconductors also have a random component. The varying number of carriers available in the medium results in a change in the resistivity of the medium and consequently in the current flow. The analysis of the generation –recombination processes responsible for this kind of noise show that it has a constant power spectral density, i.e. it is *white noise.*

4- Flicker Noise. The physical processes involved in the generation of this kind of noise are not yet totally understood. This noise is known as 1/f noise for its dependence on frequency. This dependency on frequency causes the noise power spectral density to have higher values at low frequencies, where it will be the dominant source of noise. At high frequencies, the predominant noise is white noise generated by the processes described before. The frequency in which the flicker noise becomes dominant is known as the *corner frequency.*

An important parameter in mixers is the equivalent *noise temperature.* Consider a real device to consist of an ideal noiseless device in series with a hypothetical matched resistance at the input. The noise temperature is defined as the temperature at which the matched resistance would have to be in order to generate the noise power observed at the terminals of the real device. This noise refers to the noise present in the device itself, obviously the device is not the only element in the system that generates noise.

Consider the simple mixer configuration shown in Figure 2.14:

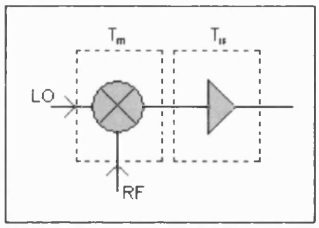

Figure 2.14 Block diagram of mixer and amplifier.

T_{if} is the equivalent noise temperature of the IF amplifier and T_m is the noise temperature of the mixer. If the conversion loss of the mixer is L the noise temperature of the receiver is given by:

$$T_{RX} = (T_m + LT_{if}), \tag{2.48}$$

where T_{RX} is the temperature at the output. If more elements before and after the mixer are considered for calculating their contribution to the noise in the system, the expression will be expanded in the same fashion considering the operating temperature and the losses associated with each element.

The signal power in an optical heterodyne detector is given by [5]:

$$P_{sig}(\omega_1) = 2P_0P_1\,\rho(\omega_1)^2\,R_{eff}, \tag{2.49}$$

where P_0 and P_1 are the power of the LO and RF signals respectively, $\rho(\omega_1)$ is the responsivity at high frequency and R_{eff} is the effective load resistance. In a properly

design optical heterodyne detection system, the dominant source of noise is the amplifier after the photodetector [6] [7]. The contribution to the noise power dissipated in the amplifier input impedance [5]:

$$P_{\text{amplifier noise}} = 290\ \text{k}B\ (10^{N/10}-1) = \text{k}T_E B, \tag{2.50}$$

where B is the bandwidth, N is the amplifier noise figure in dB and T_E is the equivalent excess noise temperature. Consider the simplest of the mixer system configurations, a single ended mixer, where a single diode operates as a fundamental mixer. A block diagram of this kind of mixer circuit is shown in Figure 2.15:

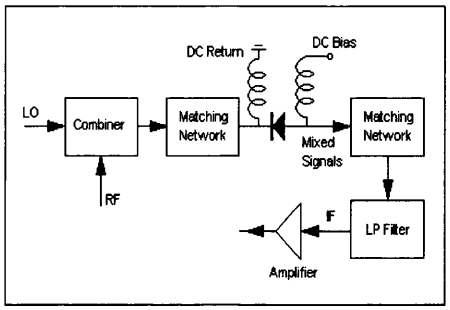

Figure 2.15 Block diagram for a single ended mixer configuration.

The *matching networks* provide the required impedance matching between the combiner and the diode and between the diode and the *Low Pass Filter* in order to minimise the reflection losses of the system. The LP filter is used for removing the high frequency components of the o/p signal generated in the mixing process. Finally, the *IF amplifier* is used for strengthening the signal at intermediate frequency, that is the one that contains the desired information.

The impedances at the input and output of the diode are of fundamental importance. The diode has been previously described as a non-linear device, therefore its resistance and capacitance vary with time when LO input is applied to it. This is the main problem to solve, how to match the source impedance when the device has a time varying impedance.

The equivalent circuit of the diode mixer system can be represented as shown in Figure 2.16:

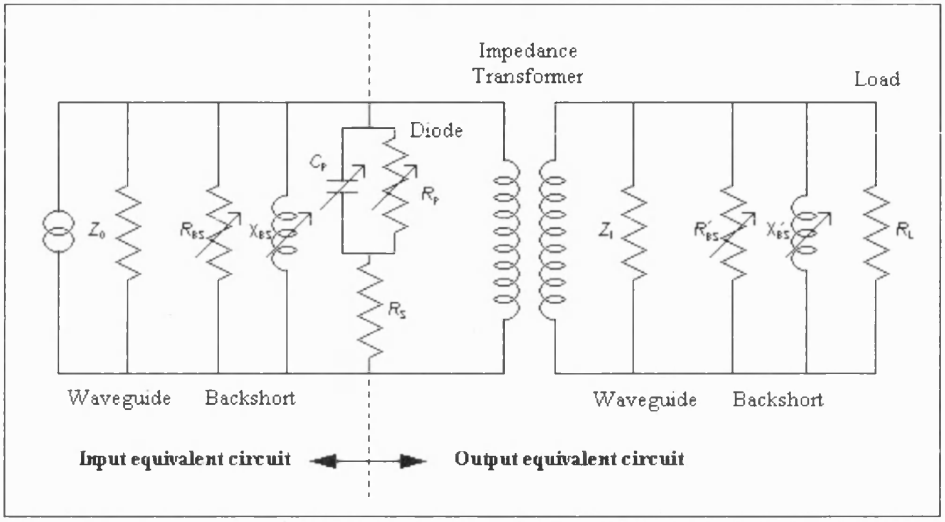

Figure 2.16 Equivalent circuits for input and output of a mixer.

R_p and C_p are the time varying resistance and capacitance of the diode. The capacitance can be considered constant, as its value does not change by as many orders of magnitude as the resistance does. R_s represent the series resistance of the device.

This equivalent circuit must be considered as two independent equivalent circuits that operate at different frequencies. The reason for representing both of them is to illustrate the diode as the link between the input frequencies and the mixed frequencies.

Consider the input circuit that operates at THz frequencies. The input signal is represented as an alternating current that travels through a waveguide of characteristic impedance Z_0. The back short changes the effective length of the waveguide and consequently its resistance (R_{BS}) and impedance (Z_{BS}). From transmission line theory, the relation between Z_0 and Z_{BS} is given by the equation:

$$Z_{BS} = j\, Z_0 \tan \beta l, \tag{2.51}$$

where β is the imaginary part of the propagation constant and l the distance from the back short position to the plane of the diode. From Eq.(2.51), Z_{BS} is purely imaginary for all the values of l. As examples, the value of Z_{BS} is zero for l=0; and Z_{BS}=∞ (open circuit) for $\lambda/4$. The equation shows that the input impedance (Z_{BS}) is periodic in l, repeating for $\lambda/2$.

Therefore, the back short can be tuned to resonate with the capacitance of the diode. This will have the effect of making the most of the current to flow through the diode resistance, and therefore maximising the conversion.

The right hand part of the circuit represents the circuit operating at the intermediate frequency. The impedance transformer represents the matching of the impedance of the diode to the impedance of the output waveguide for good coupling of power. The back short is represented in the same way as that in the input circuit. The waveguide has an intrinsic impedance of Z_I. Again the back short is tuned to maximise the current that flows through the load resistance (R_L) for maximising the power of the mixed signal.

2.4 CR ESR Spectroscopy experiment

The gyro-magnetic ratio (g-factor) is the ratio of magnetic dipole moment to the angular momentum of a particle or a system. It is widely recognised that the behaviour of electrons in condensed matter can be studied through the determination of the g-factors of the material. There are a variety of spectroscopy methods for optically measuring the g-factors. Such techniques rely on the Zeeman effect, where the energy levels are split proportionally to the intensity of the applied magnetic field (B), the Bohr magneton (μ_B) and the g-factor. The main transitions utilised by different spectroscopy methods are shown in Figure 2.17.

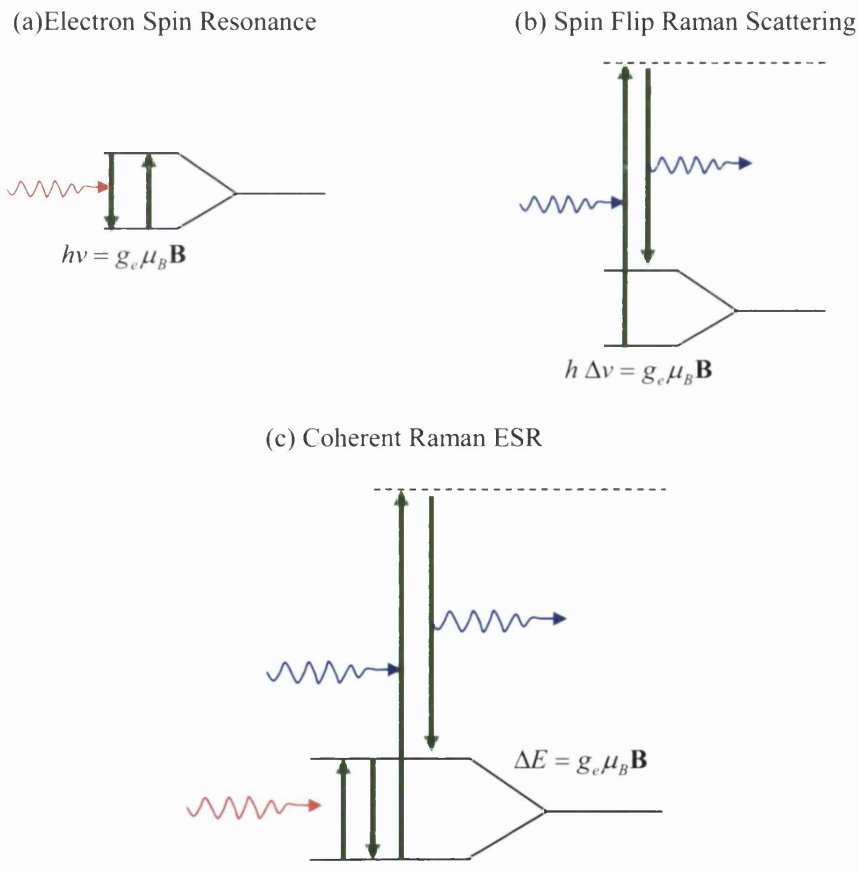

Figure 2.17 Energy transitions involved for (a) Electron Spin Resonance (ESR), (b) Spin Flip Raman Scattering (SFRS) and Coherent Raman Electron Spin Resonance (CRESR) for the estimation of g-factors.

Electron Spin Resonance (ESR) has high resolution [8] (10^{-4} meV in typical semiconductors), but the sensitivity (of the order of 10^{11} spins) is not as high as in Spin Flip Raman Scattering (SPRS) (10^{8} spins). However, SPRS has low resolution [9] [10] determined by the laser linewidth (of about 0.1 meV). Coherent Raman Electron Spin Resonance (CRESR) combines the sensitivity of SPRS with the resolution of ESR.

CRESR is the coherent optical technique for the detection of magnetic resonance with which this project was concerned. This technique, developed by the Optical Spectroscopy Group in the University of Bath [11], relies on an optical heterodyne detection system for measuring the coherent changes induced in a Raman scattered laser beam at magnetic resonance. This technique benefits from the sensitivity of the optical detection together with the spectral resolution of electron spin resonance (ESR). An added advantage of utilising such optical detection setup is the selectivity mechanism that allows the magnetic resonance signals from different centres to be resolved and correlated with the optical transitions, this particularly important for biochemical systems. Bingham *et al.* demonstrated this method, improving the sensitivity up to three orders of magnitude and applied the CRESR to the study of semiconductors [12].

In the first approximation, the g-value of an electron in a conduction-band related state (such as a donor electron) is given by [13]:

$$g = g_0 - \frac{2E_P}{3}\left[\frac{1}{E_0} - \frac{1}{E_0 + \Delta_0}\right], \qquad \text{Eq (2.52)}$$

where, the first term (g_0) is due to the intrinsic spin and the second term is due to orbital angular momentum introduced by spin-orbit coupling (matrix element E_P) between the valence band and the conduction band. E_0 is the bandgap and Δ_0 is the spin-orbit coupling between the top of the valence band and the split-off valence band. It can be seen from this that, if the specimen is strained, the bandgap changes slightly, so that the g-value will also change. However, the strain-induced change in the g-value is small, so that high resolution is necessary.

Consider a certain semiconductor with two donors which are in similar but slightly different environments so that they have similar g-values. If the microwave frequency is ν_1, the splitting of the lower energy level (ΔE) will be the same for both donors (for resonating at the same frequency) and the g-value is slightly different for both donors. Therefore the applied magnetic field for achieving resonance will be different too. The equation for each of the donors is shown:

$$\Delta E_1 = h\nu_1 = g_1^* \mu_B B_1, \tag{2.53}$$

$$\Delta E_2 = h\nu_2 = g_2^* \mu_B B_2. \tag{2.54}$$

From Eqs.(2.53) and (2.54), ΔB can be obtained:

$$\Delta B = B_2 - B_1 = (h\nu_1 / \mu_B) \; [\, (g_1^* - g_2^*) / (g_1^* g_2^*) \,]. \tag{2.55}$$

Note that this expression is valid as the linewidth is determined by hyperfine interactions and does not depend on frequency.

Consider now the same experiment but using a higher microwave frequency of ν_2, resulting in $\Delta B'$ analogous to that shown in Eq.(2.55) The ratio of these expressions gives:

$$\Delta B' = \Delta B \, (\nu_2 / \nu_1). \tag{2.56}$$

The consequence is that if two donors are energetically very close, a sufficiently high microwave frequency must be used to be able to resolve the difference between both donors ($\Delta B'$). In other words, higher frequencies yields a higher resolution of the experiment [12] [14]. Davies *et al.* used commercial photomixers for operation of the CRESR system at 13.5 GHz and 35 GHz [15] [16], but for higher frequencies there was the need to design and construct our own.

The schematic of the experimental arrangement in the CR ESR is shown in Figure 2.18.

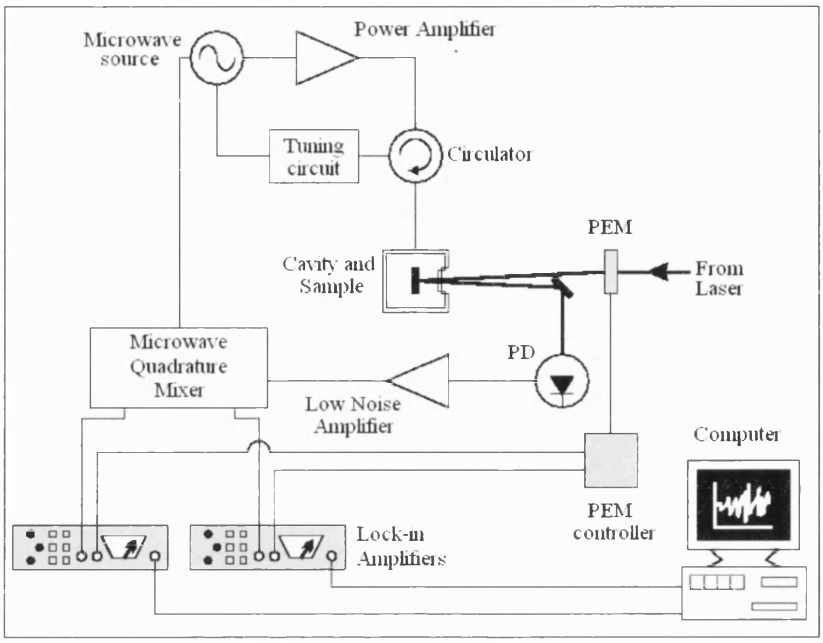

Figure 2.18 Schematic of the experimental arrangement of CRESR spectroscopy system

The sample under study is placed in a resonant microwave cavity accurately aligned with an applied variable magnetic field and illuminated with a laser. When the magnetic field resonates with the microwave excitation the spin-flip scattering becomes coherent. The original signal and the side-band signals mix together in photomixer (PD in the figure) to give an output at the microwave frequency. The photo-elastic modulator (PEM) switches the polarisation of the incoming laser, and the PEM controller ensures that the reference signals are in phase with the output of the photodetector. Each of the channels coming from the output of the quadrature mixer are sensitive to the amplitude and the phase of the signal. The CRESR system output corresponds to the absorption and the dispersion spectrum, each of them incoming from each of the lock-in amplifiers [11]:

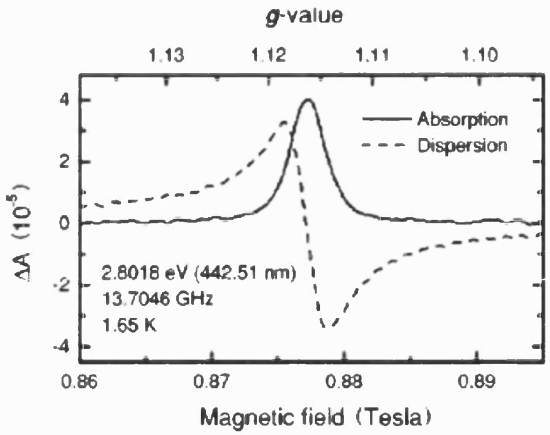

Figure 2.19 Absorption and dispersion components of the CR ESR spectrum for a ZnSe epitaxial layer [11].

The system has been successfully used for characterising semiconductors, for example for the detection of electron paramagnetic resonance of Mn^{+2} ions in CdTe [16]. The optical selectivity of CR ESR technique has allowed the estimation of the strain in different epilayers of ZnSe [11], and the localization of defects in GaN [12]. The system has been applied too for studying biochemical systems, and more in particular to the study of transition metal ion centres in proteins [17].

The Optical Spectroscopy Group built a variety of microwave sources and resonant cavities for their implementation, as well as using commercial photomixers for operation at frequencies up to 32 GHz. The research described in this thesis covers the construction of in-house detectors for operation at frequencies as high as 200 GHz for their utilization in the CR ESR setup. As demonstrated before such frequencies would yield a tremendous improvement in the accuracy of the determination of the g-factor. The detector type that was found most suitable for this application is the Metal-Semiconductor-Metal photomixer.

2.5 Metal Semiconductor Metal photomixers

The MSM photomixer consists of two interdigitated metallic contacts evaporated onto a semiconductor wafer (see Figure 2.20 a), effectively creating two back-to-back Schottky contacts (see Figure 2.20 b). When light is incident on the space between the metallisation it generates electron-hole pairs that are swept out to the external detection circuit by biasing the contact. Such devices have been widely studied in the past decades for their simple and planar structure, their high speed (due to low capacitance per unit area), their low dark current and because of the possibility of monolithic integration with FETs.

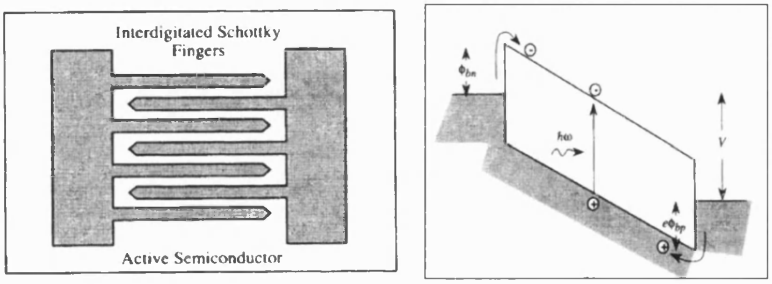

Figure 2.20 a) Top view of MSM structure b) Energy band diagram of MSM

These characteristics have motivated research in MSM devices as integrated optical / millimetre wave converters in optoelectronics. More recently MSM arrays have been applied to communications e.g. broadband optical signal distribution, signal processing and switching. Details of the development of MSMs and various applications are described in detail in Chapter 3.

2.5.1 Frequency response

In principle the three factors that limit the frequency response in MSM devices are the diffusion time (τ_{diff}), the drift time (τ_{drift}) and RC constant (τ_{RC}). The diffusion time becomes an important factor as soon as the volume in which the carriers are travelling is relatively high. But in MSMs, carriers travel distances of the order of a micrometer, so that τ_{diff} is a few orders of magnitude smaller than τ_{drift}, and can be neglected [18]. Therefore a reasonable approximation can be made in considering the time response of the device:

$$\tau \sim (\tau^2_{drift} + \tau^2_{RC})^{1/2}. \quad (2.57)$$

Obviously if the recombination time of the electron-hole pairs in the semiconductor is shorter than the transit time, the term τ_{drift} must be substituted by the average recombination time (τ_{rec}). Therefore, depending on which of the terms in the equation is dominating the time response, the devices are referred to as *transit time limited, recombination time limited* or *RC limited.*

2.5.1.1 Transit time limited devices

In order to model the transport mechanisms in MSM devices, stationary and non-stationary models have been investigated in the past. Non-stationary models using the Monte Carlo method, such as the phenomenological model of transport equations [19], accurately estimate the transit times for different illumination conditions and dimensions. Such models have the main disadvantage of requiring powerful computing facilities and are time consuming.

Stationary models, are much easier to implement numerically, as well as being much more intuitive for understanding the transport mechanisms. The accurate prediction of transport mechanisms in MSM devices was beyond the scope of this project, nevertheless the drift-diffusion model was used for assessing the order of magnitude of the transit times to compare it with the other term of Eq.(2.57).

In the drift-diffusion model the light is assumed to penetrate in the semiconductor, generating electron-hole pairs that drift towards the Schottky contacts solely due to the stationary field created by the bias (see Figure 2.21). For the evaluation of the electric field distribution within the active region of the detector, the conformal mapping technique is generally used, transforming it to a simple parallel plate capacitor model [20].

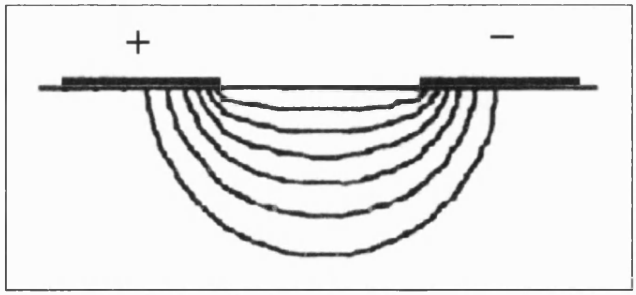

Figure 2.21 Stationary electric field in the semiconductor between the biased contacts

Using the drift-diffusion model the order of magnitude of the average drift time in MSM can be simply estimated as [21]:

$$\tau_{drift} \sim \textit{Drift distance} / (2*\textit{Saturation Velocity}). \quad (2.58)$$

This equation assumes that all the carriers travel at the saturation velocity. In most semiconductors this is achieved at electric fields of the order of 10^4 V/cm as shown in Figure 2.2. As MSM devices have a distance between electrodes of the order of a micrometer, the voltage required is of the order of a few volts. Breakdown, mainly due to avalanche and tunnelling effects, is not a critical limiting factor as it generally occurs at much higher fields than that required to achieve the saturation velocity. Another considerations not included in the drift-diffusion model is that if the applied bias is too high, then some of the carriers will be scattered into satellite valleys of the semiconductor, where their mobility is greatly reduced [22].

The drift distance will depend upon the spacing between fingers and the penetration depth of the light absorbed. Carriers that are generated far away from the surface, will have to travel a longer distance and, consequently, it will take more time for them to be collected. This fact presents a limitation to the frequency response of devices with low optical absorption coefficient at the operating wavelength. Nevertheless, as will be seen in the next chapter, a variety of solutions have been developed to minimise this effect.

The last consideration in the frequency response of transit time limited devices is that due to the difference in mobility between the carriers, the rise time is determined by the flow of the electrons (higher mobility), and a tail in the fall time due to holes (lower mobility).

2.5.1.2 RC limited devices

The RC constant is the time required to discharge the fingers. Fingers with typical sizes in MSMs (under a micrometer) present higher resistance than the value predicted from bulk resistivities due to a higher surface to volume ratio. The stronger scattering processes that occur when electrons are travelling closer to the metal/air boundary are responsible for this effect. This effect is even more pronounced for very narrow fingers (under 100 nm) as the scattering in the semiconductor/metal interface increases [23]. Therefore, it is desirable to thicken, widen and shorten the fingers as much as possible.

The resistance of the device can be calculated using a dc model that considers all the fingers as resistors connected in parallel.

$$R = 2R_0 / N, \tag{2.59}$$

where R_0 is the resistance of each finger and N is the number of fingers connected to each pad. The resistance of the device should not be greater than the resistance of the external load so as not to be a limiting factor for the frequency response of the device. The value at high frequencies may differ from that predicted by the equation due to skin depth effect, but it will remain as a good estimation if the thickness of the metal is less than the penetration depth.

The capacitance of the device is dominated by the capacitance between the fingers. The interdigitated pattern provides a very low capacitance per unit area (of the order of a few fF for a device of active area 10 μm x 10 μm), which is the key factor in the capability of MSM for high-speed application. The expression that gives the capacitance of the MSM structure is given by the equations [24]:

$$C_F = \frac{K}{K'}\varepsilon_0(1+\varepsilon_r)\frac{A}{w+s},$$

$$K = K(k) = \int_0^{\pi/2} \frac{d\phi}{\sqrt{1-k^2\sin^2\phi}},$$

$$K' = K(k'), \quad k' = \sqrt{1-k^2},$$

$$k = \tan^2\frac{\pi w}{4(w+s)}, \tag{2.60}$$

where C_F is the capacitance between the fingers, s is the spacing between fingers, w is the finger width and A is the interdigitated area. This expression can be simplified to give [25]:

$$C_F = 0.226\, N L\, \varepsilon_0(\varepsilon_r+1)\,(6.5\mu^2 + 1.08\mu + 2.37), \tag{2.61}$$

where μ is the ratio of spacing and finger width s/(s+w), N is the number of finger pairs and L is the length of the active area (also referred as *aperture*). This expression shows that in order to reduce the capacitance the fingers must be short and the number of fingers reduced.

2.5.2 Quantum Efficiency

The quantum efficiency is defined in terms of *internal quantum efficiency* and *external quantum efficiency*. The *external quantum efficiency* refers to the portion of light that is absorbed by the semiconductor generating electron-hole pairs. An expression that relates external quantum efficiency and the device dimensions is given by [26]:

$$S = [1-R]\,[s/(s+w)]\,[1-\exp(-\alpha d)], \tag{2.62}$$

where R is the Fresnel reflectivity, w is the finger width, s is the finger spacing and d the thickness of the semiconductor layer and α is the absorption coefficient corresponding to the wavelength of the incident light. The first term of the equation takes into account the fraction of the light impinging on the semiconductor that is reflected. The use of an antireflection coating for reducing this term is described in

detail in Chapter 3. The second term in Equation (2.62) accounts for the portion of the active area covered by the fingers, as the light impinging on the metallisation is reflected; this term is referred to as the *shadowing effect*. The exponential term of the equation refers to the portion of light absorbed in the active region of the semiconductor . Obviously if the wafer is too thin, part of the light will pass through it without being absorbed, affecting to the value of the external quantum efficiency.

Note that the validity of Eq.(2.62) is restricted for incident light with wavelengths comparable or smaller than the finger width. In the case of the finger width being much smaller than the wavelength, the light will not be shadowed by the fingers.

The dependency of the shadowing effect and the optical absorption in the external quantum efficiency is shown in Figure 2.22 [20]:

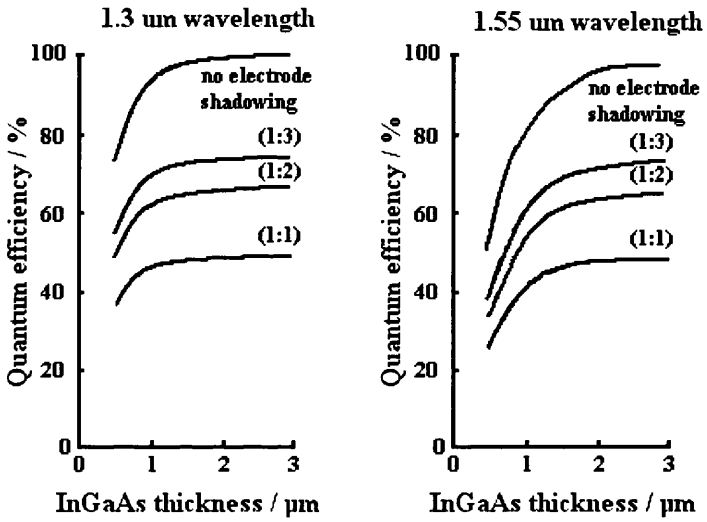

Figure 2.22 External quantum efficiency vs. InGaAs thickness at telecommunication wavelengths for devices of width:spacing ratios indicated between parenthesis [20].

The *internal quantum efficiency* refers to the ratio of carriers generated to carriers collected by the device contacts. Its value depends on the number of carriers that recombine before collection, therefore for achieving internal quantum efficiency close to unity, the transit time must be shorter than the recombination time. Nevertheless, materials with short recombination times can be desirable for

recombination time limited high speed devices as they would ensure that carriers generated far away from the contacts recombine before collection. Therefore this type of device shows better frequency response at the cost of reducing the internal quantum efficiency. The overall quantum efficiency of recombination time limited devices is given by equation (2.58), but in this case d is the maximum distance the carriers travel at the saturation velocity in the recombination time.

References:

[1] H. Melchior, "Demodulation and photodetection techniques", in F. T. Arecchi and E. O. Schulz-Dubois, Eds., Laser Handbook, Vol. 1, North-Holland Amsterdam, 1972

[2] C. Jacoboni, C. Canali, G. Ottaviani, and A. A. Quaranta, "A review of some charge transport properties of Silicon", Solid-State Electron., 20, 77, (1977)

[3] J. G. Ruch and G.S.Kino, "Measurements of the velocity-field characteristics of GaAs", Appl. Phys. Lett., 10, 40 (1967)

[4] P. Smith, M. Inoue and J. Frey, "Electron velocity in Silicon and GaAs at very high electric fields", Appl. Phys. Lett., 37, 797 (1980)

[5] S. J. Bingham, B. Borger, D. Suter and A. J. Thomson, "The design and sensitivity of microwave frequency optical heterodyne receivers", Review of Scientific Instruments, 69 (9), pp: 3403-3409, 1998

[6] T. H. Wilmshurst, "Electron Spin resonance Spectrometers", ed. Adam Hilger, London, 1967

[7] C. P. Poole, "Electron Spin Resonance: A Comprehensive Treatise on Experimental Techniques", ed. Wiley, New York, 1983

[8] A. Abragam and B. Bleaney, "Electron Paramagnetic Resonance of Transition Metal Ions" (Dover, New York, 1970)

[9] R. E. Slusher, C. K. N. Patel and P.A. Fleury, Phys. Rev. Lett. 18,77 (1967)

[10] D.G.Thomas and J.J. Hopfield, Phys. Rev. 175, 1021 (1968)

[11] S. J. Bingham, J. J. Davies and D. Wolverson, "High-resolution optical detection of electron spin resonance in epitaxial semiconductor layers by coherent Raman spectroscopy", Physical Review B, vol. 65, 155301, Mar 2002

[12] J. J. Davies, G. N. Aliev, S. J. Bingham, D. Wolverson, S. Stepanov, B. Yavich and W. N. Wang "Optically detected magnetic resonance of paired defects in as-grown magnesium-doped GaN", Physical Review B, vol. 67, 035203, Jan 2002

[13] L. M. Roth, B. Lax and S. Zwerdling, Phys. Rev. 114, 90 (1959)

[14] S. J. Bingham, J. J. Davies and D. Wolverson, A. Waag, P. Prete, N. Lovergine, "Optical heterodyne detection of magnetic resonance in semiconductor structures", Proceedings of the 26th International Conference on the Physics of Semiconductors, Edinburgh 2002, Institute of Physics Conference Series 171, ed. A. R. Long and J.H. Davies, H1, 1-8, 2003

[15] L. C. Smith, S. J. Bingham, J. J. Davies and D. Wolverson, "Electron paramagnetic resonance of manganese ions in CdTe detected by coherent Raman spectroscopy", Applied Physics Letters, 87, 202101 (2005)

[16] L. C. Smith, S. J. Bingham, J. J. Davies and D. Wolverson, "Coherent Raman spectroscopy of Mn EPR in CdTe detected using a 33.7 GHz microwave source", April 2006, to be submitted to Applied Physics Letters.

[17] S. J. Bingham, J. Gutschank, B. Borger, D. Suter, A. J. Thomson, "Magnetic circular dichroism anisotropy from coherent Raman detected electron paramagnetic resonance spectroscopy: application to spin-1/2 transition metal ion in proteins", Journal of Chemical Physics, 113 (10): 4331-4338, 20

[18] D. M. Gvozdic, J. B. Radunovic, "Transit time of electrons and holes in micron and submicron MSM photodetectors", Semicond.Sci.Tech, vol 12, pp:589-594, 1997

[19] D. .M. Gvozdic, J. B. Radunovic, "Non-Stationary response of MSM photodetectors", IEEE Transactions on electron devices, 43(2): 370-372, 1996

[20] J. B. D. Soole and H. Schumacher, "InGaAs MSM photodetectors for long wavelengths optical communications", IEEE Journal of Quantum electronics, 27(3):737-750, 1991

[21] S. Averine, Y. C. Chan, Y. L. Lam ,"Geometry optimization of interdigitated Schottky-barrier MSM photodiode structures", Solid State Electronics, 45, pp: 441-446, 2001

[22] D. M. Gvozdic, J. B. Radunovic, "The influence of electron intervalley transfer on response width of the MSM photodetector" , International Journal of Infrared and millimeter waves, 17(6): 1001-1009, 1996

[23] S. Y. Chou and M. Y. Liu, "Nanoscale Tera-Hertz MSM photodetectors", Journal of quantum electronics 28 (10), pp 2358-2368, 1992

[24] Y. C. Lim and R. A. Moore, "Properties of alternatively charged coplanar parallel strips by conformal mappings", IEEE Transaction on electron devices, vol. ED-15, pp 173-180, 1968

[25] G. W. Farnell, I. A. Cermac, "Capacitance and field distributions for interdigital surface wave transducers", IEEE Transactions on Sonics and Ultrasonics, 17(3), 1970

[26] M. Zirngibl, M. Ilegems "High Speed photodetectors on InGaAs/GaAs-on-GaAs superlatices", J.Applied Phys., 69 (12), June 1991

Chapter 3

Literature Review

High-speed and high-efficiency photodetectors have been the subject of intense research over the past decades [1] [2], mainly for their applications in optical communication networks and generation of high frequency microwave/millimetre waves. In this section the development, optimisation and applications of Schottky contacted Metal-Semiconductor-Metal photodiodes are covered.

3.1 Early developments and applications

Metal-Semiconductor-Metal structures were first proposed and fabricated in their simplest form by Sze *et al.* [3] in the Bell Telephone Laboratories. The structure of the detector, as shown in Figure 3.1, consisted of a 12 μm thick n-type silicon wafer with platinum top and bottom contacts. In this paper the potential distribution in the semiconductor, carrier transport and current-voltage characteristics of a silicon detector were studied based on thermionic emission theory.

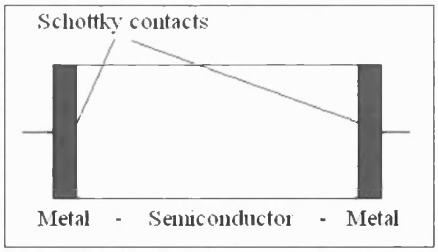

Figure 3.1 Schematic of MSM proposed by Sze, Coleman and Loya [3].

These kind of structure suffer from a slow response time due to the long distance travelled by the carriers, as well as being difficult to integrate with planar electronics. In order to overcome these problems Sugeta and Uritsu [4] [5] proposed a planar MSM detector with interdigitated contacts for application to high speed optoelectronics circuits. The fabrication of AND/OR and INHIBITOR/NOT gates using different combinations of MSMs with coplanar waveguides and strip lines on GaAs was realised, obtaining switching speeds as fast as 200 ps.

The monolithic integration of electronic and optoelectronic devices in optoelectronic integrated circuits (OEIC) is attractive for showing better noise and speed performance than circuits with individual connected elements. The integration of p-i-n detectors (vertical device) and field effect transistors or FET (planar device) presented major structural and fabrication incompatibilities [6] [7]. Therefore, the development of planar types of detector was of prime importance for simplifying the fabrication and optimising the performance of OEICs. The interdigitated MSMs, together with Mott barrier photodiodes [8] and interdigital surface photoconductors [9] were the most attractive alternatives.

In 1984 the Fujitsu research team, Ito *et al.* [10] [11], were the first to develop completely monolithically integrated photoreceivers consisting of MSMs and FETs using the receiver circuit shown in Figure 3.2 (a). The MSMs had an active area of 100μm x 100 μm with 16 fingers of width and spacing 3 μm fabricated by optical lithography. The study of the response time of the receiver when built using MSMs in comparison with the same circuit built using p-i-n diodes is especially relevant. Given the RC time limitation of the circuit, the lower value of the capacitance of the MSMs (see Figure 3.2 (b)) ensured a faster performance; a rise time of 300 ps, corresponding to a -3 dB frequency beyond 1 GHz was reported.

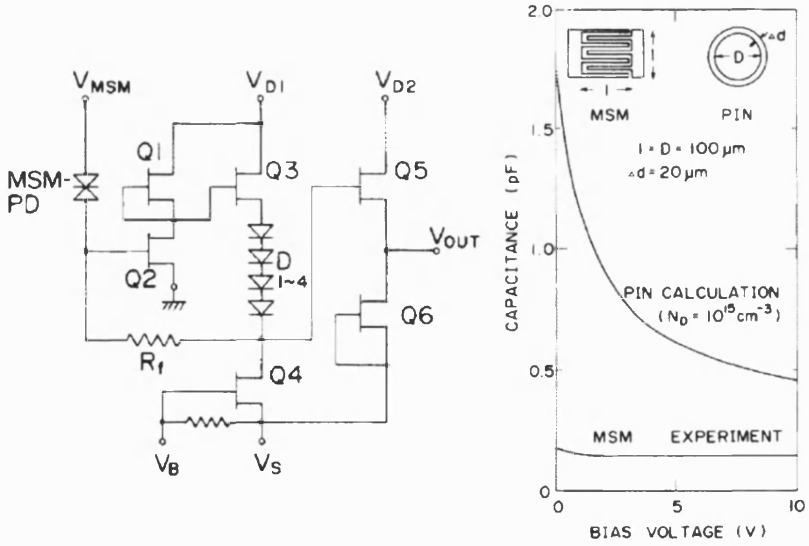

Figure 3.2 Circuit layout of the monolithically integrated MSM/transimpedance preamplifier (b) Capacitance comparison for p-i-n diode and MSM diode [11].

These advances culminated with the development of a monolithically integrated four-channel receiver using MSMs and FETs [12].

Another early application of MSM structures was their use in optoelectronic heterodyne detection schemes in two different configurations. The first one is referred to as an Optically Gated (OG) switch, and was demonstrated by Foyt and Leonberger [13] based on the previous work of Auston [14]. The second application proposed and fabricated by Lam and McDonald is the Electrically Gated (EG) switches [15]. The two mixer configurations are shown in the Figure 3.3:

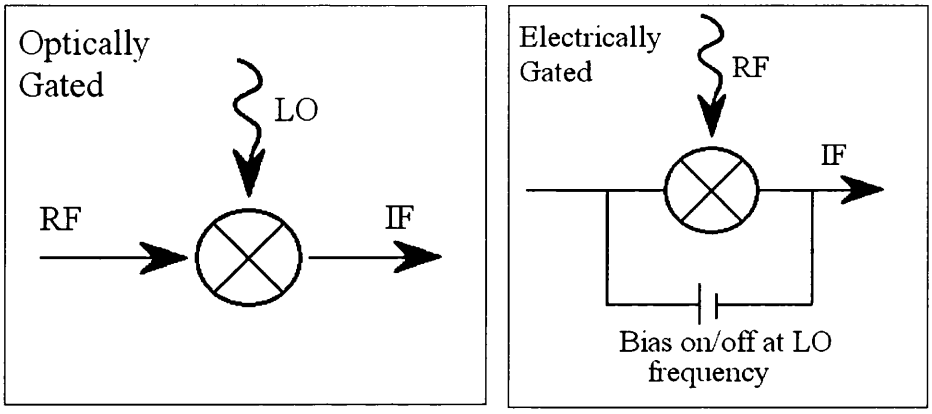

Figure 3.3 Schematic of optically and electrically gated mixer configurations.

In the OG configuration the optical signal is modulated at the switching frequency (local oscillator), and the signal to be gated is introduced electrically through one of the contacts of the MSM. The different mixing products, and in particular the intermediate frequency are transmitted electrically and filtered for connection to the spectrum analyzer. This configuration found application in high speed sampling and rapid switching of high voltages.

For the EG operation, the signal to be mixed is introduced optically and the switching frequency is introduced by changing the bias through the detector. When the bias voltage is under a certain threshold, the velocity of the optically generated carriers is reduced, making the transit time comparable to the recombination time. When this occurs the detected signal is reduced dramatically providing a switching detection function. Heterodyne detection using the EG configuration was applied to

switching matrixes for very broad signals. It is important to note that the application that this research project is concerned with is a third configuration where both the LO and the RF are introduced optically.

Once these applications for MSM structures were demonstrated, research concentrated on improving the minimum detectable signals and the frequency response of the MSM devices. Ito and Wada [16] reported the dependencies of the dark currents with different metals forming the Schottky contacts onto GaAs. The reported results are shown in Figure 3.4:

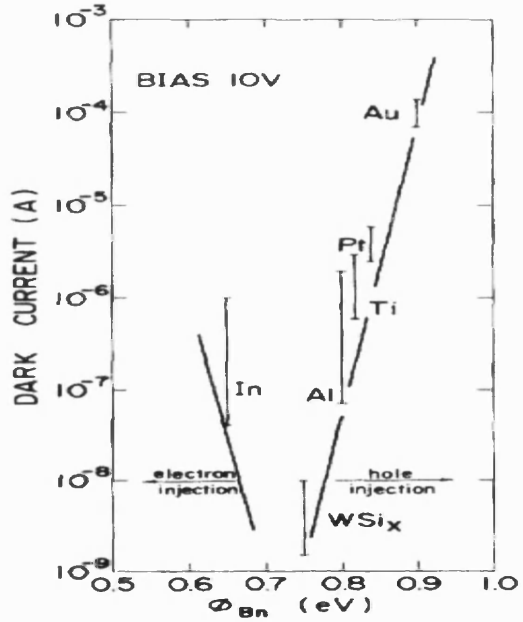

Figure 3.4 Dark current dependence on the barrier height reported by Ito and Wada [16].

Those results revealed the importance in the selection of material for the contacts, in order to achieve low values of the dark current, for reducing the minimum detectable signals for this type of detector. Consequently, a 140 fF MSM with WSi_x contacts and antireflection coating was fabricated and demonstrated to have a frequency response up to about 1.3 GHz. Discussions about how different models previously reported explain the gain mechanisms observed in experiments were included in the paper. Such models consider electron and hole tunnelling injection at cathode and

anode respectively due to accumulated carriers in the vicinity of the contacts and photo conducting gain due to long lifetime traps in the active layer or in the surface of the device.

These early years of research in MSMs culminated with the publication of the results obtained by Van Zeghbroeck *et al.* [17]. In this paper an MSM of active area 15 μm x 10 μm with aluminium fingers 0.75 μm wide and spaced 0.5 μm was fabricated by means of electron beam lithography on undoped GaAs. Under non illuminated conditions the device was found to have a dark current of 0.8 nA at 4 V bias voltage. The 4.8 ps FWHM electrical pulse reported was measured by the electro-optical sampling set up shown in Figure 3.5, the obtained response was deconvolved and Fourier transformed to give an instantaneous bandwidth of 105 GHz.

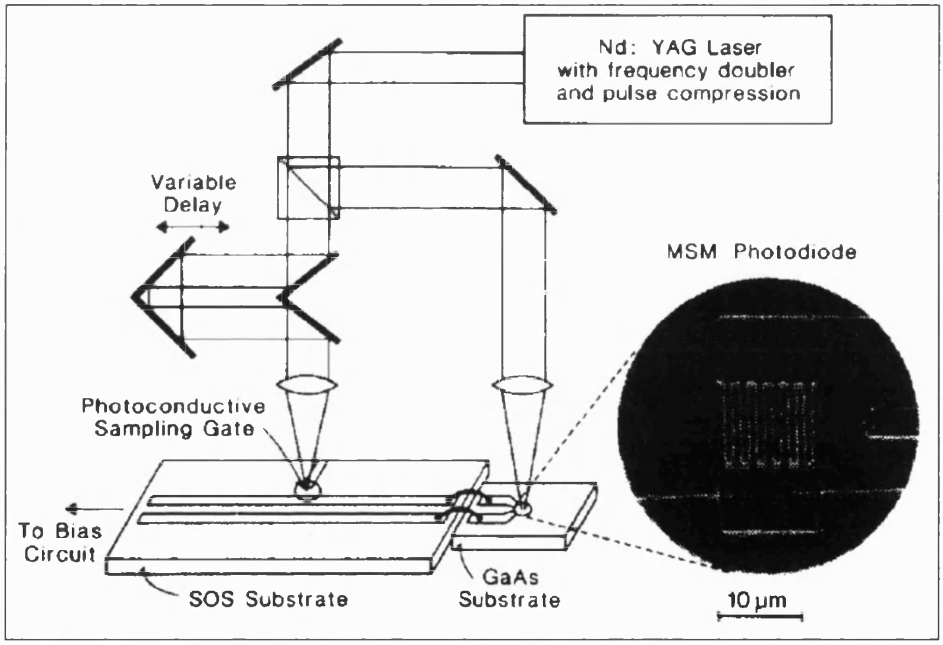

Figure 3.5 Electro-optical sampling setup used by Van Zeghbroeck *et al.* [17]

This paper reported the first experimental evidence that MSMs are able to operate at ultra-high frequencies with responsivity of 0.1 A/W. Such characteristics demonstrated their potential for implementation in different optoelectronic applications.

3.2 Materials

Different materials have been used in different applications depending mainly on the optical absorption characteristics, recombination times, carrier transport and barrier height of the semiconductor. This section compiles a review of selected papers that cover fabrication, testing and optimisation of MSMs in different materials.

Early research on metal-semiconductor-metal structures investigated the use of materials used widely in microelectronics, such as silicon, gallium arsenide and germanium. Most of these early devices were recombination time limited as small sizes were difficult to achieve with the existing fabrication techniques. Therefore achieving fast response times relied on fast carrier recombination. Two successful approaches for the limitation of the carrier average lifetime of in the semiconductor were doping of the material [18] and the damaging of the semiconductor with radiation [19].

In the late 80s and early 90s there was a conjunction of technological circumstances that made extensive research in MSMs possible. Improvements in semiconductor growth technology made available a wider range of high purity materials. Also the increased availability of electron beam lithography systems and femtosecond lasers allowed fabrication of smaller sizes and high-speed characterisation.

3.2.1 Silicon and GaAs

Chou and Liu [20] published in 1992 one of the most comprehensive reports of MSMs to date. This paper covers Monte Carlo simulations, fabrication and testing of devices built using GaAs, Low Temperature Grown GaAs (LTG GaAs) and Si. The main effort of this research consisted in the fabrication of devices with finger widths and spacings as small as 25 nm. The motivation for fabricating these devices on LTG GaAs is the improvement of the quantum efficiency by making the transit time of the devices an order of magnitude smaller than the recombination time. This approach results in a RC limitation in the frequency response as the fingers of submicron sizes are highly resistive, and the capacitance of the device is very high due to the proximity of the interdigitated contacts. For this reason the minimum feature size is

limited to 100 nm. The experimental results of the responses obtained via EO sampling for wavelength 620 nm are shown in the Figure 3.6:

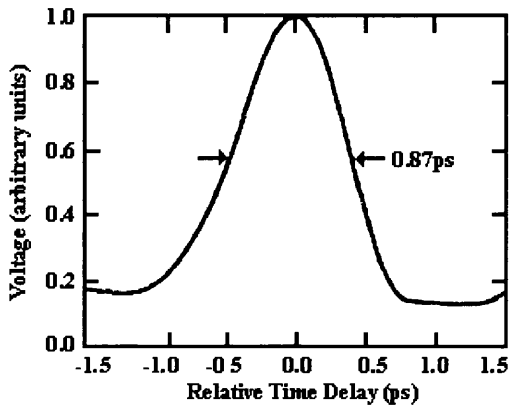

Semiconductor	LT-GaAs			Bulk GaAs	Bulk Si	
Finger spacing / width (nm)	100 / 100	200 / 200	300 / 300	100 / 100	100 / 100	1200 / 800
Intrinsic transit time (ps)	0.4	0.8	1.1	0.4	2.7	12.5
(In) RC time constant (ps)	1.56	1.04	0.52	1.56	1.56	1.39
Measured Response (ps)	1.6	1.0	0.87	1.5	10.7	14.3
Measured Bacndwidth (GHz)	280	440	510	300	41	32

Figure 3.6 Results reported by Chou and Liu [20]

a)Response of LTG-GaAs MSM PD with 300nm spacing and width at 1.5 V bias

b)Table of measured data for different material and dimensions.

The MSM devices reported in this study have active areas of 10 μm x 10 μm for GaAs and LTG GaAs, and 20 μm x 20 μm for silicon devices. As it can be observed in Figure 3.6, the measured bandwidth for LTG GaAs devices is higher for larger spacing, confirming that they are RC time constant limited devices. These were the fastest photodetectors on LTG GaAs reported to date.

The lower bandwidth of devices on crystalline silicon was attributed to the weaker optical absorption and longer recombination time [21], making possible the collection of carriers generated deep in the material. This poses a further problem as the bandwidth is dependent on the wavelength of the incident light. To overcome this fact, Liu *et al.* [22] fabricated MSMs on silicon-on-insulator, reporting a record bandwidth of 140 GHz. In this configuration, a thin layer (100 nm) of silicon is separated from the bulk silicon with a layer of oxide, preventing deeply generated carriers from being collected and providing a bandwidth independent of the incident

light wavelength. An additional advantage claimed by the workers for such devices is the lower capacitance of the detectors due to the lower dielectric constant of the oxide, reducing the RC constant, therefore allowing the possibility of a faster response. This faster response was counterbalanced by a decrease in quantum efficiency due to reduced absorption in the thin layer of material. For minimising this reduction in responsivity the researchers proposed a quarter-wave stack of reflectors (Si/SiGe) underneath the active layer.

Due to the short carrier recombination time in LTG GaAs, many workers have reported ultra high frequency response of MSMs in such material, at the cost of low quantum efficiency. The study of the carrier lifetime in GaAs as a function of the growth temperature and post growth annealing was done by Melloch *et al.* [23]. Making use of the results in this study, Krishnamurthy *et al.* [24] reported MSMs on intermediate temperature grown (ITG) GaAs where the carrier lifetime was tailored to be of the order of magnitude of the average transit time. In this paper a large area detector (400 μm x 400 μm) was reported to have an instantaneous bandwidth of 4 GHz with dark currents of the order of nano amperes. A comparison of the same device built on ITG (Intermediate Temperature Grown) and HTG (High Temperature Grown, as normally grown) GaAs was presented for demonstrating an improvement in frequency response without dramatically affecting the efficiency. The results are illustrated in Figure 3.7:

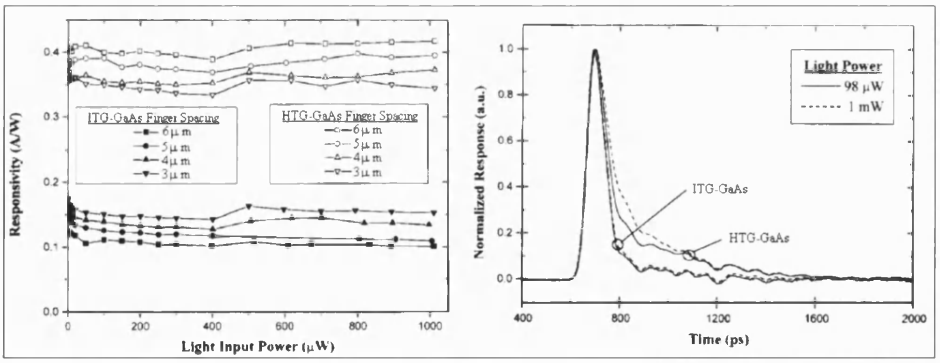

Figure 3.7 Performance comparison of 400 μm x 400 μm MSMs built on ITG and HTG GaAs [24].

3.2.2 Materials for telecommunications wavelengths -InGaAs and Germanium

Devices built on GaAs and Si are suitable for the short-wavelength part of the spectrum, but the absorption of light in these materials at telecommunication wavelengths (1.3 μm and 1.55 μm) is very weak. The material that is generally used for such wavelengths is InGaAs, but its use for MSMs is problematic since the barrier heights of this material are very low [25]. This low barrier means that detectors evaporated directly onto InGaAs suffer from unacceptably high values of the dark current. To circumvent this problem barrier enhancement techniques consisting of the addition of a top thin strained layer of GaAs [26] [27] and AlGaAs [28] [29] were proposed. Moderate reduction of the dark current was achieved, but at the expense of long tail responses due to the trapping and re-emission of carriers in the strained interface between the active layer and the cap layer. Soole and Schumacher [30] proposed the use of a lattice matched InAlAs layer on top of the InGaAs layer. The barrier enhancement layer modified the band diagram as shown in Figure 3.8, and was successfully proved to reduce the dark current of the devices [31].

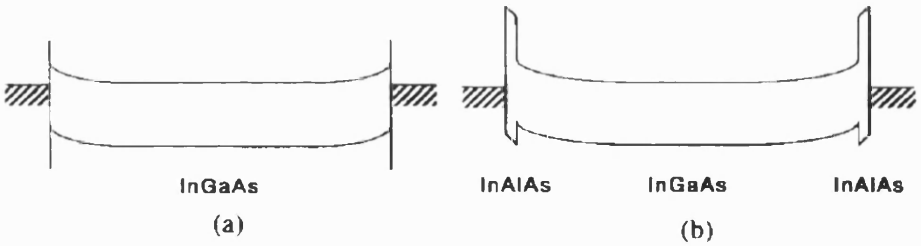

Figure 3.8 InAlAs Schottky barrier enhancement layer proposed by Soole and Schumacher [30].

Another approach for barrier enhancement is the use of an InP:Fe cap layer [32]. Kuhl *et al.* [33] reported the fabrication and testing of transit time limited devices with such epilayered structures, achieving moderate dark current (300 nA) and transient responses of the order of tens of picoseconds. The -3 dB bandwidth of devices with 1.5 μm spacing at 0.84 μm was estimated to be 75 GHz with an internal quantum efficiency of 100%. In Figure 3.9 the response of a 2 μm spacing MSM as a function of bias is shown, the inset figure confirms that the devices are transit time limited:

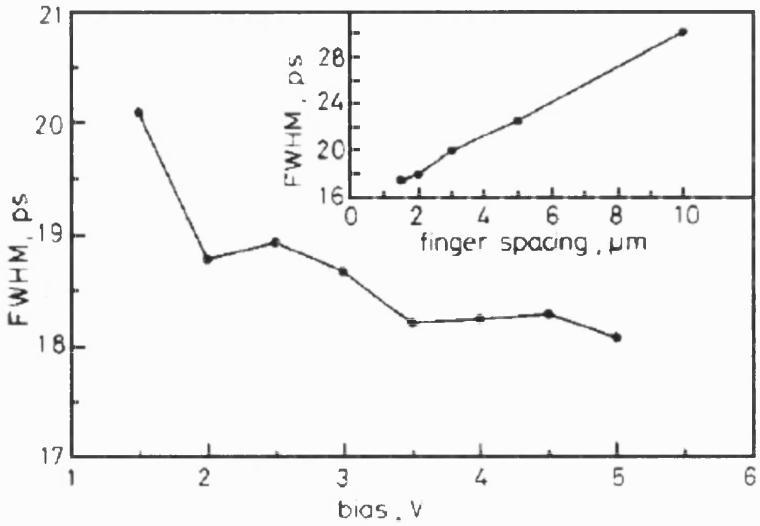

Figure 3.9 Results of FWHM for 0.84 μm obtained by Kuhl, Hieronymi *et al.* [33]

The epilayered structure was fabricated using MOCVD, and consisted of a 300nm buffer layer of InP:Fe, followed by a 2 μm thick active layer of InGaAs capped with a 20 nm barrier enhancement layer of InP:Fe.

Soole and Schumacher [34] discussed the different gain mechanisms previously reported in InGaAs barrier enhanced MSM devices. Those gain mechanisms, as well as long tail responses, were attributed to traps due to lattice mismatches in the interfaces between the substrate and the active layer, and between the active layer and the barrier enhancement layer. They proposed high speed, low dark current and highly efficient devices based on a lattice-matched epilayered structure consisting of a InP substrate, followed by an InGaAs active layer capped with a InAlAs barrier enhancement layer.

In this paper, the reported values of dark current for barrier enhanced InGaAs MSM photodetectors were the lowest to date. Due to the resultant energy band of the epilayered structure (see Figure 3.8), at high bias voltages the dark current rose due to tunnelling through the enhancement layer, as seen in Figure 3.10

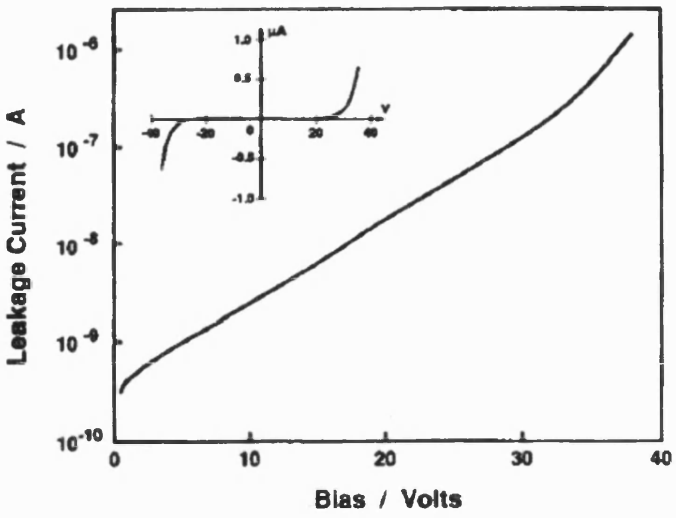

Figure 3.10 Dark current vs. bias for InGaAs/InP lattice matched MSM with an active area 18 μm x 18 μm and 0.5 width/spacing ratio [34].

Photodetectors with 0.5 μm and 1 μm finger widths and spacing ranging 1-3 μm were estimated to be transit time limited. Two dimensional Monte Carlo simulation, neglecting diffusion, recombination, trapping, ballistic effects and velocity overshoot of the carriers, is used to model MSMs of the mentioned dimensions. With such a model, trade-offs between bandwidth and efficiency for devices of different active layer thicknesses are presented with similar results for 1.3 μm and 1.55 μm. Those results are shown in Figure 3.11:

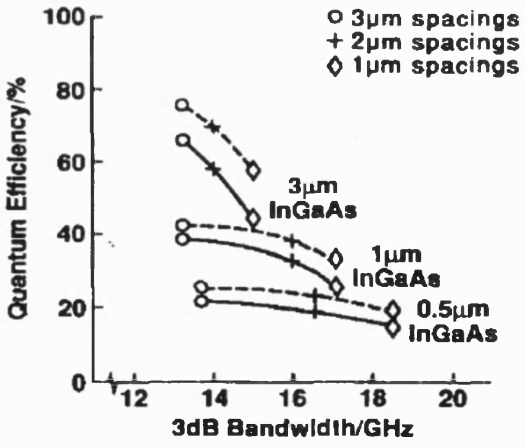

Figure 3.11 Bandwidth/efficiency trade off reported by Soole and Schumacher [34].

In Figure 3.11, the lines join devices with the same active layer thickness, the solid lines corresponding to finger width 1 μm and the dotted lines corresponding to finger width 0.5 μm. These results showed the potential of MSMs built onto InGaAs for their use in high speed optoelectronic receivers at telecommunication wavelengths.

The other material that is suitable for near infrared telecommunication wavelengths is Ge due to the direct narrow bandgap (0.8 eV) and strong optical absorption. The use of germanium was prominent in semiconductor research in the USSR from the 70s, and MSM structures such as the one proposed by Sze *et al.* were demonstrated [35]. More recently, planar MSM structures onto germanium over silicon have been demonstrated. Using silicon as a carrier has the advantage of making these devices fully compatible with other silicon technology. The main problem with this approach was the lattice mismatch between the materials, provoking stress and defects in the active epilayer. Colace *et al.* [36] demonstrated a simple approach for overcoming this problem. They used CVD for fabricating wafers with a buffer layer of low temperature grown Ge between the carrier and the active layer, therefore relaxing the strain. This technique makes possible the fabrication of much thicker flat films of germanium with fewer defects. They fabricated photodetectors onto 500 nm thick Ge active films with silver contacts. The results obtained for the photocurrent dependency on wavelength are shown in Figure 3.12:

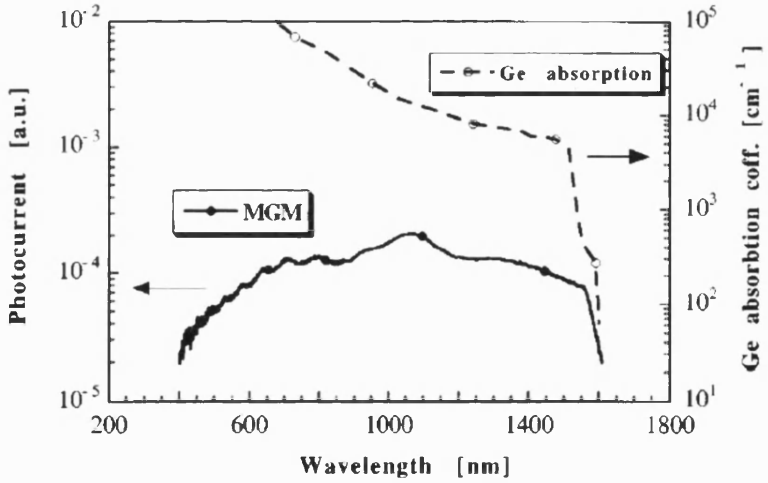

Figure 3.12 Photocurrent of MSM and optical absorption of crystalline Ge reported in by Colace *et al.* [36]

DC tests yielded a responsivity as high as 0.24 A/W corresponding to a wavelength of 1.3 μm. The time response of this device was experimentally demonstrated by illuminating the device with a Nd:YAG laser with pulses of 100 ps at 1.3 μm and the output signal was monitored with a 1 GHz oscilloscope. Using this setup, devices with 10 μm spacing showed a response time of 2 ns. This paper does not explore whether the origin of such a slow response is the result of the size of the device (finger sizes are not reported) or because the limitation imposed by the measuring equipment.

Buca *et al.* [37] demonstrated the high speed operation of an MSM using a similar epilayer structure to Colace *et al.* In this study Cr contact MSMs with active areas ranging 10 μm x 10 μm – 100 μm x 100 μm and finger widths and spacings between 1.5 μm and 5 μm were fabricated. The smaller of these devices were characterized in an electroptical sampling system at wavelengths of 1.3 μm and 1.55 μm. This experiment yielded response time as short as 12.5 ps corresponding to a 3 dB bandwidth of 13 GHz. Another relevant investigation included in this paper is the decrease of the dark current of the devices with SiO_2 passivation, the results are shown in Figure 3.13:

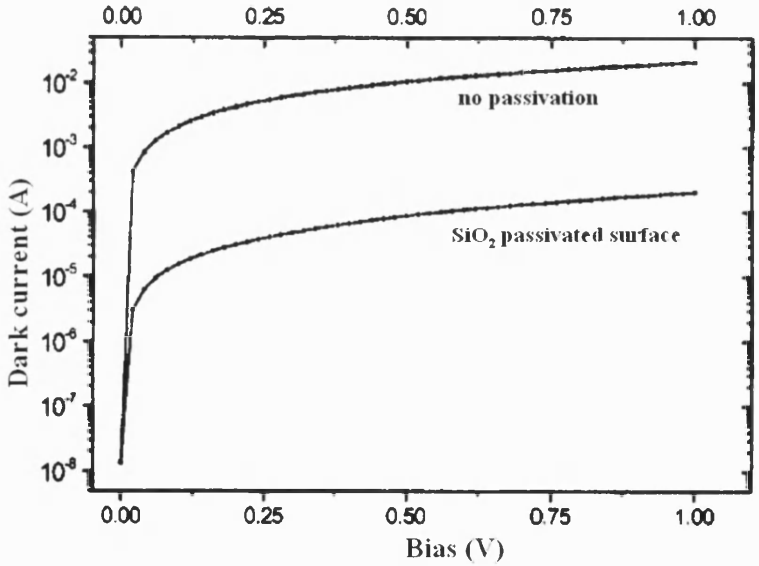

Figure 3.13 Reduction of the dark current due to passivation reported by Buca *et al.* [37]

The passivation of the devices consisted of the addition of a SiO_2 layer onto the wafer, and the etching of such oxide prior to chromium evaporation of interdigitated structures and contacting pads. The reduction of the dark current is attributed to the reduction of the Ge surface current.

The most complete results for ultrahigh-speed MSM Ge-on-insulator photomixers were reported by Rouviere *et al.* [38]. In this paper bandwidths of 10 GHz, 18 GHz, 20 GHz and 35 GHz were measured for devices with spacings of 2 μm, 1 μm, 0.7 μm and 0.5 μm respectively.

3.2.3 UV Photodetectors – GaN, ZnO, ZnSe and DLC

The interest in the use of GaN and its alloys grew through its use as a material for the production of blue lasers and LEDs [39]. Following studies for fabrication of high quality contacts on GaN [40], the interest extended to the study of GaN on sapphire for visible-blind photodetectors [41]. The potential applications for this type of detector are very broad, thanks to the good performance of III-V nitrides at high temperatures and in caustic environments [42]:

- Military and space communications applications
- Engineering monitoring – ex. aircraft control systems and flame detection
- UV astronomy

To the best of this author's knowledge, Walker *et al.* were the first to have reported a comprehensive study of the high speed potential of GaN [43]. In this paper they built devices on unintentionally doped GaN and Mg doped GaN using Pt/Au for the metallisations. Experiments on spectral optical absorption and responsivity dependence on optical power were reported. The frequency response was investigated by illumination with a pulsed nitrogen laser (337 nm) yielding pulse widths of <10 ns (limited by the measurement equipment) and 200 ns for GaN and Mg:GaN respectively.

More recently Li *et al.* have reported temporal characterisation of ultra high speed MSMs on GaN [44]. Detectors of active area 25 μm x 25 μm and finger widths and

spacings ranging from 0.3 μm to 5 μm were fabricated onto a 2 μm GaN wafer grown on sapphire. The impulse response of the devices at 270 nm wavelength for different incident powers was studied. The longer response found for higher levels of illumination was attributed to space-charge screening effect. The results obtained for devices with finger width and spacing 0.3 μm are shown in the Figure 3.14:.

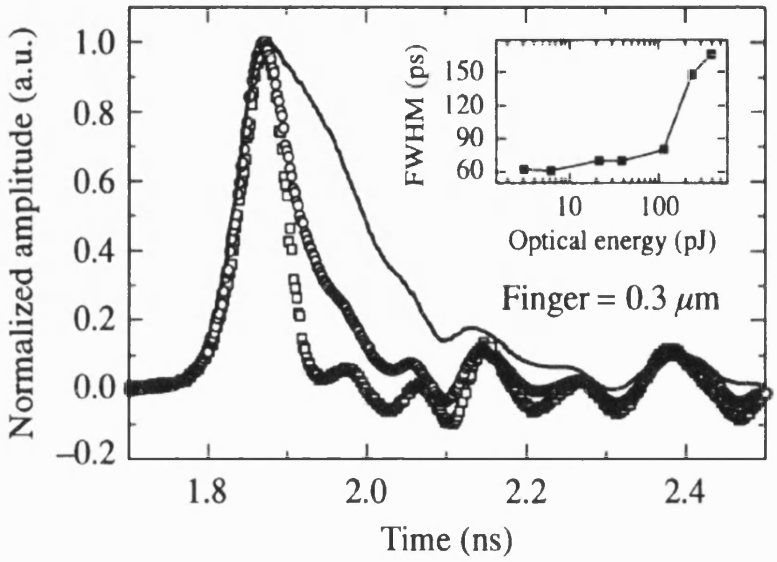

Figure 3.14 Impulse response for illumination energies of 3 pJ (squares) , 116 pJ (circles) and 391 pJ (solid line) reported by Li *et al.* [44]

In a later work [45] they demonstrated a record FWHM on GaN of 3.5 ps for low illumination levels using and EO sampling system. This is the fastest response reported to date for conventionally grown GaN. The data obtained was used for the estimation of the electron velocity in GaN for different field strengths. The obtained results are shown in Figure 3.15:

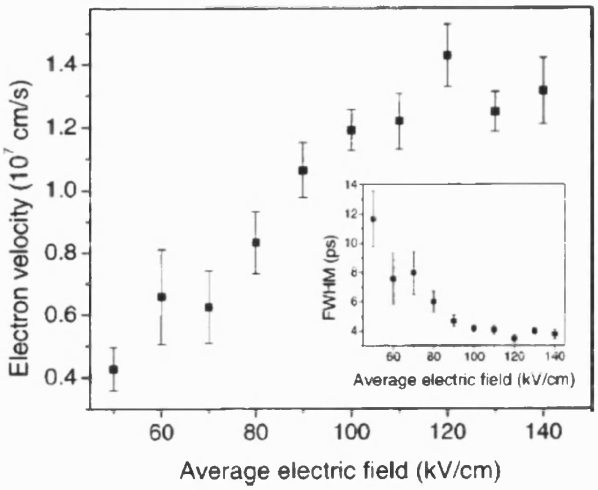

Figure 3.15 Electron velocity and FWHM dependence on electric field [45].

The latest improvement in frequency response for photodetectors in GaN was reported by Mikulics *et al.* [46]. This material, when grown at low temperatures (650°C), instead of conventional growth at high temperatures (750°C - 900°C), has a dislocation density fifty times higher, and it has a lower electron mobility. These two circumstances reduce the carrier lifetime to the sub-picosecond range (760 fs was reported). A device of active area 20 μm x 20 μm and finger width and spacing of 1 μm and 1.5 μm respectively was illuminated with 100 fs pulses, giving an output signal of a record 1.9 ps FWHM.

AlGaN has similar advantages to GaN with the addition that the cut-off wavelength can be altered by varying the concentration of Al [47]. In this paper Butun *et al.* tailor the Al concentration for maximising the performance in deep ultra violet frequencies. They obtained a responsivity of 0.53 A/W with an ultraviolet- visible rejection of 7 orders of magnitude.

Chang *et al.* studied the performance of ZnSe MSM devices with the active layers grown over GaAs and ZnSe. [48]. The use of ZnSe as a carrier yielded better performance of quantum efficiency and dark current than when using GaAs. In later research [49] they investigated the characteristics of contacts when using different materials. Calculations of barrier heights for ITO (indium tin oxide), TiW and Ni/Au,

together with the simulated response using thermionic emission modelling was reported, yielding the results shown in Figure 3.16:

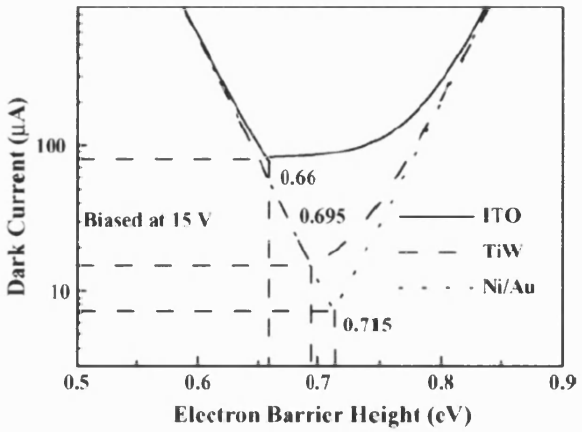

Figure 3.16 Theoretical barrier heights and dark currents for MSMs on ZnSe reported by Chang *et al.* [49]

The dark current values obtained experimentally were found to be higher than that predicted theoretically for devices of finger width and spacing 10 μm. Low frequency measurements were performed, confirming the 1/f noise component.

The same group reported detectors on MBE grown ZnO over sapphire for UV operation [50]. They investigated the use of Ru, as in previous research Au and Ag contacts proved problematic over this material. Dark currents three orders of magnitude smaller than the photocurrent were measured, and discrete response times were obtained (850 ms) due to the large size of the devices (10 μm finger width and spacing) and the experimental technique employed.

A relatively novel material that has been the subject of intensive research in the last decade for its application in electronics is diamond-like carbon (DLC) structures [51]. A multitude of applications have been proposed and demonstrated for this material, among them, its use for UV detection using metal-DLC-metal [52].

3.3 Optimizations- Improving the frequency response and quantum efficiency

Apart from the different trade-offs described in the previous sections, there are a variety of approaches that have been employed for optimizing the performance of MSMs. The simplest of these approaches, as has been already described, is the use of a buried layer under the active layer for avoiding the collection of deeply generated carriers. In this section the most prominent examples encountered during our research are presented.

Burm *et al.* [53] studied the maximum quantum efficiency that GaAs MSMs can achieve depending on their dimensions and wavelength of incident light. They estimated that the loss of light in the interface between air and the semiconductor was around 30%. This value together with the shadowing effects and the light absorbed too deeply limits greatly the performance of these devices. As with many other applications in optoelectronics the use of an antireflection (AR) coating was found desirable for minimising the reflections at the interface. Carrano *et al.* [41] reported the use of an AR coating for GaN MSMs calculating the optimum thickness of the layer as:

$$\text{AR coating thickness} = (\lambda_0 / 4n(\lambda))^{*}m \qquad (3.1)$$

where λ_0 is the wavelength in free space, $n(\lambda)$ the refractive index of the material at the operating wavelength and m an odd integer. The antireflection coating not only improves the external quantum efficiency, but the internal quantum efficiency too, as it reduces the recombination close to the surface. In addition it reduces the dark current of the devices, as shown in Figure 3.13.

Another technique for enhancing the quantum efficiency of these devices is the use of transparent and semitransparent contacts for minimizing the shadowing effects. Examples of this type of material are TiN, ITO, TiW and W. The use of such materials requires an adequate barrier height when brought in contact with the semiconductor, as well as having low value of resistance. This enhancement of the

quantum efficiency is achieved at the cost of reduction in frequency response in transit time limited devices [54]. This is due to the fact that light collected directly under the contacts generates electron-hole pairs in a region where the electric field is weak, therefore introducing a tail in the response.

Texturing of semiconductor for increasing the optical absorption is an approach that has been investigated for the improvement of the efficiency of solar cells [55]. The same principle has been successfully applied to MSMs [56]. In this paper triangular and rectangular sub-wavelength texturing (width ranging 50 - 250 nm, depth 1000 μm) of the active area was demonstrated to reduce the reflectivity and to enhance the internal quantum efficiency. As can be seen in Figure 3.17, the higher orders of transmitted waves for textured devices travel in non-perpendicular angles to the air-semiconductor interface. This fact leads to the reduction of the transit time of the carriers (as they are closer to the contacts) improving the internal quantum efficiency (as less carriers recombine before collection). The compared performance of conventional and textured MSM devices is shown in Figure 3.17.

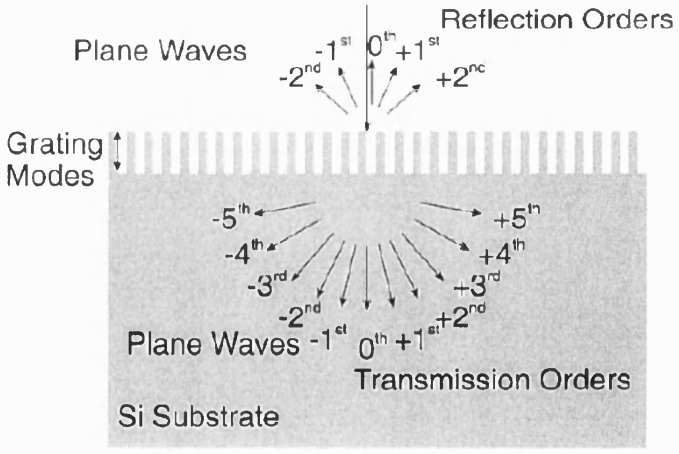

Device	Surface Reflection	Responsivity (A/W)	External Q.E.	Internal Q.E.
Planar	~33%	~0.23	~44%	~66%
Structured	~3%	~0.43	~81%	~84%

Figure 3.17 a) Diagram of transmission orders for textured devices and b) Experimental results of surface reflectance, responsivity, external and internal quantum efficiency for planar and nanostructured devices at 700nm wavelength[56].

Using nano-structured photodetectors brings the added advantage of improving the frequency response of transit time limited devices. The devices described in this paper are limited by the drift time of the carriers, the obtained time responses reported correspond to 1700 ps for planar and 600 ps for the equivalent nano-structured detector.

The use of buried and semi-buried contacts has been investigated for MSM due to their potential in improving the efficiency of the devices. Sharma *et al.* [57] studied and characterised devices using semi-buried contacts in the three possible configurations shown in Figure 3.18.

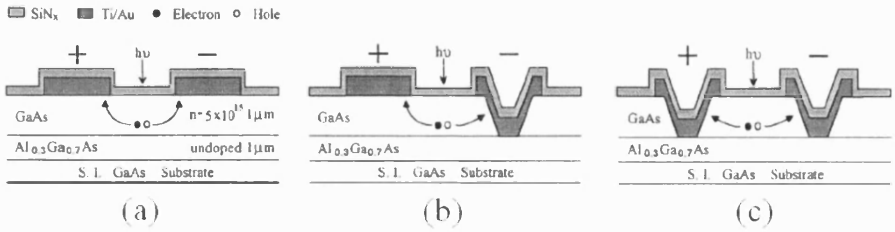

Figure 3.18 Different configurations reported in [57] a) Without recessed electrode b) Recessed cathode c) recessed cathode and anode.

The most important feature of this type of detector is the improvement of the quantum efficiency by reducing the transit time of the carriers, as well as slightly improving the frequency response due to the more homogeneous electric field between contacts. Furthermore, that was achieved without a degradation of the dark current or the capacitance of the device.

Burm *et al.* [58] proposed a circular shaped device, and this concept was extended to other shapes [59]. The advantages of circular and elliptical active area is the reduction of the capacitance without a great reduction in the efficiency, as its shape accommodates the Gaussian shape of the laser beam. This provide a potential improvement of the frequency response for RC limited devices.

As it has been previously discussed, the quantum efficiency of the devices is greatly limited by the portion of light that is absorbed within the active region. Furthermore,

it is not desirable to collect deeply generated carriers as, due to the long transit times, they would introduce a tail in the time response. Placing the active region within a Fabry-Perot resonant microcavity provides the mechanism for the light to make multiple passes through the semiconductor. The family of optoelectronic devices using such a mechanism are referred to as Resonant-Cavity Enhanced (RCE) photonic devices [60], and it comprises photodetectors, phototransistors, modulators and LEDs. The main feature of this mechanism is the possibility of selecting the resonant wavelength by tuning the thicknesses of the different layers of the Bragg reflector.

Li *et al.* were the first to propose an RCE MSM [61]. In this paper a GaAs MSM with an antireflection coating on top of the device and a buried Bragg reflector under the active area consisting of alternative epilayers of GaAs/AlGaAs was theoretically analysed. The result of the study was the potential of this type of device for achieving nearly 100% internal quantum efficiency. Different workers have followed this research and demonstrated experimentally this type of device for GaAs and InGaAs [62] [63] [64]. Kishino *et al.* [65] fabricated and characterised a GaN RCE MSM including a top reflector for maximising the absorption. The epilayered structure used and the results of the improved performance with the top reflector are shown in Figure 3.19:

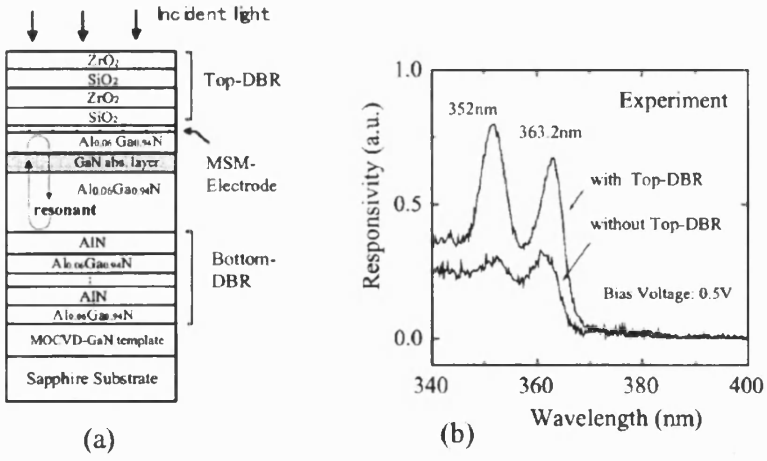

Figure 3.19 a) Schematic of the cross-section of RCE-MSM and
b) UV responsivity spectra of RCE-MSM reported by Kishino *et al* [65].

3.4 Advanced Applications

This type of high speed photodetectors has found applications in optoelectronic generation of high power microwaves/mm-waves by heterodyne conversion and for optical signal linking [66].

The research carried out in this project is concerned with the first of such applications. Verghese *et al.* [67] demonstrated the ability of metal-semiconductor-metal photodetectors to generate coherent signals at the difference frequency between two co-propagating beams incident on the device (photomixer operation). These workers verified the operation of this type of detector on LTG-GaAs for generating signals at frequencies up to 2.5 THz and an output power of 0.2 μW [68]. Thanks to these advances, MSMs were successfully demonstrated for their application as local oscillators for superconducting bolometric mixers.

The use of a single MSM for high-power high-frequency signal generation has an inherent limitation in the trade off between the high-speed requirement (reduced active area) and the output level (increase of detection area). Different approaches have been proposed for overcoming such limitation, the most prominent one is called velocity matched photodetector [69]. In this arrangement the individual outputs of every detector in an array interfere constructively to form a high power signal. Of this family of detectors probably the most interesting are the velocity matched waveguide photodetectors (VM-WGPD).

MSM Waveguide photodetectors were proposed by Soole *et al.* in the two different configurations shown in Figure 3.20.

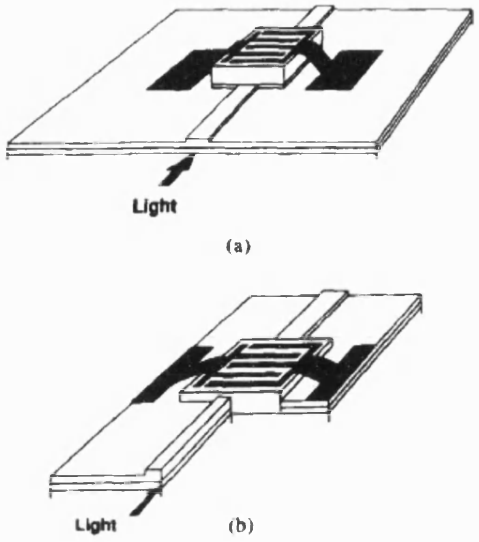

Figure 3.20 Two configurations proposed by Soole *et al.* (a) vertical coupling geometry [70] and (b) butt coupled waveguide photodetector [71].

In the vertical coupled geometry detector, light couples up into the active area of the detector from the waveguide passing beneath it. As a small fraction of light is absorbed in this configuration, the applications for this type of integrated detector are monitoring the power of passing signals and for signal recognition. If this detector is to be used as a terminating photodetector, the length of the device must be of hundreds of microns to ensure the coupling of the most of the power into the diode. In the butt-coupled geometry the power is coupled into the side of the structure, the light being absorbed in a few microns. This configuration was reported as suitable in cases when the structure is incompatible with vertically coupled detection.

Velocity matched WGPD were successfully applied for the heterodyne generation of high-power high-frequency signals for use as Local Oscillator [72].

References:

[1] K.Kato, "Ultrawide bandwidth/High frequency photodetectors", IEEE Transactions Microwave Theory Tech, vol 47, pp 1265-1281, 1999

[2] M. Razeghi, "Short wavelength solar blind detectors- status prospects and markets", Proceedings of the IEEE, 90 (6), pp 1006-1014, 2002

[3] S. M. Sze, D. J. Coleman, A. Loya, "A current transport in Metal-Semiconductor-Metal (MSM) structures", Solid State Electronics, 14(12): 1209-&, 1971

[4] T. Sugeta, T. Uritsu T, "High-Gain Metal-Semiconductor-Metal Photodetectors for high-speed optoelectronic circuits", IEEE Transactions on electron devices, 26(11):1855-1856, 1979

[5] T. Sugeta, T. Uritsu, S. Sakata and Y. Mizushima, "Metal-Semiconductor-Metal Photodetectors for high-speed optoelectronic circuits", Japanese Journal of applied physics, 19:459-464 Suppl. 1, 1980

[6] R. F. Leheny, R. E. Nahory, M. A. Pollack, A. A: Ballman, E. D. Beebe, J. C. Dewinter and R. J. Martin, "Integrated InGaAs p-i-n/FET photoreceiver", Electron. Letters, vol 16 (10), pp 353-355, May 1980

[7] S. Miura, O. Wada, H. Hamaguchi, M. Ito, M. Makiuchi, K. Nakai and T. Sakurai,"A monolithically integrated AlGaAs/GaAs p-i-n/FET photoreceiver by MOCVD", IEEE Electron device letters, EDL-4 , 375-376, 1983

[8] C. J. Wei, H. J. Klein, H. Beneking, "Symmetrical mott barrier as a fast photodetector", Electron letters (17), pp 688-690, 1981

[9] C. W. Slayman and L. Figueroa, "Frequency and pulse response of a novel interdigital surface photoconductor", IEEE electron device letters (2), pp 112-114, 1981

[10] M. Ito, O. Wada, K. Nakai and T. Sakurai, "Monolithic integration of a MSM photodiode and a GaAs preamplifier", IEEE electron device letters, (EDL-5):12, 531-532, 1984

[11] M. Ito, O. Wada, K. Nakai, T. Sakurai, T. Kumai, H. Hamaguchi, M. Makiuchi, "High speed monolithically integrated GaAs photoreceiver using a MSM photodiode", Applied Physics letters, 47 (11), 1129-1131, 1985

[12] M. Ito, O. Wada, T. Sakurai, H. Hamaguchi, M. Makiuch, T. Kumai, "A Monolithic four-channel photoreceiver integrated on a GaAs substrate using MSM photodiodes and FET's", IEEE electron device letters, (6)12, pp 634-635, 1985

[13] A. G. Foyt, F. J. Leonberger and R. C. Williamson, "InP photoelectronic mixers", SPIE, vol 269, pp. 109-114, 1981

[14] D. H. Auston, "Picosecond optoelectronic switching and gating in silicon", Applied physics letters, vol.26, pp. 101-103, 1975

[15 D. K. W. Lam and R. I. McDonald, "GaAs optoelectronic mixing operation at 4.5 GHz", IEEE transactions on electron devices, vol. 31(12), 1984

[16] M. Ito and O. Wada, "Low dark current GaAs MSM photodiodes using WSix contacts", IEEE Journal of quantum electronics, 22(7), pp 1073-1077, 1986

[17] B. J. Van Zeghbroeck, W. Patrick, J. M. Halbout and P. Vettinger, "105-GHz MSM photodiode", IEEE Electron device letters, 9(10), pp 527-529, 1988

[18] R. A. Lawton and A. Scavannec, "Photoconductive detector of fast transition optical waveforms", Electronics Letters, 11(4):74-75, 1975

[19] P. R. Smith, D.H. Auston, A. M. Johnson and W. M. Augustyniak , "Picosecond photoconductivity in Radiation Damaged Silicon on Sapphire films", Applied Physics Letters, 38(1):47-50, 1981

[20] S. Y. Chou and M. Y. Liu, "Nanoscale Tera-Hertz MSM photodetectors", Journal of quantum electronics 28 (10), pp 2358-2368, 1992

[21] M. Y. Liu, S. Y. Chou, S. Alexandrou, C. C. Wang and T. Y. Hsiang, "A 75 GHz silicon MSM Schottky photodiode", Applied Physics letters 62 (20): 2507-2509, May 1993

[22] M. Y. Liu, E. Chen and S. Y. Chou, "140 GHz MSM photodetectors on silicon-on-insulator with scaled active layer", Applied physics letters, 65 (7): 887-888, 1994

[23] "Molecular beam epitaxy of non stoichiometric semiconductor and multi phase material system" Critical reviews in solid state and material science vol 21, pp 189-263, 1996.

[24] V. Krishnamuthy, M. C. Hargis and M. R. Melloch, "A 4-GHz large area (160 000 um^2) MSM-PD on ITG-GaAs", IEEE Photonics technology letters, 12(1):71-73, 2000

[25] K. Kajiyama, Y. Mizushima and S. Sakata, " Schottky barrier height of n-InGaAs diodes", Applied physics letters, 23:458-460, 1973

[26] H. Schumacher, H. P. Leblanc, J.B.D. Soole and R. Bhat, "An investigation of the optoelectronic response of GaAs/InGaAs MSM photodetectors", IEEE electron device letters, 9: 607-609,1988

[27] J. Hugi, Y. Haddab, R. Sachot and M. Ilegems, "Carrier trapping in ultrafast MSM photodetectors on InGaAs/GaAs-on GaAs superlattices", Journal of applied physics, 77 (4): 1785-1794, 1995

[28] T. Kikuchi, H. Ohno and H. Hasegawa, "$In_{0.53}Ga_{0.47}As$ MSM photodiodes using a lattice mismatched AlGaAs Schottky assist layer", Electron letters, 24: 1208-1210, 1988

[29] W. P. Hong, C. K. Chang and R. Bhat, "High performance $Al_{0.15}Ga_{0.85}As/In_{0.53}Ga_{0.47}As$ MSM photodetectors grown by OMCVD", IEEE Transaction on electron devices (36):659, 1989

[30] H. Schumacher, J. B. D. Soole, H. P. Leblanc, R. Bhat and M. A. Koza, "High speed response of InAlAs/InGaAs MSM photodetectors at 13 μm and 1.55 μm wavelengths- experiment and theory", IEEE Transaction on electron devices, 36(11):2624-2625, part 1, 1989

[31] H. Schumacher, J. B. D. Soole, H. P. Leblanc, R. Bhat and M. A. Koza, "Noise behaviour of InAlAs/GaInAs Photodetectors", Electronics letters, 26 (9): 612-614, 1990

[32] L. Yang, A. S. Sudbo, R. A. Logan, T. Tanbunek and W. T. Tsang, "High performance of Fe:InP/InGaAs MSM photodetectors grown by metalorganic vapor phase epitaxy", IEEE Photonics technology letters, vol 2, p 56, 1990

[33] D. Kuhl, F. Hieronymi, E. H. Bottcher, T. Wolf, A. Krost and D. Bimberg, "Very high speed MSM InGaAs:Fe photodetectors with InP:Fe barrier enhancement layer grown by low pressure metalorganic chemical vapor deposition", Electron letters, vol. 26, p 2107, 1990

[34] J. B. D. Soole, H. Schumacher, "InGaAs MSM photodetectors for long wavelength optical communications", IEEE Journal of quantum electronics, 27 (3): 737-752, 1991

[35] N. A. Shekhovtsov, A. A. Mishnev, "Influence of a magnetic-field on current-Voltage characteristics of Germanium MSM and P+-Semiconductor-Metal Structures", Soviet Physics Semiconductor-USSR, 9 (1): 73-74 1975

[36] L. Colace, G. Masini, F. Galluzzi, G. Assanto, G. Capellini, L. Di Gaspare, E. Falange and F. Evangelisti, "Metal-Semiconductor-Metal near infrared Light detector based on epitaxial Ge/Si", Applied Physics Letters 72 (24): 3175-3177, 1998

[37] D. Buca, S. Winnerl, S. Lenk, C. Buchal, S. Mantl and D. X. Xu, "Metal-Germanium-Metal ultrafast infrared detectors", Journal of applied physics, 92 (12):7599-7605, 2002

[38] M. Rouviere, L. Vivien, X. Le Roux, J. Mangeney, P. Crozat, C. Hoarau, E. Cassan, D. Pascal, S. Laval, J. M. Fedeli, J. F. Damlencourt, J. M. Hartmann and S. Kolev, "Ultrahigh speed germanium-on-silicon-on-insulator photodetectors for 1.31 μm and 1.55 μm operation", Applied Physics Letters, 87 (23): Art. No. 231109 DEC 5 2005

[39] S. Nakamura, Y. Mukai, M. Senoh, "Candela-class high brightness InGaN/AlGaN Double-heterostructure blue-light-emitting diode", Applied physics letters, 64 (13): 1687-1689, 1994

[40] Z. Fan, S. N. Mohammad, W. Kim , O. Aktas, A. E. Botchkarev, K. Suzue, H. Morkoc, K. Duxstad and E. E. Haller, " Ohmic contacts and Schottky barriers to n-Ga-N", Journal of electronic materials, 25 (11): 1703-1708, 1996

[41] J. C. Carrano, T. Li, P. A. Grudowski, C. J. Eiting, R. D. Dupuis and J. C. Campbell, "Comprehensive characterization of MSM ultraviolet detectors fabricated on single crystal GaN", Journal of applied physics, 83(11): 6149-6160 1998

[42] S. N. Mohamad, A. A. Salvador, H. Morkoc, "Emerging GaN based devices", Proceeding of the IEEE 83(10):1309-1355, 1995

[43] D. Walker, E. Monroy, P. Kung, J. Wu, M. Hamilton, F. J. Sanchez, J. Diaz and M. Razeghi, "High-speed, low-noise metal-semiconductor-metal ultraviolet photodetectors based on GaN", Applied Physics Letters 74(5): 762-764, 1999

[44] J. Li, W. R. Donaldson and T. Y. Hsiang, "Very fast MSM ultraviolet photodetectors on GaN with submicron finger width", IEEE Photonics technology letters, 15 (8): 1141-1143, 2003

[45] J. Li, Y. Xu, T. Y. Hsiang and W. R. Donaldson, "Picosencond response of GaN MSM photodetectors", Applied physics letters, 84 (12):2091-2093, 2004

[46] M. Mikulics, M. Marso, P. Javorka, P. Kordos, H. Luth, M. Kocan, A. Rizzi, S. Wu and R. Sobolewski, "Ultrafast metal-semiconductor-metal photodetectors on low-temperature-grown GaN", Applied Physics Letters, 86 (21): Art. No. 211110, May 2005

[47] S. Butun, T. Tut, B. Butun, M. Gokkavas, H. B. Yu and E. Ozbay, "Deep-ultraviolet Al0.75Ga0.25N photodiodes with low cut-off wavelength", Applied Physics Letters, 88 (12): Art. No. 123503 Mar 2006

[48] T. K. Lin, S. J. Chang, Y. K. Su,Y. Z. Chiou, C. K. Wang, S. P. Chang, C. M. Chang, J. J. Tang and B. R. Huang, "ZnSe MSM photodetectors prepared on GaAs and ZnSe substrates", Materials Science and Engineering B-Solid State Materials for advanced Technology, 119(2): 202-205, 2005

[49] S. J. Chang, T. K. Lin, Y. K. Su, Y. Z. Chiou, C. K. Wang, C. M. Chang and B. R. Huang, "ZnSe Homoepitaxial MSM photodetectors with various transparent electrodes", Materials Science and Engineering B-Solid State Materials for advanced Technology, 127 (2-3): 164-168 FEB 25 2006

[50] T. K. Lin, S. J. Chang, Y. K Su, B. R. Huang, M. Fujita and Y. Horokoshi, "ZnO MSM photodetectors with Ru contact electrodes", Journal of Crystal Growth, 281(2-4): 513-517, 2005

[51] W. I Milne, "Electronic devices from diamond-like carbon", Semiconductor Science and Technology 18 (3): S81-S85 Suppl. S Mar 2003

[52] S. C. Binari, M. Marchywka, D. A. Koolbeck, H. B. Dietrich and D. Moses, "Diamond Metal-Semiconductor-Metal ultraviolet photodetectors", Diamond and Related Materials 2 (5-7): 1020-1023 Apr 1993

[53] J. Burm, K. I. Litvin, D. W. Woodard, W. J. Schaff, P. Mandeville, M. A. Jaspan, N. M. Gitin and L. F. Eastman, "High-Frequency, High-Efficiency MSM Photodetectors", IEEE Journal of Quantum electronics, 31(8), Aug 1995

[54] Y. Z. Chiou, Y. K. Su, S. J. Chang, J. F. Chen, C. S. Chang, S. H. Liu, Y. C. Lin and C. H. Chen, "Transparent TiN Electrodes in GaN Metal-Semiconductor-Metal Ultraviolet Photodetectors", Jpn. J. Appl. Phys., (41): 3643-3645, 2002

[55] K. Shirasawa, H. Takahasasi, Y. Inomata, K. Fukui, K. Okada, M. Takayaka and H. Watanabe, "Large area High efficiency Multicrystalline Silicon Solar cells", Proc. 12th European Photovoltaic Solar Energy conference, Amsterdam, pp. 757-760, 1994

[56] A. K. Sharma, S. H. Zaidi, P. C.Logofatu and S. R. J. Brueck, "Optical and electrical properties of nanostructured metal-Silicon-metal photodetectors", IEEE Journal of Quantum electronics, 38 (12): 1651-1660 Dec 2002

[57] R. H. Yuang, J. L. Shieh, J. I. Chyi and J. S. Chen, "Overall performance improvement in GaAs photodetectors by using recessed-cathode structure", IEEE Photonics Letters, 9(2):226-228 Feb 1997

[58] J. Burm, K. I. Litvin, W. J. Schaff and L. F. Eastman, "Optimization of High-Speed Metal-Semiconductor-Metal Photodetectors", IEEE Photonics Technology Letters, 6(6):722-724, 1994

[59] E. H. Bottcher, E. Drogue, A. Strittmatter, "Polarisation-insensitive high-speed InGaAs Metal-Semiconductor-Metal Photodetectors", Electronics letters 33(10):912-914, 1997

[60] M. S. Unlu, S. Strite, "Resonant-Cavity enhanced Photonic Devices", Journal of Applied Physics, 78(2): 607-639, 1995

[61] Z. M. Li, D. Landheer, M. Veilleux, D. R. Conn, R. Surridge, J.M. Xu and R. I. McDonald, "Análisis of a Resonant-Cavity enhanced GaAs/AlGaAs MSM Photodetector", IEEE Photonics Technology letters, 4(5):473-476, 1992

[62] S. Collin, F. Pardo, J. L. Pelouard, "Resonant-Cavity-enhanced subwavelength Metal-Semiconductor-Metal photodetector", Applied Physics letters, 83(8): 1521-1523, 2003

[63] X. Y. Chen, B. Nabet, F. Quaranta, A. Cola and M. Currie, "Resonant-cavity-enhanced heterostructure metal-semiconductor-metal photodetector", Applied Physics letters, 80(17):3222-3224, 2002

[64] A. Strittmatter, S. Kollakowski, E. Droge, E. H. Bottcher, D. Bimberg, "High speed, high efficiency resonant-cavity enhanced InGaAs MSM photodetectors", Electronics letters, 32(13):1231-1232, 1996

[65] K. Kishino, M. Yonemaru, A. Kikuchi and Y. Toyoura, "Resonant-cavity-enhanced UV metal-semiconductor-metal (MSM) photodetectors based on AlGaN system", Physics Status Solidi A-Applied research, 188(1):321-324, 2001

[66] Y. M. Wong, D. J. Muelner, C. C. Faudskar *et al.* , "Technology development of a high density 32-channel 16-GB/s optical-data link for optical interconnection applications for the optoelectronic technology consortium", Journal of Lightwave technology, 13(6):995-1016, 1995

[67] S. Verghese, K.A. McIntosh, E.R. Brown, "Highly tunable fiber-coupled photomixers with coherent terahertz output power", IEEE transactions on microwave theory and techniques 45 (8):1301-1309 Part 2, 1997

[68] S. Verghese, K.A. McIntosh, E.R. Brown, "Optical and THz power limits in the low-temperature-grown GaAs photomixers", Applied Physics Letters, 71(19):2743-2745, 1997

[69] T. Chau, N. Kaneda, T. Jung, A. Rollinger, S. Mathai, Y. Oian, T. Itoh, M. C. Wu, W. P. Shillue and J. M. Payne, "Generation of mm waves by photomixing at 1.55 μm using InGaAs-InAlAs-InP velocity matched distributed photodetectors" IEEE Photonics technology letters 12(8):1055-1057, 2000

[70] H. Schumacher, J.B.D. Soole, R. Esagui, H.P. Leblanc, R. Bhat, M.A. Koza, "High speed waveguide photodetector on InP" Applied physics letters, vol.55:2173-2175, 1989

[71] J. B. D. Soole, H. Schumacher, H. P. Leblanc, M. A. Koza, R. Bhat, "Butt-coupled InGaAs MSM waveguide photodetector formed by selective area regrowth", Applied physics letters, vol.56:1518-1520, 1989

[72] J. Payne, B. Shillue and A. Vaccari, "Photonic Local Oscillator System", MMA Project Book, Chapter 7, Section 1, 1999

Chapter 4

Fabrication Techniques

This chapter covers all the techniques used in the fabrication of tthe devices carried out in the David Bullett Nanofabrication Laboratory and the Terahertz Technology Laboratory at the University of Bath. The techniques described in this chapter will be referred to in following chapters in the description of the fabrication processes investigated and developed for successful production of various device prototypes. The information contained in this chapter was obtained from the bibliography provided in Appendix I and from our own research.

4.1 Cleaning Procedures

In all semiconductor processing, it is essential to ensure the wafer surface, tools and working environment are as clean as possible. If impurities are present on a wafer surface during certain stages of the processing, it can lead to imperfect devices, and therefore to poorer performance and lower yields. Given the budget restrictions of this research project, it was key to minimise the waste of material. The David Bullett Nanofabrication Laboratory has a rating of 1000, i.e. less than 1000 particles larger than 1μm per cubic feet.

The typical wafer cleaning procedure involved the sequential immersion in trichloroethane, acetone and isopropanol (IPA) for removing grease, oils and organic impurities. This recipe is even more effective if the solvents are heated, typically up to 60°C and ultrasound bath is used. Diluted acid solutions were used when further cleaning was required.

4.2 Photolithography

With the exception of the photomixers, the patterning of the rest of the features required for this project was done using contact optical lithography. In this technique the semiconductor is coated with photosensitive material, brought into contact with a photomask and exposed through it to a strong ultraviolet light source.

4.2.1 Photolithography masks

Standard photolithography masks consist of a fused-silica substrate covered with a patterned chromium film. A photomask was designed using a standard CAD software package and then produced by Compugraphics International Ltd. by electron beam lithography. The mask included all the features required for the production of all the prototypes described in this work. There are three groups of cells that correspond to the different steps for the production of transmission lines, MSM chips and filter chips.

The 10 mm x 5 mm cells for the fabrication of the 34 GHz prototypes chips are shown in Figure 4.1. From left to right the cells correspond respectively to alignment marks, straight coplanar waveguide (CPW), tapered CPW and groove etching window. Note that other etching windows cells are not included in the figure.

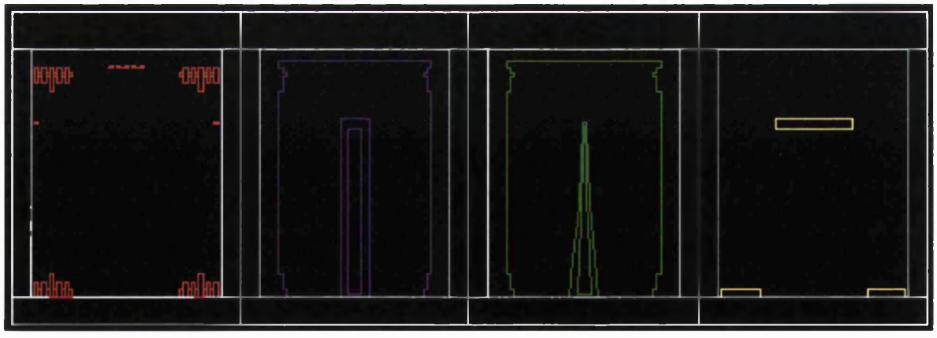

Figure 4.1 Photolithographic cells (10 mm x 5 mm) for 34 GHz transmission lines.

In Figure 4.2 the 10 mm x 10 mm cells for the fabrication of individual MSM chips are shown, each layer corresponds to a different photolithographic stage in the process. Not that not all layers are shown for more clarity.

1- Frame window (white layer)

2- Global and Local alignment marks (red layer)

3- Connecting pads (green layer)

4- Registration marks for back alignment (yellow and blue layer)

5- Thick grid for chip separation via dry etching (purple layer)

6- Thin grid for chip separation via wet etching (not shown)

7- Membrane windows (turquoise layer)

8- Antireflection coating etch (not shown)

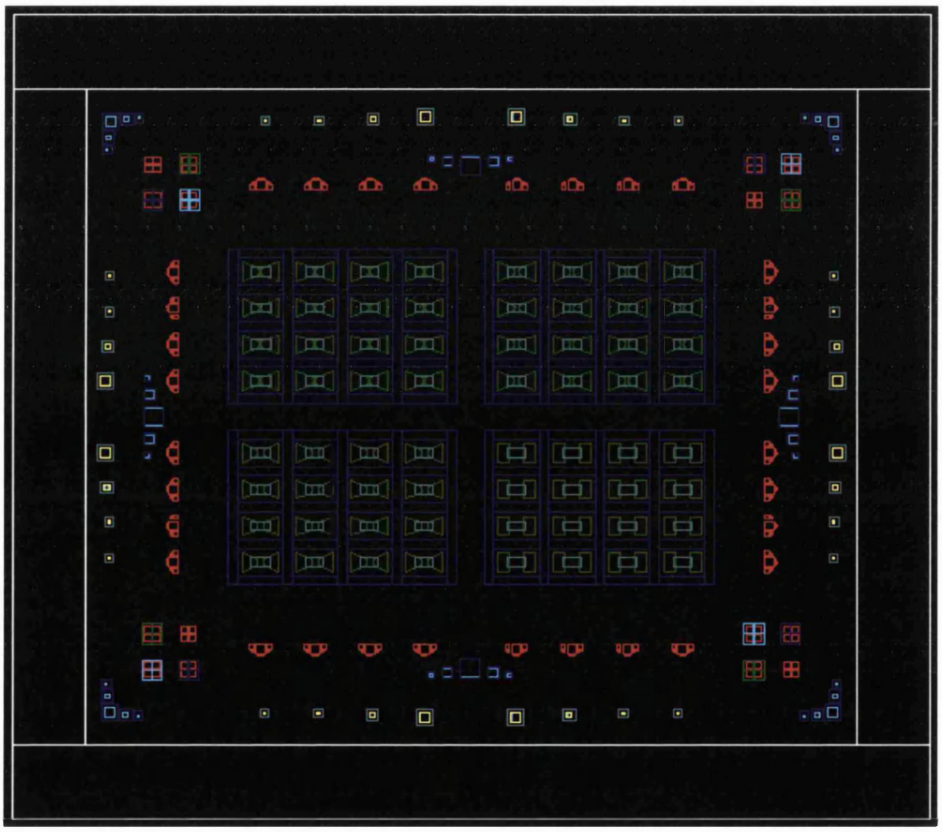

Figure 4.2 Photolithographic cells (10 mm x 10 mm) for MSM chip fabrication.

The filter chip cell shown in Figure 4.3 includes four 3-element hammerhead filters for blocking 100 GHz, four 5-element hammerhead filters for blocking 200 GHz, parallel strip lines for electro optical characterization of MSMs and 4 filters for other

applications not concerned with this research project. Alignment marks for mechanical chip separation are included in the cell.

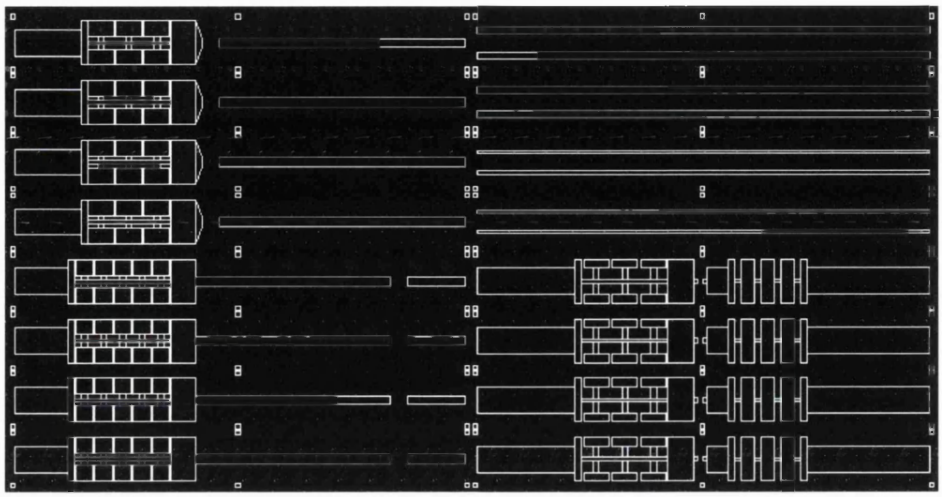

Figure 4.3 Photolithographic cells of 100 GHz and 200 GHz blocking filters and parallel striplines.

Photographic film was used as a photolithographic mask in different stages of development of the fabrication process as it is quick and cheap to produce. The negative images of that desired on the mask were drawn in a conventional CAD program, printed on paper and photographed with an SLR camera. After development, the negatives were adhered to a transparent glass and used as a mask. This technique proved successful in the production of various transmission lines, contacting pads and etching masks.

This technique has the inherent limitation of resolution of the grain size of the film, as well as being problematic to achieve optimum contact with the photoresist due to film bending. Nevertheless, it proved a very useful complement to conventional photolithography masks, as it reduces dramatically time and cost constraints. The film used for such masks was Kodalith ASA 8 as it was the smallest grain size available.

4.2.2 Process

Contact photolithography is quick and relatively easy and, with the correct resist and recipe, patterns down to 1 μm can be obtained. The success of this technique relies on using the correct resist thickness, ensuring adequate contact between resist and mask, and calibration for optimum exposure and developing time.

The main photoresist used was Shipley 1813. Such resist when spun at 3500 rpm and baked 60 seconds at 115ºC giving thickness 1.5 μm requiring a dose of 120 mJ/cm^2. The developer used was Microposit 351 diluted 3.5:1 in deionised water. The development time was 40 seconds and the sample thoroughly rinsed in water for removing totally the exposed resist.

Two different lift off enhancement techniques were used in the course of this project. Both techniques rely on the same principle of achieving an undercut profile for ensuring that the metallisation on the semiconductor and the metal on top of the resist are not connected.

The first of the methods consists of using a thin bottom layer of lift off resist (Microchem LOR-B) and a top layer of 1813. As the sensitivity of the LOR-B is much higher than the resist on top, the resultant profile is as shown in Figure 4.4 a). The size of the undercut is controlled by the baking temperature and development time. The other method is the immersion of the sample in chlorobenzene (typically one minute) that induces the hardening of the top layer of the resist. The schematic of the undercut profile is shown in Figure 4.4 b). This second method has the inconvenience of having less control over the size of the undercut.

Figure 4.4 Representation of undercut profile after evaporation using a)LOR- B b)Chlorobenzene.

4.3 Electron Beam Lithography

Electron Beam Lithography (EBL) is the technique that was used for the fabrication of the fingers and small contacting pads of the photomixers. This technique consists of the acceleration and focusing of electrons to a beam and scanned over a wafer covered with a thin film of electron sensitive resist.

In this technique the digital pattern is transferred directly to the resist without the need of a mask, therefore it achieves much higher resolution than photolithography as it avoids light diffraction limitation. The smallest finger width fabricated during this project to fingers is 100 nm. The main constraints of the EBL system are the exposure speed, the reliability of the system and the high costs of its use.

4.3.1 EBL System

The EBL System used in the course of the research consists of a HITACHI scanning electron microscope converted into a lithography system using RAITH software for controlling the exposure processes. The part of the system that creates and focuses the beam of electrons is known as the *column*. The main elements in the column together with the anti-vibration table are shown in Figure 4.5:

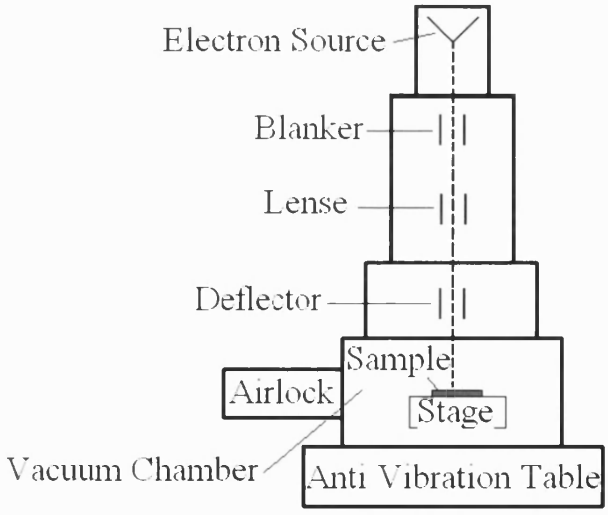

Figure 4.5 Schematic arrangement of the main elements in the column.

- Electron Source: electron sources work either by thermal excitation of electrons in a conductive material to a level that they gain energy enough to overcome the potential barrier (*thermionic emission*) or by applying an electromagnetic field strong enough to make the carriers tunnel across the barrier (*field emission*).

- Lenses: They are used to focus the beam as they travel through the column. They can use electrostatic or magnetic forces. They suffer spherical and chromatic aberrations that are minimized by confining the beam in the smallest possible spot, at the cost of reducing the brightness (current) of the beam. The size of the spot on the sample ranges 1.5 nm - 5 nm if the beam is well focussed.

- Blanker: The blanker is the responsible for switching the beam on and off. It consists of an electrostatic deflector. The simplest arrangement is two plates with an aperture underneath. When voltage is applied across it, the beam is swept off the acceptance of the aperture. The high-speed operation of the blanker is critical for achieving high resolution, as during the time that the shutter is still open the sample will still be exposed. Therefore, for accurate exposure of fine feature doses, the blanker switching time must be as short as possible; in our system it is 0.375 ns.

- Deflector: This is the responsible for deflecting the beam producing the scanning across the surface of the sample. It can perform the deflection magnetically or electrostatically.

The column and the stage chamber are maintained at high vacuum (of the order of 10^{-5}mbar) for ensuring good performance. The *stage controller* is responsible for moving the sample towards the beam for optimum working distance and for loading and unloading operations.

Details of the electron beam pattern exposure can be found in the Elphy manual in the Appendix I. The basic steps consist in loading the sample, calibration of current of the beam, global alignment, local alignment and exposure of patterns.

4.3.2 Electron beam Resists

The resist is a material that when exposed by the electron beam undergoes some physical changes. Normally the resist consist in a polymer dissolved in a solvent. If the electrons provoke a breakdown of the polymer chains it is said to be a *positive resist*. In this case the exposed area becomes soluble in the appropriate developer. On the other hand, if the electrons induce cross-linking of the polymer chains it is said to be a *negative resist*. Negative resist becomes insoluble to certain solvents. These two types of resists are illustrated in Figure 4.6:

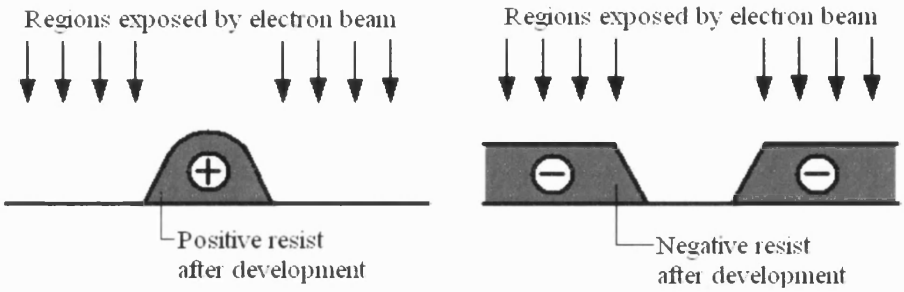

Figure 4.6 Remaining resist after development for positive and negative resist.

The main resist used during this work was the most common and studied resist, the *polymethyl-methacrylate* (PMMA). It is a resist that behaves as positive for low doses and as negative for high doses (of the order of ten times the dose for positive behaviour). The other resist used during the course of our research is the PMMA-MMA, a copolymer of PMMA used in a double layer technique similar to that described in the section 4.2.2

There are two important parameters for defining the quality of a resist:

Sensitivity: minimum dose required to expose through the whole layer of resist (assuming a reference thickness of the layer). High sensitivities bring normally a decrease in the resolution.

Contrast: is defined as $|log_{10}(D_1/D_2)|^{-1}$, where D_1 is the critical dose and D_2 is the sensitivity. For higher contrast, the walls of the exposed patterns will be more vertical.

A table with typical values for the used resists is shown:

Resist	Type	Resolution (nm)	Sensitivity ($\propto$ C/cm^2)	Contrast
PMMA	+/-	10	100/1000	Low
PMMA -MMA	+	100	10	Low

Table 4.1 Characteristics of resists used

The developer that provided the best resolution is a 1:3 solution of Methyl isobutyl ketone (MIBK) in IPA.

4.3.3 Electron-Sample interaction:.

The interaction between electrons and solids has been widely studied in the past by means of *Monte-Carlo simulations*. The modelled paths that electrons travel in the material for two different acceleration voltages are shown in Figure 4.7:

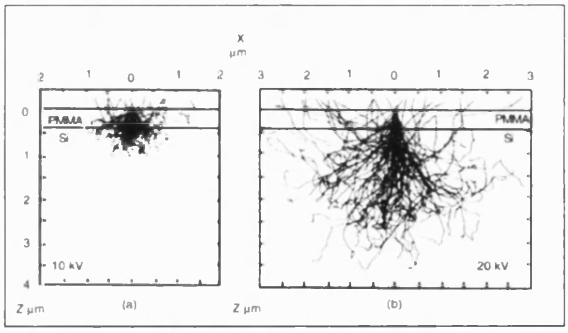

Figure 4.7 Monte Carlo simulation for electron scattering in silicon samples at 10 kV and 20 kV Kyser and Viswanathan [1].

Ideally when the beam of electrons arrive in the film of resistive material, it induces physical changes only in the exposed areas. However, scattering effects that occur to the electrons when travelling through the material provoke the exposure outside the desired area. If the electrons suffer scattering in small angles, they are said to be *forward scattered.* If those angles are large, they are said to be *back scattered.*

The high energy electrons in the beam are referred to as *primary electrons*. As the electrons cross the resist, their kinetic energy is transferred to it generating low

energy electrons (between 2 and 50 eV) called the *secondary electrons*. These are the responsible for the exposure of the most of the resist.

Experimentally the number of backscattered electrons is found to be independent of the beam energy. The most important factor that influences the intensity of the backscattering is the substrate composition. When an insulating material was used, the electrons of the beam will build up around the exposed area provoking a *charging up effect* that dramatically increases the number of backscattered electrons, therefore affecting the resolution. In order to avoid the charging up effect, a conducting path for the electrons had to be provided, i.e. metallic wire in contact with the surface.

The forward scattering provokes a broadening of the exposed pattern at the bottom of the resist as the electrons divert slightly from their original direction. The empirical expression that relates the widening of patterns due to forward scattering is given by [2]:

$$d_f = 0.9\ (R_t / V_{acc})^{1.5} \tag{4.1}$$

Where d_f is the increase in the diameter of the beam in nanometres, R_t is the thickness of the resist expressed in nanometres and V_{acc} is the acceleration voltage in kV. It is clear than in order to minimize this effect, the thickness of the resist must be minimized and the highest available acceleration voltage must be used. This is the main reason for using higher voltages for higher resolution when thin layers were not desirable.

As the forward scattered electrons broaden the effective diameter of the beam at the bottom of the resist, the backward scattered electrons will travel far away from the incident point. That means that those electrons will effectively expose areas surrounding the desired pattern. This effect is known as the *proximity effect*. The primary electrons are the principal cause of this effect as they travel much longer distances than the secondary electrons (typical values for average transit distances of secondary electrons are a few nanometres). Proximity effect correction techniques used in this project are described in Chapter 5.

4.3.4 Process

A necessary consideration when operating an EBL system is the requirement for alignment marks on the sample. Alignment marks are size-known metal features that are used for calibration of the relative position of the sample with respect to the stage (*global marks*) and for relative position of devices with respect to the sample (*local marks*). They are generally patterned on the samples via optical lithography.

Global alignment marks are generally large features with respect to the exposed patterns. The relative position of the sample with respect to the beam is of major importance as it will determine the distances swept on the surface that correspond to certain angles swept by the beam. Local alignment marks are generally smaller than global marks, and they are used for fine positioning of exposed patterns. Those marks were used too for measuring the small displacement due to long exposure thermal drifts

Three different recipes were used for the production of the devices. A critical factor for the repeatability of the processes is the temperature of the resist when it is spun. Slight differences in the temperature of the PMMA will lead to slightly different thicknesses, therefore affecting the finger dose and proximity effect correction calibration

4.3.4.1 Single Layer PMMA

In the early stages of the project, devices were fabricated using a single layer of PMMA as thick as 250 nm (the limit of the used PMMA). The process consists of:

1- Clean and pre-bake
2- Spin PMMA at 4000 rpm
3- Bake 60 s at 180°C
4- E-beam exposure
5- 60 s development in MIBK:IPA 1:3

The main difficulty found with this recipe is that lift off is problematic when evaporating more than 150 nm of metal, and the maximum resolution of 300 nm was

achieved. In addition, the proximity effects were found to be very pronounced due to the small quantity of resist.

4.3.4.2 Double Layer PMMA

In order to address the problems that arose when using the first recipe, a second recipe using a double layer was investigated. The process consists of:

1- Clean and pre-bake
2- Spin PMMA at 4000 rpm
3- Bake 5 s at 180°C
4- Spin PMMA at 4000 rpm
5- Bake 60 s at 180°C
6- E-beam exposure
7- 90 s development in MIBK:IPA 1:3

This recipe avoided the lift off problems for thick metal and achieved much higher resolution. With this recipe, fingers of width as small as 100 nm were fabricated.

4.3.4.3 Double layer of PMMA and PMMA-MMA

The third technique used is a double layer of PMMA and PMMA-MMA, similar to that used for the fabrication of T-gates [3], but with an inversion of the layers. The difference in sensitivity between the top layer of copolymer and the bottom layer of PMMA produces an undercut similar to that described in Section 4.2.2 providing better lift off results. The process consist of:

1- Clean and pre-bake
2- Spin PMMA-MMA at 4000 rpm
3- Bake 5 s at 180°C
4- Spin PMMA at 4000 rpm
5- Bake 60 s at 180°C
6- E-beam exposure
7- 90 s development in MIBK:IPA 1:3

This fabrication process was extended including a metal layer between the copolymer and the PMMA and an additional wet etch after e-beam exposure. The fabrication steps for this extended process are shown in Figure 4.12:

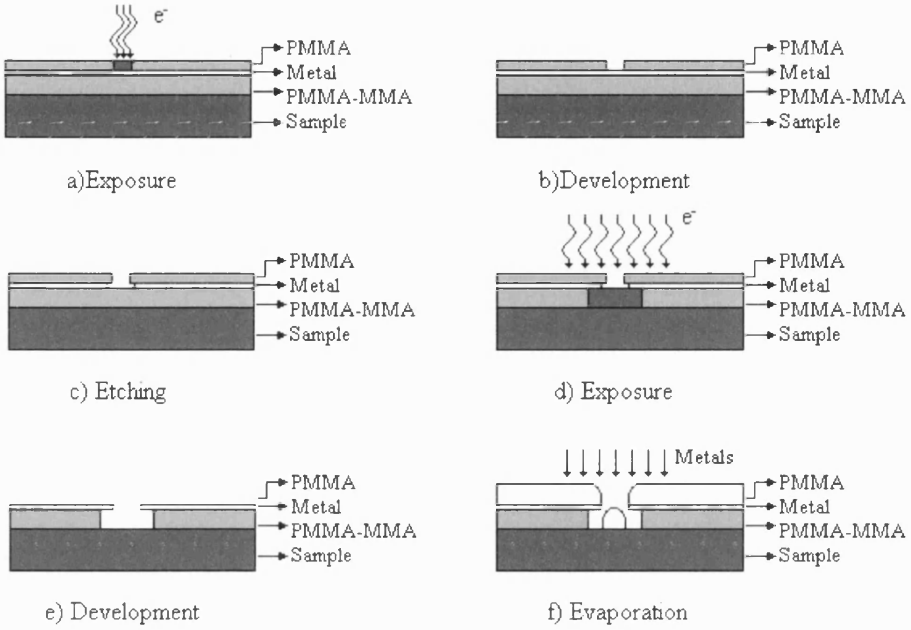

Figure 4.12 Fabrication steps for trilayer PMMA-MMA / Metal / PMMA) technique

4.4 Metal deposition

The deposition of metals onto a substrate was performed using an Edwards 306 thermal evaporator and an Edwards e-Beam evaporator. In the thermal evaporator high current is applied through the tungsten boat, containing the metal to be evaporated, rising the temperature to the melting point. Once this point is reached, the metal begins to evaporate upwards in the vacuum chamber depositing on the sample. The rate at which the metal is deposited is controlled by varying the applied voltage, and monitored by the variation of vibration of a piezoelectric crystal inside the cavity. The e-beam operates in a similar manner, with the difference that the melting point is achieved by firing a high energy electron beam onto a graphite crucible where the metal is placed.

4.5 Wet Etching

Wet etching refers to the removal of material by immersion in a solution that chemically reacts with the substrate. This technique was used for removing protective layers of SiO_2, thinning wafers, etching grooves for mounting, grids for chip separation and membrane formation. Some recipes and etch rates obtained for different materials are shown in Table 4.2:

Etchant	Solution	Material	Etch rate	Use
$HF:H_2O$	1:3	SiO_2		Protective layer etch
$H_2SO_4:H_2O_2:H_2O$	1:8:20	GaAs	1 μm/min	Grooves and grids
$HNO_3:H_2O_2:H_2O$	7:10:3	GaAs	5 μm/min	Thinning chips
Citric Acid:H_2O_2	5:1	GaAs	0.25 μm/min	Membrane formation
	5:1	AlGaAs	0.003 μm/min	Etch stop layer
$HF:H_2O$	1:3	Si		Sacrificial Chips

Table 4.2 Wet etch recipes

Note that the citric acid solution was made by dissolving anhydrous citric acid (powder) in water in a proportion of 1gr/ml. As variations in temperature or stirring method change slightly the etch rates, the values shown in the table are the average of those obtained in successive etch tests.

4.6 Wafer Lapping

Mechanical lapping of the back of the chip after all front-side processing was performed for the separation of individual MSMs chips (Process described in Chapter 7). The lapping was performed using a Logitech PM5 grinding/ polishing jig and grinding was performed on a glass plate using an alumina solution seeded with 3 μm particles. The roughness of the finished surface is much better than that obtained with chemical etching, making possible further processing on the back of the chip.

4.7 Profiling

During different stages of the processing it was required to accurately know the profile of the surface. A Dektak surface profiler with a vertical accuracy of 100 nm was used for this purpose. In this machine, a sharp diamond tipped needle is positioned on the starting point on the chip using a mechanical stage, and then driven across the sample. The microactuators connected to the tip respond to the vertical movement resulting in small voltage fluctuations, that then are transmitted to the computer for monitoring. Automated scanning software applications were used for the generation of 3D models of the inspected chips.

The profiler was used to measure thicknesses of resist, surface roughness, etched profiles, relative angle between surfaces, and for the calculation of etching rates and selectivity.

4.8 Soldering and Mounting

Once the semiconductor chips were fabricated they had to be mounted and electrically connected. Wax and cyanoacrylate were used for fixing the position of the chips, with the advantage of being easily removed with solvents.

The electrical connections were made using silver paint and conductive epoxy. The silver paint has the main disadvantage of having low viscosity, therefore is easily absorbed by capillary effect in between the chips, increasing the risk of short circuiting the devices. Its main advantage is that can be easily removed using acetone and IPA. Epoxy has much higher viscosity, making it much easier to handle, but has the disadvantage of being very difficult to remove after curing.

References:

[1] D. F. Kyser and N. S. Viswanathan, "Monte-Carlo simulation of spatially distributed beams in Electron-Beam Lithography" Journal of Vacuum Science and Technology, 12 (6): 1305-1308, 1975

[2] P.Rai-Choudhury "Handbook of Microlithography, micromachining and micro fabrication", vol 2, SPIE Press, 1997

[3] S. C. Kim, B. O. Lim, H. S. Lee, D. H. Shin, S. K. Kim, H. C. Park and J. K. Rhee, "Sub-100 nm T-gate fabrication using a positive resist ZEP520/P(MMA-MAA)/PMMA trilayer by double exposure at 50 kV e-beam lithography", Materials Science in semiconductor processing, 7 (1-2): 7-11, 2004

Chapter 5

14, 34 and 50 GHz photomixers

This chapter covers the design, modelling, fabrication and testing of the prototypes for operation at frequencies up to 60 GHz carried out in the David Bullett Nanofabrication Laboratory and the Terahertz Technology Laboratory at the University of Bath.

5.1 Design and modelling

These devices were to be used as a direct substitute for a commercial InGaAs photomixer operating at 14 GHz and 34 GHz in the CR-ESR spectroscopy system described in Section 2.4. During this project ensuring the speed performance of the devices was of higher priority than achieving high values of quantum efficiency as the optical heterodyne detection system can detect signals incoming from photodiodes with very poor responsivity [1].

5.1.1 MSM design and modelling

The design process consisted of the selection of material and the calculations of the sizes of the detectors that would ensure the satisfactory operation for our high-speed requirements.

In the first steps of the design process, GaAs was found to be the most suitable material for its good absorption in the region 400 nm-800 nm where the spectroscopy experiment operates. As seen in Chapter 3, the choice of LTG GaAs over conventionally grown GaAs presents further advantages for high-speed applications, such as high mobility, high saturation velocity, sub-picosecond carrier lifetime and high breakdown field strength. The main parameters are shown in table 5.1:

Thermal conductivity (W/cm-°C)	0.46
Energy gap (eV)	1.435
Relative permittivity	13.1
Breakdown field strength (V/μm)	40
Carrier life time (ps)	0.3-0.5
Electron mobility (cm^2/V s)	200
Saturation velocity (μm/s)	4×10^{11}

Table 5.1 LTG GaAs Characteristics

During the annealing of LTG GaAs, the arsenide precipitates forming recombination centres that reduce the average lifetime of the carriers to the order of tenths of picoseconds [2]. Therefore, considering just the carrier lifetime, MSMs in LTG GaAs have the potential to be *recombination time limited* devices able to operate at THz frequencies. Assuming that all the carriers travel at the saturation velocity the average distance that they can cover before recombination was estimated to be 0.25 μm. As seen in Section 2.5, the distance that the carriers can travel in the recombination time must be comparable to the finger spacing for not compromising further the quantum efficiency. In order to fulfil this condition, the spacing should be 250 nm or smaller.

The evaluation of the term [1-exp(-αd)] in Eq.(2.62) for incident wavelengths between 400 nm and 850 nm for a layer 0.25 μm thick, yielded values from 0.95 to 0.1. Therefore the epilayered structure chosen was an undoped LTG GaAs active layer 1 μm thick over a half a micrometer layer of AlGaAs grown over 400 μm layer of bulk GaAs. The values of the predicted quantum efficiency for different shadowing ratios, assuming that the only carriers collected are those that travel a distance shorter than 250 nm, are shown in Figure 5.1:

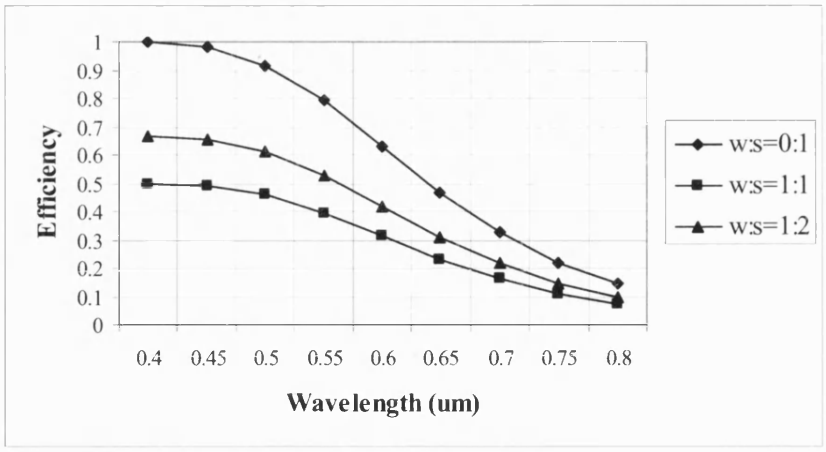

Figure 5.1 Theoretical quantum efficiency vs. wavelength for LTG GaAs MSMs with different width : spacing (w:s) ratios, accounting shadowing effects and carrier recombination before collection

Due to the short recombination time of LTG GaAs, the detectors of suitable dimensions for our application were found to be RC time-constant limited. In order to evaluate the intrinsic instantaneous bandwidth of different devices and the effect of the parasitic elements, an equivalent circuit model was used. From the electrical length of the detector circuit, it was estimated that the lumped element modelling is valid up to about 100 GHz. For higher frequencies a distributed element approach is necessary. The circuit analysis was performed using Serenade Harmonica circuit simulator [3].

The equivalent circuit modelling was carried out in two stages. The first stage was the modelling of the intrinsic characteristics of the MSM devices; subsequently elements of the extrinsic circuit were included for a better understanding of the effects of parasitic elements on the instantaneous bandwidth of the devices. The intrinsic and extrinsic MSM elements are represented by the equivalent circuit shown in Figure 5.2 [4]:

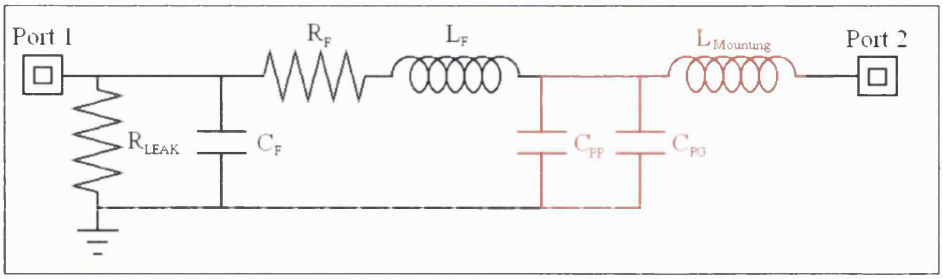

Figure 5.2 Equivalent circuit representing the intrinsic response of MSMs (elements in black) and extrinsic response including parasitic elements (elements in red).

In the intrinsic equivalent circuit model, R_{LEAK} represents the resistance between the two contacts, C_F is the capacitance between the fingers, R_F is the resistance of the fingers in parallel and L_F is the inductance of the fingers. The extrinsic elements C_{PP} and C_{PG} represent the capacitance between the contacting pads and between the pads and the ground plane respectively. The $L_{MOUNTING}$ represents the inductance of the epoxy or silver paint bonding. Note that Port 2 represents a load resistance of 50 ohms. The impedance of Port 1 was set as 50 ohms.

The capacitance between the interdigitated contacts was calculated using Eq.(2.61) for a range of sizes. An example of the obtained results is shown in Figure 5.3. Note that these values of the capacitance refer to the values under no bias. When there is a bias voltage, the active region is depleted and the capacitance is reduced (results shown in section 5.3).

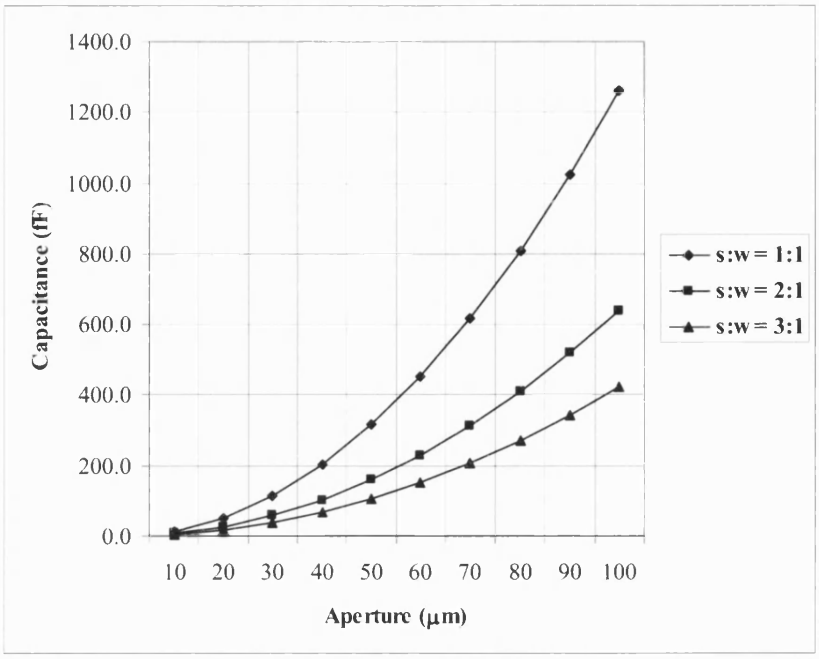

Figure 5.3 Theoretical interdigital capacitance (C_F) versus aperture for MSMs with fingers 0.25 μm wide and different spacing:width ratios.

Our tests showed that C_{PP} and C_{PG} are of the order of 5 fF and 1 fF respectively. R_{LEAK} is the resistance across the interdigitated metallisations and is of the order of GΩ. The L_F is the inductance of the fingers ranging from a pH to tens of pH depending on the finger length.

The resistance is generally dominated by the load resistance (R_{LOAD}, typically 50 Ω). As seen in Chapter 2, due to scattering processes, the value of R_F deviates from that predicted by the bulk resistance. Therefore, correction coefficients must be used for different sizes of fingers. Assuming an aperture and a finger size, the minimum number of fingers that a detector should have for R_F not to dominate over the load resistance can be calculated using Eq.(2.59). Figure 5.4 illustrates the relationship between the number of fingers and R_F for detectors with finger length 12 μm; note that the experiments for the calculation of the correction coefficients utilised for plotting this graph are described in Section 5.3.

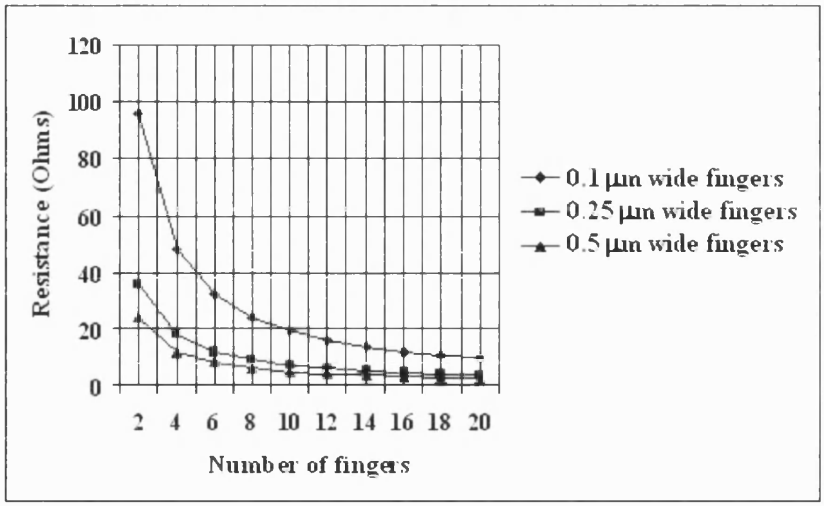

Figure 5.4 Theoretical estimation of R_F versus the number of fingers of MSM devices with fingers 12 µm long and 200 nm thick.

The value of R_F when operating at high frequency may differ from that measured at dc, but as the thickness of the fingers is smaller than the skin depth (approximately 415 nm at 34 GHz), the estimated values are assumed to be a good approximation.

Modelling of the equivalent circuit yielded that the elements responsible for major delays in the time response of the circuit are C_F, R_F and L_F. Therefore in order to achieve the maximum responsivity those three values must be minimised.

In order to illustrate the results obtained by modelling, consider an MSM with 14 fingers 0.3 µm wide spaced 0.3 µm, covering an area of 10 µm x 10.6 µm. Using Eq. (2.61), the capacitance of the device is estimated to be 20 fF, R_F is estimated to be 5 Ω, and the inductance of the fingers is assumed to be 1 pH [4]. The equivalent circuit model suggests that the intrinsic 3 dB bandwidth of this device should be well over 200 GHz. Nevertheless, the epoxy bonding for the connection of the device will introduce an extra inductance that will reduces the 3 dB bandwidth [4]. As a limit case, circuit modelling showed that a 0.2 pH inductance reduce the 3 dB bandwidth to 75 GHz. The calculated S12 parameters for both cases are shown in Figure 5.5.

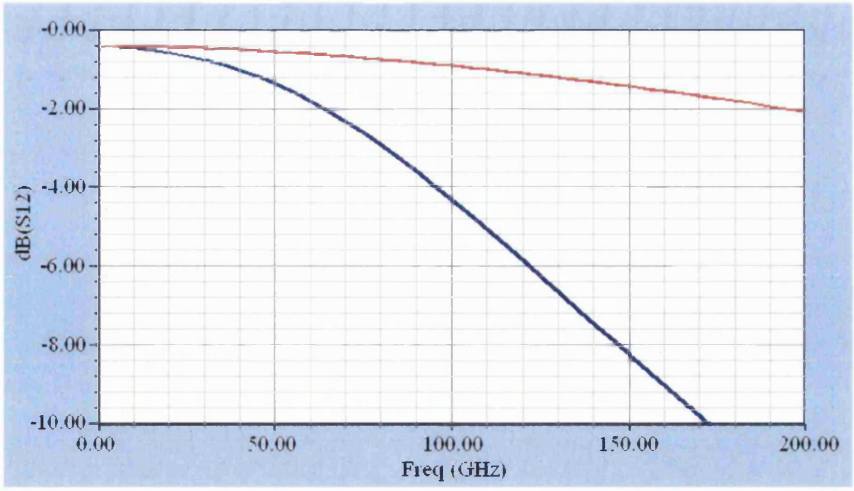

Figure 5.5 S_{12} parameters for an unmounted (red) and mounted (blue) MSM with 14 fingers 0.3 μm wide spaced 0.3 μm, of active area of 10 μm x 10.6 μm, for a Port 1 impedance of 50 Ω.

To our knowledge, there is no reference in the literature that include a formula for the estimation of the MSM impedance. Nevertheless, Verghese *et al.* have assumed that the photodetector is a current source of much higher impedance than 50 Ω [5]. To evaluate the influence of such factor in the S12 parameters, the equivalent circuit model of the same device considered in Figure 5.5 was run for Port 1 impedance values of 50 Ω, 100 Ω and 150 Ω. The result is shown in Figure 5.6:

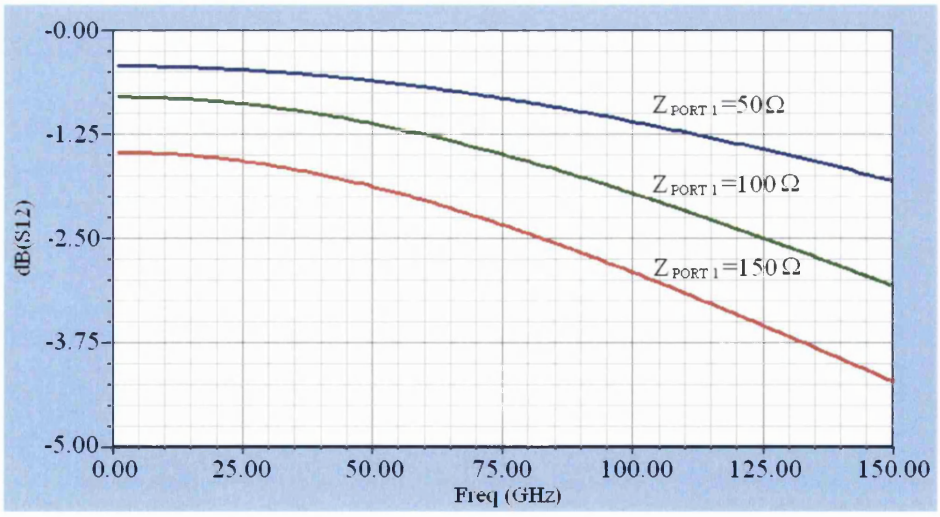

Figure 5.6 S_{12} parameters for an unmounted MSM for various Port 1 impedances.

As it can be seen in Figure 5.6, the higher the impedance of the photodetector the higher the losses due to reflections provoked by higher impedance mismatches along the circuit.

It is convenient to make an estimation of the quantum efficiency for this particular device. Assuming the Fresnel reflectivity to be 0.3, and absorption of 600 nm light in 0.25 μm thick layer (recombination transit time limit), the overall quantum efficiency is estimated to be 10%. In order to enhance the value of the quantum efficiency devices with buried and semi-buried contacts were designed, as they are able to collect carriers generated deeper in the semiconductor.

In Table 5.3 the results for the 3 dB RC limited bandwidths obtained by the equivalent circuit model are shown for a range of devices. WA (working area) refers to the area exposed by e-beam including fingers and small contacting pads, as seen in Chapter 4, this area determines the minimum finger size that can be exposed. AA (active area) refers to the active area covered by the interdigitated patterns and it is the detection area.

$WA^{1/2}$ (μm)	$AA^{1/2}$ (μm)	Finger length (μm)	Width (μm)	Spacing (μm)	C_F (fF)	Intrinsic 3dB BW (GHz)	Mounted (0.1 pH) 3dB BW (GHz)	Mounted (0.2 pH) 3dB BW (GHz)
25	15	17.5	0.25	0.25	28.4	170	115	75
25	15	17.5	0.25	0.5	14.4	280	280	82.5
25	15	17.5	0.25	0.75	9.5	380	155	82.5
25	15	17.5	0.25	1	7.1	450	160	82.5
25	20	22.5	0.25	0.25	50.5	120	90	62.5
25	20	22.5	0.25	0.5	25.6	205	120	80
25	20	22.5	0.25	0.75	16.9	260	140	82.5
25	20	22.5	0.25	1	12.7	310	150	82.5
50	30	32.5	0.5	0.5	56.8	90	80	60
50	30	32.5	0.5	0.75	38.5	130	100	70
50	30	32.5	0.5	1	28.8	167.5	115	75
50	30	32.5	0.5	1.25	23	200	125	80
50	40	42.5	0.5	0.5	100.9	52.5	52.5	45
50	40	42.5	0.5	0.75	68.4	75	70	55
50	40	42.5	0.5	1	51.2	100	90	62.5
50	40	42.5	0.5	1.25	40.8	120	100	70

Table 5.3 RC limited bandwidths calculated by the equivalent circuit model for Port 1 impedance 50 Ω.

5.1.2 CPW design and modelling

Transmission lines were designed and modelled in order to provide efficient connection of the photodetectors to the external circuit. Many commercial photodetectors typically use coplanar waveguide (CPW) for its simple planar structure, its low losses and wide bandwidth. Suspended CPW has the additional advantage of reducing the C_{FG} and C_{PG} as well as being less lossy than the grounded CPW. There are two main factors that affect the S parameters of the transmission line. These are reflections occurring along the transmission line and reflections in the connection of the transmission line to the outer connector. Both reflection mechanisms are due to impedance mismatches. Given that the outer line has an impedance of 50 Ω, transmission lines must have the same impedance along their length for the central frequency of 34 GHz. Two different types, straight and tapered, of suspended CPW were designed using TX line calculator [6], see Figure 5.7. For determining the bandwidth and losses along both types of transmission line they were modelled using High Frequency Structure Simulator (HFSS) [7].

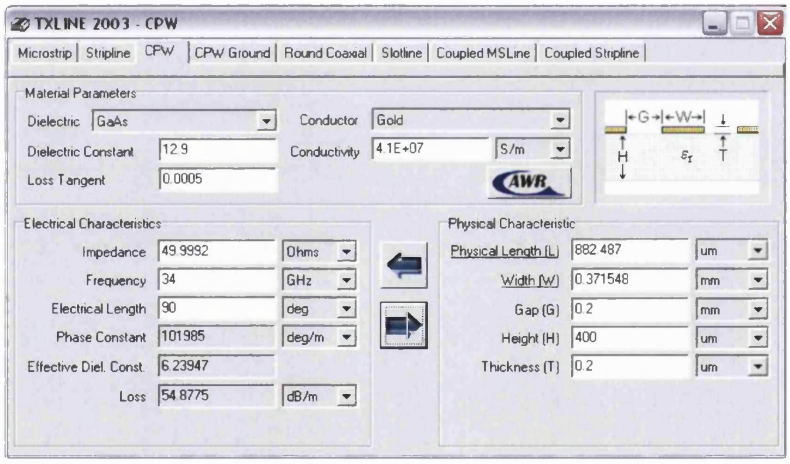

Figure 5.7 TX Line transmission line calculator.

The tapered CPW was designed for having a width/gap ratio that yields an impedance of 50 Ω ± 0.2 Ω along the line for signals at 34 GHz. This design has the main aim of minimising the reflections in the connection between the pad of the photodetector and the transmission line. In Figure 5.8 the structure simulated in HFSS and the S_{12} results are shown. The simulation was run for three modes but only the first mode was found to propagate along the line.

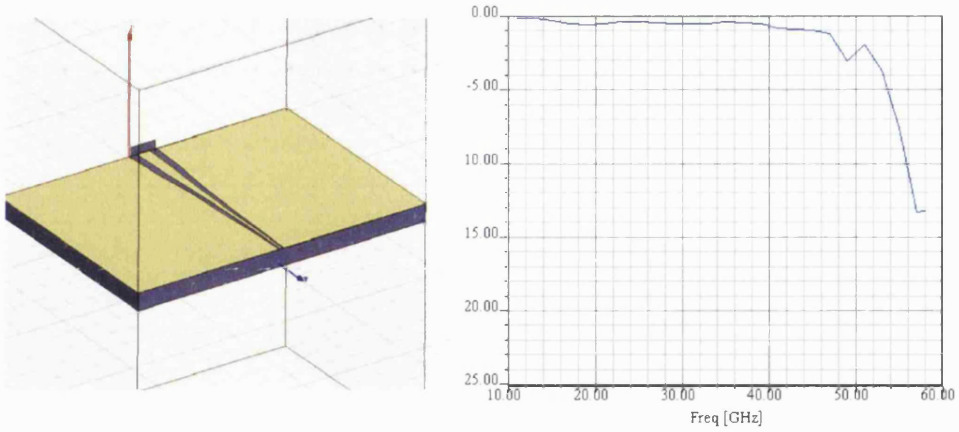

Figure 5.8 S_{12} Parameters modelled with HFSS for suspended tapered CPW.

The straight CPW yielded similar results, see Figure 5.9:

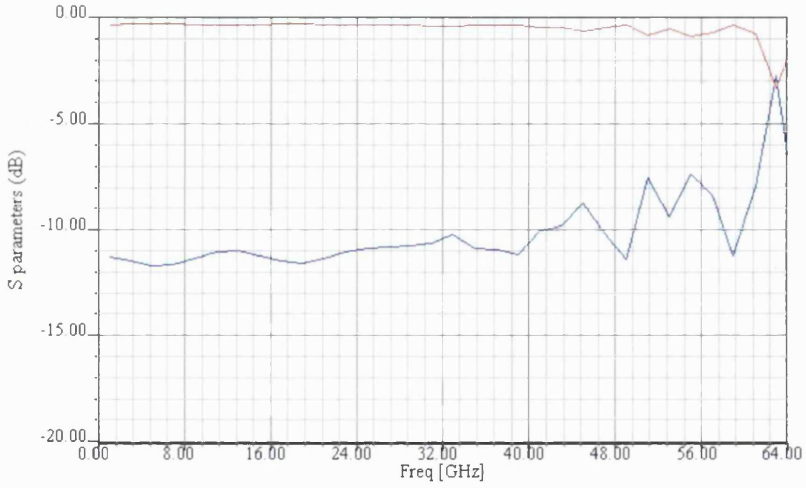

Figure 5.9 S_{12} (red) and S_{11} (blue) parameters for straight CPW.

5.1.3 Mount design

The mount was designed for a 6 mm x 10 mm x 0.4 mm chip with CPW suspended in the middle of the cavity resting in two lateral shelves as shown in Figure 5.10. A V-connector to coplanar waveguide transition (ANRITSU V115FCPW) was soldered into the brass mount for good microwave performance up to 60 GHz. The CPWs described in the previous section had dimensions chosen for the outer planes

of the transmission line to be aligned with the ground pins in the connector, as shown in the inset of Figure 5.10 to minimise reflections [8]. An V to K adapter was used for operation under 40 GHz.

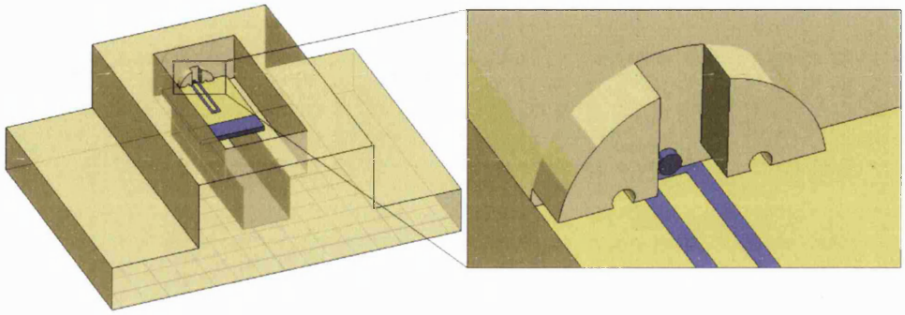

Figure 5.10 Mount design for MSMs up to 60 GHz.

5.2 Fabrication

5.2.1 Finger fabrication, proximity effect correction and dose calibration

The *Proximity effect* proved to be a major concern when fabricating the photomixers. Very fine features must be exposed with very accurately calibrated doses for a successful lift off after evaporation. The presence of other features close to them will induce an increase in the exposure of the resist. In order to address this problem, isolated fingers of a range of widths and using different recipes were exposed with graded doses as shown in Figure 5.11 (a). Once the optimum doses were known for isolated fingers of widths ranging of 0.25 μm-2 μm, collections of fingers with a range of spacings were exposed for evaluating the relative increase of exposure, see Figure 5.11 (b). As a general scaling rule, proximity effects between fingers were found to increase the exposure between 5% and 10% when the spacing is comparable with the finger width.

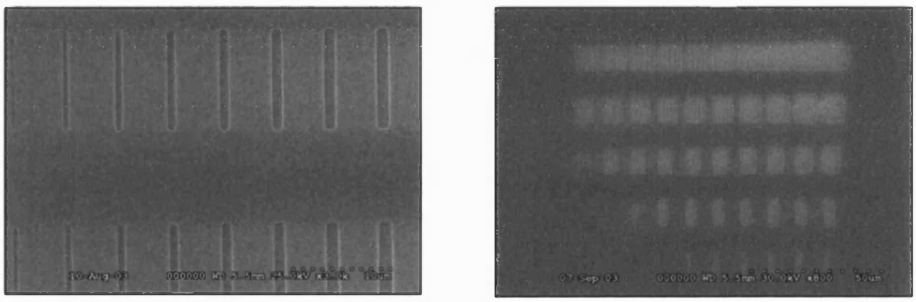

Figure 5.11 Detail of dose calibration exposures for (a) individual fingers and (b) collection of fingers on GaAs.

Proximity effects become critical when exposing the finger patterns in the vicinity of the contacting pads. Electrons undergo collisions within the electron-resist and the supporting substrate, leading to a reduction in their energy and a change in their trajectories (scattering). Thus, the electrons spread out and partially expose the areas of resist immediately adjacent to those that are intentionally exposed. Proximity effects limit the minimum separation between adjacent features and result in the need to reduce the dose in features that are close to other features.

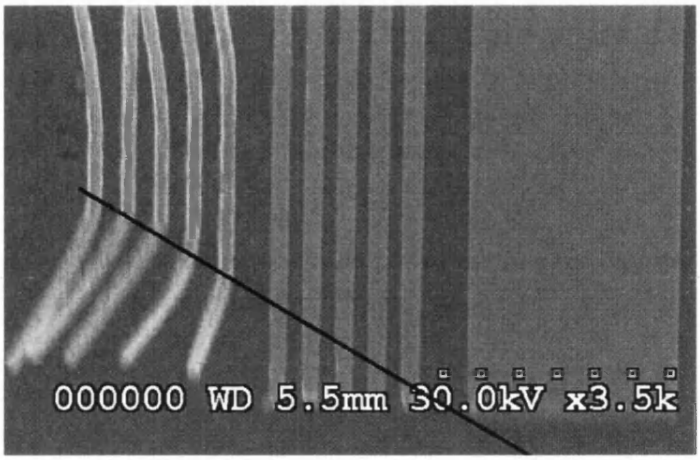

Figure 5.12 Detail of the fabricated patterns used for pad-fingers proximity effect quantification.

Figure 5.12 shows a detail of the method developed to quantify the magnitude of the proximity effects induced by exposure of the pads. The optimum dose for a particular size of finger in the absence of the pads is known as it was previously calibrated, and is referred to as D_{OPT}. Close to the contact pad there are two blocks of five fingers each, the block on the right was exposed with a slightly higher dose than the one to its left ($D_1 < D_2 < D_{OPT}$). The contact pad pattern was exposed with relatively high dose. The black line represents the loci of points that were exposed with the optimum dose (D_{OPT}). The positions in the finger patterns that did not receive a sufficiently high dose (below the black line) are not properly adhered to the sample, as the window in the PMMA after development was not totally open. Therefore the extra dose due to proximity effects (D_{PROX}) in those points can be calculated from: $D_{OPT} = D_{PROX} + D_n$.

With this method the strength of the proximity effect was evaluated for different distances from the pad and for different pad doses. This method proved extremely important for the successful fabrication of MSMs, where a collection of fingers and connecting pads in close proximity needed to be exposed.

In order to correct proximity effects two techniques were used. The first is the *dose modulation* technique. Given a pattern and certain order in which individual elements are exposed, the dose of each feature is calibrated for the exposed pattern to

correspond to the desired size. This process has the inconvenience of being very time consuming as changing the dose of one pattern affects the calibration doses of all the surrounding patterns. In combination with the *modulation dose* technique a second technique was used, it consists of the reduction of the size of the patterns to be exposed. The reduced size is compensated by applying higher dose or making use of the extra dose originated due to the proximity effect. Therefore for the fabrication of 0.25 μm wide fingers, the finger patterns exposed were 0.2 μm wide and the extra dose due to the proximity effect widens the feature to the desired size. Table 5.4 shows the required area and pattern dose for a collection of ten 0.25 μm wide fingers for a range spacings:

Width (μm)	Spacing (μm)	Optimum Area Dose (μAs/cm^2)	Dose central finger	Dose last finger
0.25	0.25	300	0.9	1.1
0.25	0.5	325	0.9	1.1
0.25	0.75	350	0.9	1.1
0.25	1	375	0.9	1.1
0.25	1.5	400	0.9	1.1

Table 5.4 Doses of for devices of active area 15 μm x 15 μm.

As seen in Chapter 3, the quantum efficiency of a transit time limited MSM with contacts recessed 0.5 μm on LTG-GaAs can be estimated to be about 30% due to collection of carriers generated deeper in the semiconductor. Furthermore, this design reduces the spreading in the travelling distance of carriers generated at different depths due to a more homogeneous electric field distribution in the active layer. Reactive dry etching was considered for recessing the electrodes, but it was not found convenient as it can mechanically damage the semiconductor affecting the quality of the Schottky contact [10]. The semi-buried contacts were realised by anisotropic wet etching. For successful fabrication using such technique, the fingers have to be aligned with the crystallographic direction [011] resulting in a v shaped profile.

The semiburied MSMs have the additional advantage of allowing the evaporation of thicker metallisations with thin layers of PMMA, therefore reducing the resistance of the fingers (R_F) of the devices.

5.2.2 Photomixers fabrication process

The first batches fabricated were monolithically integrated MSMs with CPW, the developed fabrication process is shown in Table 5.5:

Step	Process	Recipe	Comments
0	Chip Cutting	6 mm x 10 mm chip	Cutting parallel to crystallographic axis
1	SiO_2 wet etch	2 minutes in HF	
2	Spin S1813	30 s @ 3500 RPM	
3	Baking	Hot plate 115ºC for 60 s	
4	Hardening	2 min Chlorobenzene	Lift off enhancement technique
5	UV frame exposure	3 minutes exposure	Critical for optimum contact
6	Development	1min in H_2O:Microposit 351@ 3.5:1	See Figure 5.13
7	Rinse	1 min in H_2O	Critical for successful lift off
8	UV alignment marks exposure	Typically 4 s exposure	Recipe depends on calibration of lamp
9	Development	40 s in H_2O:Microposit 351 @ 3.5:1	Critical recipe calibration for successful lift off
10	Rinse	1 min in H_2O	Critical for successful lift off

Table 5.5a Fabrication Process I

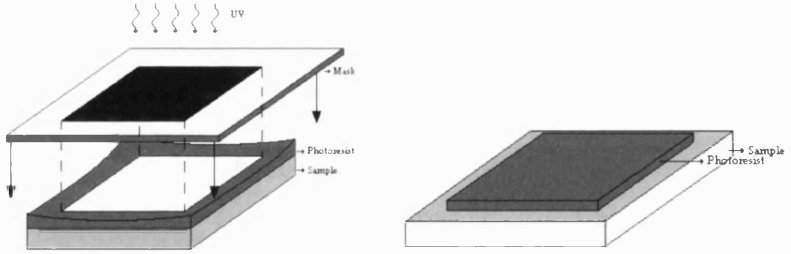

Figure 5.13 Detail of frame exposure and development (fabrication steps 5 and 6)

11	Metal Evaporation	20 nm Ti (for adhesion) + 200 nm Au	Minimum of 200 nm of metal required for optimum contrast during e-beam alignment
12	Lift off	Long immersion in acetone followed by IPA rinse	Optional soft ultrasound
13	Repetition of steps 2-7	Frame exposure and development	
14	UV exposure of CPW	Typically 4 s exposure	Using photographic film masks
15	Development	40 s in H_2O:Microposit 351 @ 3.5:1	Critical recipe calibration for successful lift off
16	GaAs oxide etch	1 min immersion in HCl	For good quality contact

17	Metal Evaporation	50 nm Ti + 500 nm Au	
18	Lift off	Long immersion in acetone followed by IPA rinse	Optional ultrasound
19	Spin and Bake double layer of PMMA	Described in detail in Chapter 4	
20	E-beam exposure of MSM		Placement using CPW metallization
21	Development	Typically 80 s in MIBK:IPA 1:3	Critical calibration of development time for successful lift off
22	GaAs oxide etch	1min immersion in HCl	For good quality of Schottky contacts
23	Metal Evaporation	20 nm Ti + 150 nm Au	
24	Lift off	Long immersion in acetone followed by IPA rinse	Ultrasound is not recommendable as it can damage delicate MSMs
25	Repetition of steps 2-7		
26	UV exposure of connection pads	Typically 4 s exposure	
27	Development	40 s in H_2O:Microposit 351 @ 3.5:1	Critical recipe callibration for successful lift off
28	Rinse	1 min in H_2O	Critical for successful lift off
29	Metal Evaporation	20 nm Ti (for adhesion) + 200 nm Au	
30	Lift off	Long immersion in acetone followed by IPA rinse	
31	Mounting	Placement of chip in place and gluing to the mount	
32	Connection	Central pin connected to central line of CPW, and side pins connected to ground planes	Epoxy or silver paint applied under the microscope using the tip of an optical fibre.

Table 5.5b Fabrication Process I

With this method MSMs with active areas ranging from 100 μm x 100 μm to 15 μm x 15 μm and finger widths and spacing ranging 1–0.2 μm were fabricated for operation at 14 GHz, 34 GHz and 50 GHz. Some of those are shown in Figure 5.14:

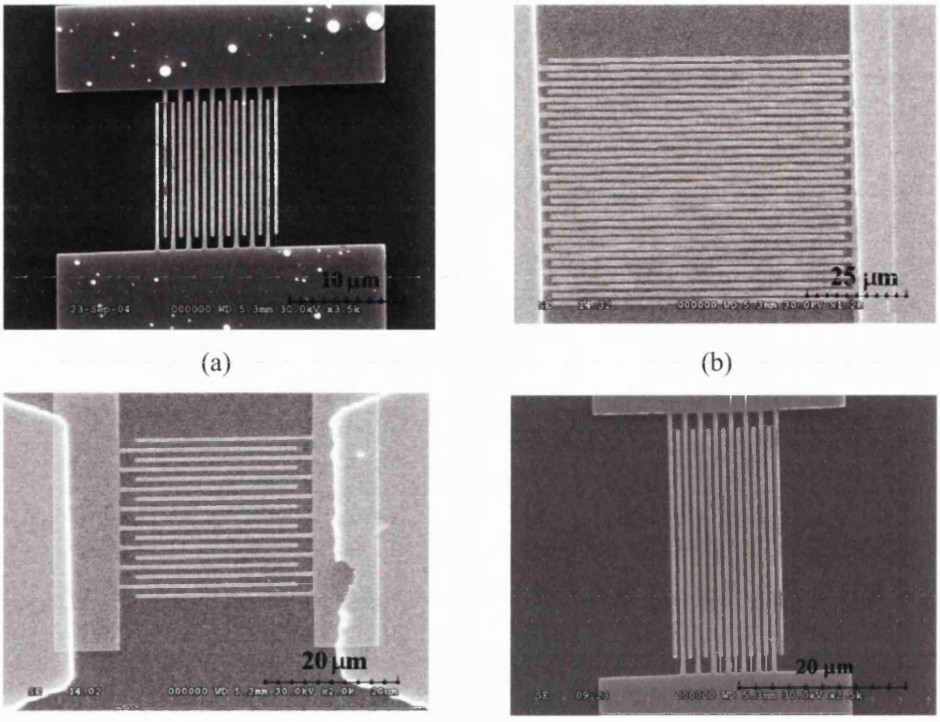

(a) (b)

(c) (d)

Figure 5.14 Photographs of some fabricated devices (a) Active area= 10 µm x 10 µm, finger width and spacing 0.3 µm (b) AA= 60 µm x 60 µm, w=1 µm and s=0.9 µm, (c) AA= 25 µm x 25 µm, w=0.5 µm and s= 1 µm, (d) AA= 13 µm x 27 µm, w=0.55 µm and s=0.45 µm.

Many batches with different combinations of widths, spacings and areas were fabricated in the course of this research. Three typical dimensions of devices for operation at different frequencies are shown in Table 5.6:

Frequency operation	WA (µm x µm)	AA (µm x µm)	s (µm)	w (µm)
14 GHz	50 x 50	40 x 40	0.5	0.5
34 GHz	50 x 50	30 x 30	0.5	0.5
50 GHz	25 x 25	15 x 15	0.25	0.25

Table 5.6 Table for devices operation at 14 GHz, 34 GHz and 50 GHz, where s and w are respectively the width and spacing of the fingers.

The main disadvantage of this fabrication method is the low yield, as any damage in the device or transmission lines during fabrication or testing, left 6 mm x 10 mm of

GaAs unusable. Another disadvantage encountered in the beginning of the research is that as the CPWs were fabricated using a photographic negative and then used as global alignment marks, the placement of the devices was not very accurate.

In order to improve the yield, an alternative fabrication method (Fabrication Method II) for monolithically integrated MSMs was developed, see Table 5.7. Figure 5.15 shows the patterns included in the photolithographic mask, note that the MSMs in yellow are included only for clarity.

Step	Process	Layer
1	Chip cutting and SiO_2 wet etch	
2	Spin, bake and hardening S1813	
3	UV frame exposure and development	Layer 0, White
4	UV exposure of global (in the corners) and local (in the inset) alignment marks development, and metal evaporation	Layer 1, Red
5	Ebeam exposure of five MSMs devices, development, GaAs oxide etch, metal evaporation and lift off	Layer 2, Yellow
6	Inspection of devices and selection of the one in best condition (in the figure the central one)	
7	Repetition of steps 2 and 3	
8	Exposure of CPW using the global alignment marks for placing it in the correct position with respect to the selected device	Layer 3, Purple
9	Exposure of contacting pads , development, GaAs oxide etch, metal evaporation and lift off.	Layer 4, Pink
10	Mounting and Connection	

Table 5.7 Fabrication process II

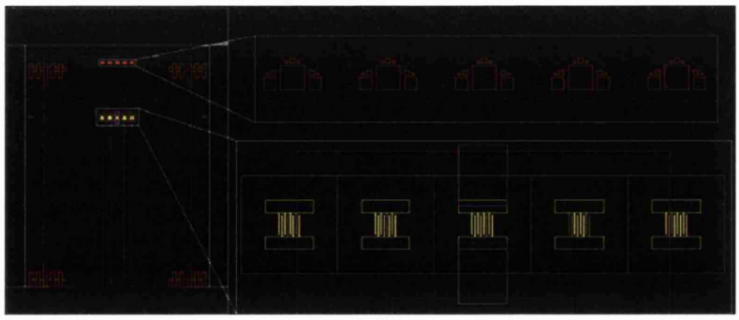

Figure 5.15 Photolithographic mask used in Fabrication Process II

The main novel feature of this method is the possibility of selection of the MSM in best condition after lift-off, therefore reducing the chances of failure of the fabrication process. This method sensibly improved the yield by avoiding waste of material due to deficient MSMs.

A third fabrication method for non-monolithic prototypes was developed for further improving the yield. This consisted in the fabrication of CPW chip, using the first 4 steps of Table 5.7. Subsequently, a groove was fabricated via photolithography and wet etch on the CPW chip where the MSM is to be placed. The result after this step is shown in Figure 5.16 (a). The individual MSM chips fabricated using the process described in Table 7.8, were placed in position and glued to the CPW chip, Figure 5.16 (b):

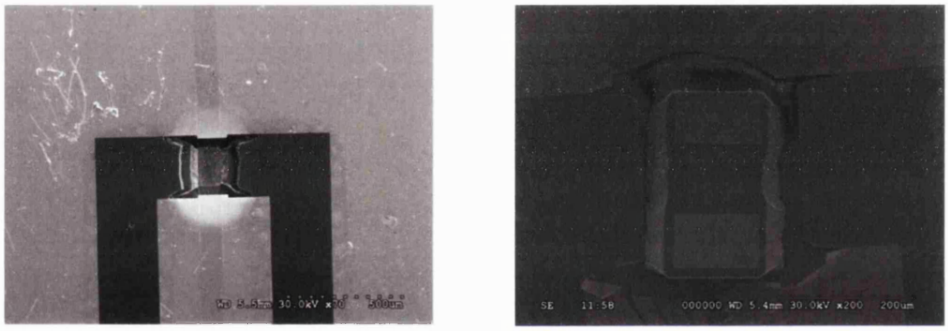

Figure 5.16 Non monolithical prototypes resulting from Fabrication Process III a) CPW with etched groove b) Individual MSM chip glued in place

This process was developed for the characterisation of individual MSM chips. The advantages of this design are the possibility of interchanging the device if damaged after operation and the ease of connection as the MSM sits in the groove. The main disadvantage is the necessity of connecting the pads to the transmission line, therefore introducing an extra inductance that reduces the frequency response of the prototypes.

5.2.3 Mounting

Once the chips were successfully fabricated, they were fixed on the housing with cyanoacrylate and the central and ground pins were connected to the CPW using conducting epoxy or silver paint as shown in Figure 5.17:

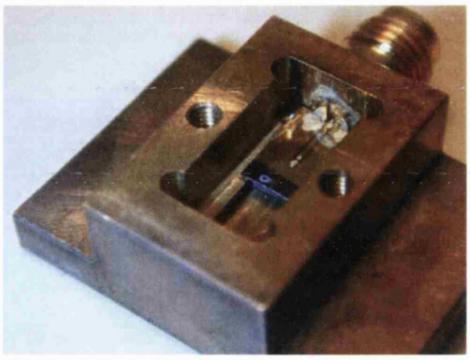

Figure 5.17 Mounted device

5.3 Test and Results

The first tests to be carried out for validating the modelling of the devices were the measurement of the resistance of the fingers. The resistance was measured using a Keithley programmable electrometer and a Keithley programmable current source. In order to make accurate measurements, the fingers were evaporated over an insulator material (SiO_2 and silica) for avoiding leaking of current from pad to pad through the semiconductor. This fact led the electron beam to charge up the chip during exposure and therefore affected the resolution. Given that the minimum achieved width of finger in silica was 1 μm, the study was restricted to the dependence of resistance per unit length with respect to the thickness of the fingers. The results are shown in Figure 5.17:

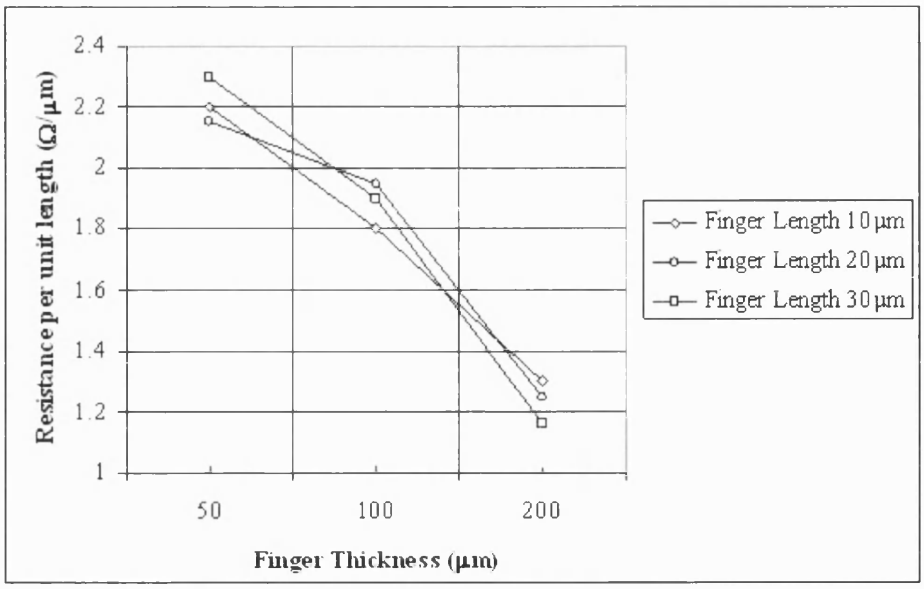

Figure 5.17 Finger resistance vs. finger thickness on SiO_2 for 1 μm wide fingers.

The same measurement of resistance dependency with thickness on GaAs did not show a significant deviation from that on silica for 1 μm wide fingers. This was attributed to the high resistance through the undoped semiconductor. In light of this, tests for calculating the dependency of the resistance with respect to finger width were carried out for fingers 200 nm thick on LTG GaAs, the results are shown in Figure 5.18:

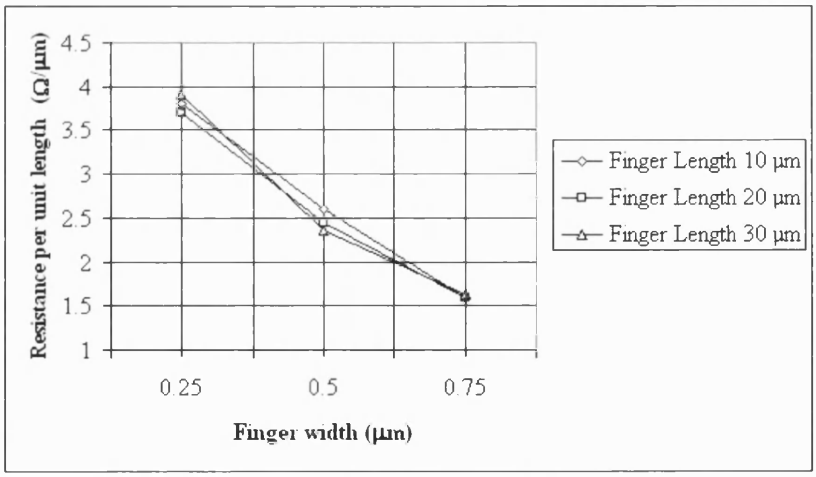

Figure 5.18 Finger resistance vs. finger widths,
for fingers 200 μm thick on LTG GaAs.

The resistance correction coefficients obtained from the data presented in Figure 5.17 and Figure 5.18 were the values used in the calculation of the R_F in the equivalent circuit modelling (Section 5.1).

For the capacitance characterisation, large arrays of devices with a combination of sizes were fabricated on the same chip for ensuring the accuracy of the obtained values. The measurements of the capacitance of the devices and were carried out using HP 4279A 1MHz C-V meter. Some of the obtained results obtained are shown in Table 5.10:

Aperture (μm)	Spacing (μm)	Width (μm)	Estimated Capacitance for Planar MSM (fF)	Experimental Capacitance Planar MSM (fF)	Experimental Capa. buried MSM (fF)
75	1	1	177.4	181	183
75	2	1	90.0	92	91
75	3	1	59.6	61	62
75	4	1	44.5	47	46
20	0.5	0.5	25.2	30	31
20	0.5	1	22.2	27	27
20	0.5	1.5	19.0	20	21
20	0.5	2	16.5	17	18
12	0.25	0.25	18.2	24	
12	0.5	0.25	9.2	17	
12	0.75	0.25	6.1	13	

Table 5.10 Measured capacitance and theoretical capacitances.

As it can be seen in Table 5.10 the measured values are in good agreement with the measured ones. The small deviation is more pronounced the smaller the aperture of the devices. This probably is due to the fact that the theoretical predicted value corresponds only to the capacitance of the fingers (C_F), whereas the measured capacitance includes the capacitance from pad to pad (C_{PP}) and from pad to ground (C_{PG}). Obviously, the smaller the aperture of the device, the closer the pads are, incurring a higher value of C_{PP}. Measurements of the capacitance between pads separated by distances ranging 8 μm and 80 μm yielded values of C_{PP} between 7 fF and 3 fF.

The buried devices with very fine finger widths proved to be difficult to fabricate. For widths larger than 0.25 μm the measurement of the capacitance yielded very similar results to the values obtained for conventional MSM as seen in Table 5.10.

The measurements of the capacitance were completed with C-V measurements of the devices. An example of the obtained results are shown in Figure 5.17, corresponding to a 20 μm x 20 μm device with finger width and spacing 0.5 μm.

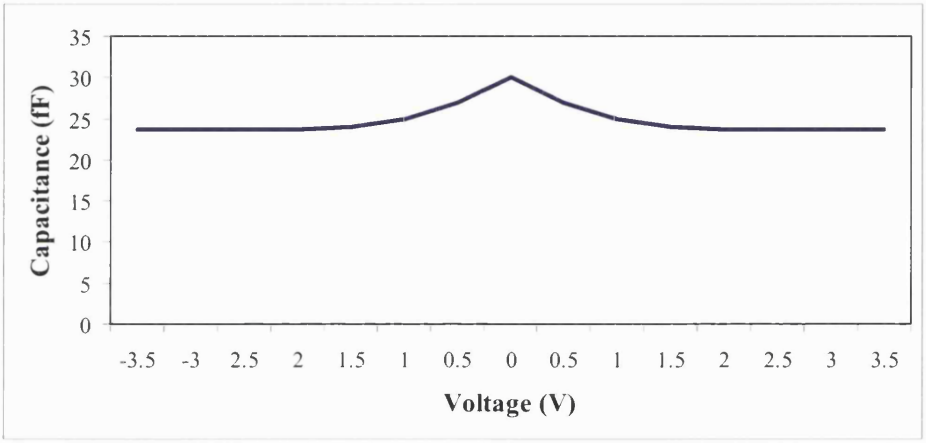

Figure 5.17 Measured C-V characteristics of an MSM on LTG-GaAs.

The figure shows how the value of the capacitance is reduced roughly a 25% when the semiconductor completely depleted. This reduction of the capacitance between finger (C_F) was introduced in the equivalent circuit model.

For the dc measurements, the housing was connected to a power supply and a current meter, and the devices were illuminated by a 12 mW HeNe laser (632.8 nm) coupled in a single mode optical fibre (ESM-12) as shown in Figure 5.18. The numerical aperture (NA) is 0.05 and the core size is 12 μm with a mode field diameter (MFD) of 6.4 μm at 1550 nm. The estimation of the size of the beam on the device can be easily obtained by using the NA of the fiber and the distance from the tip to the fiber to the sample by using the Gaussian beam divergence equations. At 1 mm distance, the radius of the waist of the beam was estimated to be approximately 50 μm.

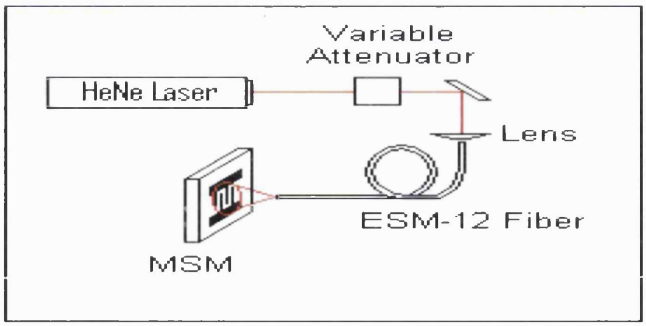

Figure 5.18 DC measurement schematic setup.

Two x-y-z stages were used for maximum coupling of the light into the fibre (using a 20x lense) and for optimum illumination of the device, such setup is shown in Figure 5.19. The maximum power measured at the output of the fibre was 4 mW, well below the high power breakdown limit found in literature.

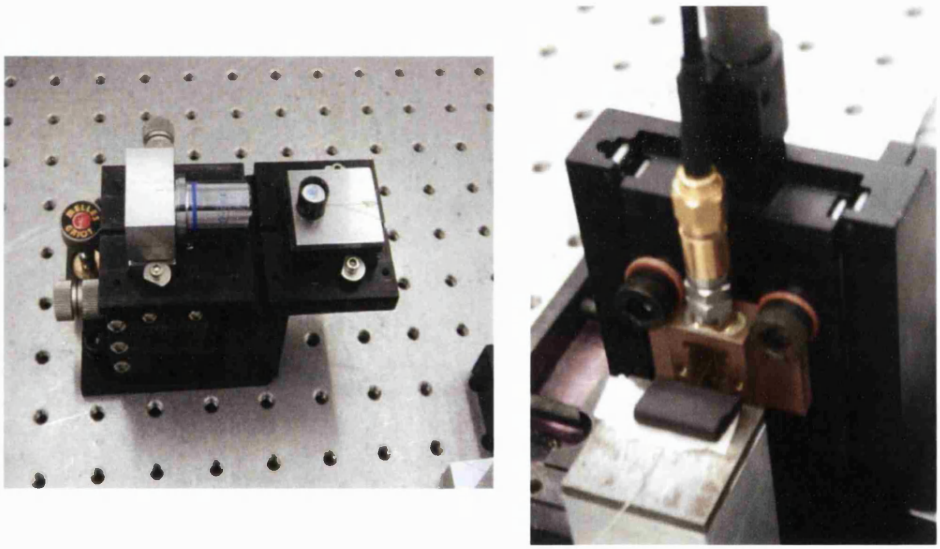

Figure 5.19 Fibre optic, lense and microstage setup for DC measurements.

The devices were tested under non illumination conditions for measuring the dark current of the devices for different values of bias. The initial measured values of the dark current were observed to increase (up to 20%) after a few minutes of use, stabilising afterwards. In general the values of the dark current were found to be of the order of tens of nanoamperes.

The estimation of the size of the spot for calculating the responsivity is not extremely accurate, as the shape of the beam is dependent on the quality of the cleaving of the fibre and on the distance from the fibre to the device (that it can not be accurately measured). Nonetheless the values of the responsivity shown in Figure were made assuming that beam size spot is 100 μm in diameter and that the centre of the device is aligned with the axis of the beam. The portion of the total optical power (4 mW) that was incident in the active area of the detector was calculated by integration of the Gaussian distribution.

DC tests result for devices with finger width 0.25 μm and active area 15 μm x 15 μm and 20 μm x 20 μm are shown in Figure 5.20:

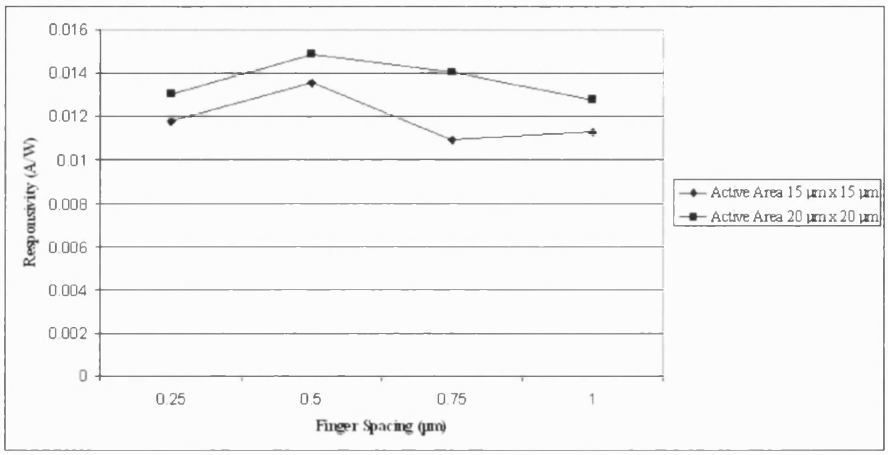

Figure 5.20 Responsivity vs. finger spacing for MSMs with finger width 0.25 μm and active areas 15 μm x 15 μm and 20 μm x 20μm.

It can be observed how larger values of spacing do not yield higher values of the quantum efficiency as it would be expected attending only to the shadowing effect. This was attributed to the fact that for large spacings the average transit time becomes greater than the average recombination time.

DC tests result for devices with finger width 0.5 μm and active area 30 μm x 30 μm and 40 μm x 40 μm are shown in Figure 5.21:

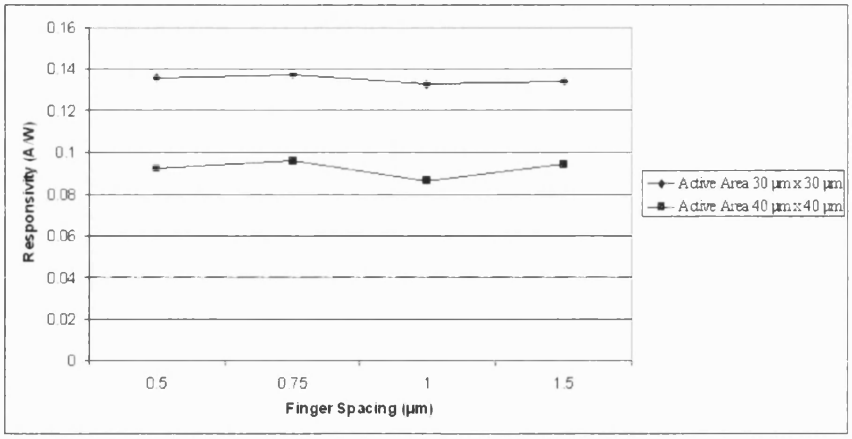

Figure 5.21 Responsivity vs. finger spacing for MSMs with finger width 0.5 µm and active areas 30 µm x 30 µm and 40 µm x 40 µm.

Note that MSM devices have a maximum operating bias voltage, that corresponds to the point where the photocurrent begins to oscillate due to carriers tunnelling through the barrier. The values for the maximum operating bias voltage is of the order of tens of µA, and is obviously strongly dependent on the finger spacing. DC tests result for devices with finger width 1 µm and active area 60 µm x 60 µm and 80 µm x 80 µm are shown in Figure 5.22:

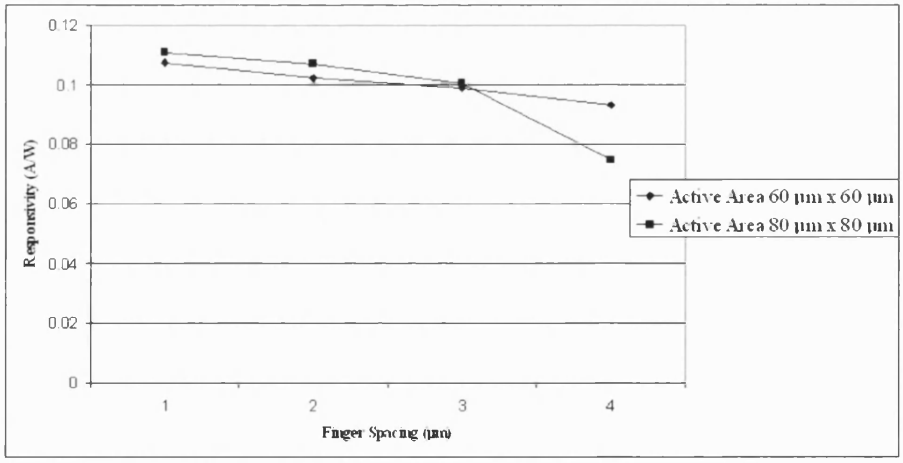

Figure 5.22 Responsivity vs. finger spacing for MSMs with finger width 1 µm and active areas 60 µm x 60 µm and 80 µm x 80 µm.

A setup similar to that used for dc tests was arranged for the characterisation of the time response of the devices. In such setup the prototype was connected to a 50 GHz oscilloscope and the device was illuminated with a fs pulsed Ti:Sapphire laser. The experiment did not yield any results

DC test were performed for various batches of devices with buried contacts. In Figure 5.23 results obtained for devices with fingers 0.5 μm wide, 0.5 μm deep and active area 30 μm x 30 μm and 40 μm x 40 μm are shown:

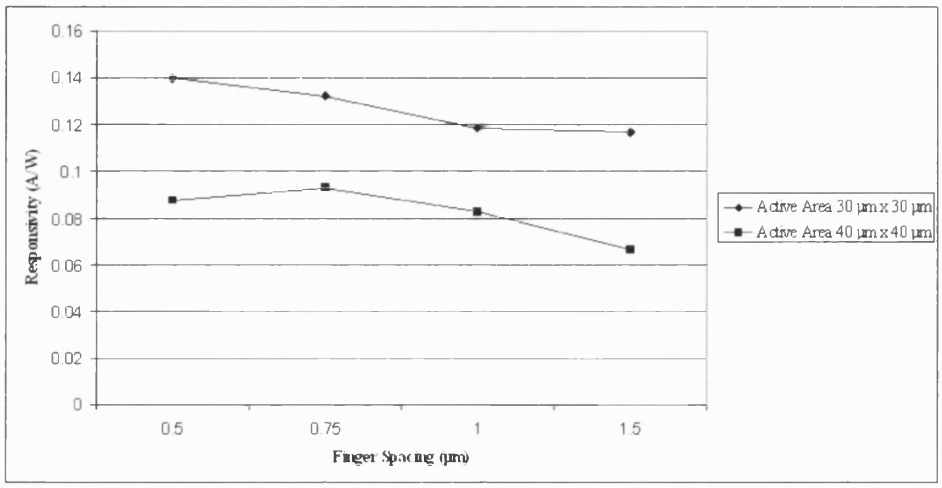

Figure 5.23 Responsivity vs. finger spacing for 0.5 μm buried MSMs with finger width 0.5 μm and active areas 30 μm x 30 μm and 40 μm x 40 μm.

The inaccuracy in the determination of the size of the beam on the device makes difficult to make an estimation of the improvement of the quantum efficiency when using buried contacts. The obtained values of the maximum bias voltage obtained for the buried device are lower than the equivalent normal device. This was attributed to the fact that for the same applied voltage, the corresponding electric field in the semiconductor is stronger when using devices with recessed electrodes.

As seen in Chapter 2, photodiodes have a linear dependency of the photocurrent with the optical power. Six optical attenuators were used in the setup shown in Figure 5.24 for this measurement. All the tested devices passed satisfactorily the test, the typical obtained results being shown in Figure 5.20:

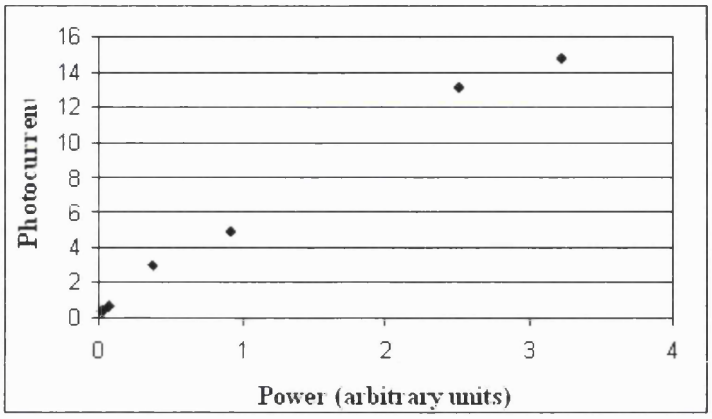

Figure 5.24 Photocurrent vs. incident optical power.

Some of the devices were re-tested months after they were originally tested, no degradation in their performance was observed. .

An MSM photomixer was used to measure a 33 GHz coherent Raman detected ESR spectrum of a dilute Ruby sample. The monolithical device had an active area of 20 μm x 20 μm and finger width and spacing of 0.5 μm. It was operated at a bias voltage of 8 V, driven by a laser tuned to 596.5 nm with a power of 650 μW. The resulting spectrum is shown in Figure 5.19, demonstrating successful operation of the prototype.

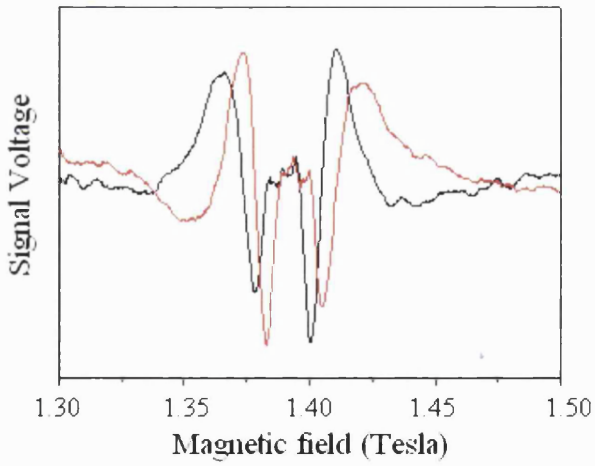

Figure 5.21 A 33 GHz coherent Raman detected ESR spectrum of a dilute Ruby sample measured with one of the fabricated prototypes.

The spectrum obtained with our prototype is identical to that obtained with a commercial InGaAs photomixer, with the exception that our device showed a responsivity five times smaller in the CR ESR setup. The spectrum obtained is not as clear as that shown in Figure 2.19, this is attributed to the misalignment of the sample with respect to the applied magnetic field. In that case, the signals of the absorption and dispersion are not well separated into both output channels [10]. Furthermore, the presence of other transitions in the sample other than the one under study can complicate greatelly the interpretation of the data.

An useful calculation is the estimation of the generated millimetre power level by making use of Eq.(2.49). Assuming that the power RF (P_1) signal is a hundred times smaller than the power from the local oscillator (P_0), those values can be calculated considering that the total incident power incident was 650 μW. The effective load resistance (R_{eff}) is 20 ohms, and the responsivity of our device is assumed to be 0.1 A/W (according the previously obtained results). With such values the signal power from the photodetector is 1.6×10^{-9} W. This value must be compared with the noise level of the mm-wave detection system in the CR ESR. As it was previously described in Chapter 2, the power noise in the detection system is dominated by the noise of the amplifier that follows the photomixer. The noise power can be calculated from Eq.(2.50). Assuming a bandwidth of 33 GHz, and that the amplifier noise figure is 3 dB, the $P_{AMP\ NOISE}$ is 1.3×19^{-10} W.

References:

[1] Private communication with Dr. S.Bingham

[2] P.Kordos, A.Forster, M. Marso, "550 GHz bandwidth photodetector on low-temperature grown molecular-beam epitaxial GaAs", Electronics letters, 34(1):119-120, 1998

[3] Ansoft Corporation, Serenade v.8.7, Harmonica circuit simulation

[4] W.C. Koscelniak, M.A. Littlejohn and J.L.Pelouard, " Analysis of a GaAs MSM Potodetector with 0.1 μm finger spacing", IEEE Electron device letters, 10(5):209-211, 1989

[5] S. Verghese, K. A. McIntosh, E. R. Brown, "Highly tunable fiber-coupled photomixers with coherent terahertz output power", IEEE Transactions on microwave theory and techniques, 45 (8): 1301-1309, Part 2, AUG 1997

[6] AWR, TXline 2003

[7] Ansoft Corporation, High Frequency Structure Simulation v9.0

[8] Private communication with Dr. S.R. Davies

[9] Private communication with J.M. Rollin

[10] Private communication with Prof. J. J. Davies

Chapter 6

Monolithic photomixers

This chapter covers the design, modelling and fabrication process developed for monolithically integrated prototypes for operation at 100 GHz and 200 GHz.

6.1 High frequency housing

For operation at frequencies higher than 90 GHz coplanar waveguides become lossier and conventional cables do not support them. Therefore the use of hollow waveguides for the transmission of the high frequency signals is necessary. An existing mount design for astrophysics applications consisting of a mixer block with two crossing waveguides was found to be adequate for the 100 GHz prototypes. Figure 6.1 shows the schematic configuration of the prototype using the existing mount:

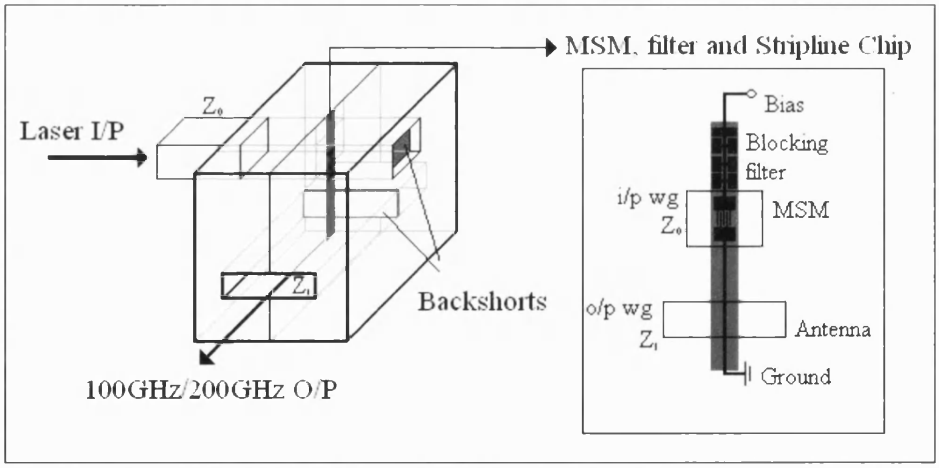

Figure 6.1 Schematic configuration of high speed prototypes.

The design of the 100 GHz monolithic prototypes using this housing consisted of a LTG-GaAs chip sitting in a groove and connected to SMA connectors for biasing. The MSM is suspended perpendicularly to the input WR-5 waveguide for illumination, with a low pass filter at one side and a microstrip leading to the WR-10

output waveguide. The low pass filter at one side of the device is to avoid the high frequency signal leaking up the SMA connector, forcing the signal to travel along the microstrip. The housing has a movable back short in the output waveguide to maximise the power coupling to the microstrip-waveguide transition (essentially an antenna).

For the 200 GHz prototypes the housing would be an analogous design but with the WR-10 being used for illumination and the WR-5 being the output. The only difference in the configuration is the relative position of the groove with respect to the waveguides for allowing illumination through the input waveguide.

Although output signal at 100 GHz could be measured directly with a diode detector, a better solution is to down convert the signal using a conventional waveguide diode mixer. The simplest arrangement is to use a harmonic mixer, pumped at an LO frequency in the 5-15 GHz range. A high order harmonic of the LO mixes with the signal to produce an IF output in the 1-4 GHz range, which can be observed using a spectrum analyser. A typical harmonic mixer used in this way can detect signals as low as around -60 dBm (1 nW). Such high sensitivity was estimated to be sufficient to detect the output signals from the MSMs.

6.2 Monolithic design and modeling

As seen in the previous chapter the advantage of using monolithically integrated prototypes is the fact that they avoid the parasitic inductance introduced by the soldering. The equivalent circuit model was run to assess the dimensions of the devices with the required bandwidth, the predicted bandwidth given in Table 6.1:

$(AA)^{1/2}$ (μm)	Width (μm)	Spacing (μm)	C_F (fF)	3dB BW (GHz)
5	0.25	0.25	3.2	660 GHz
10	0.25	0.25	12.6	310 GHz
10	0.25	0.5	6.4	480 GHz
10	0.25	0.75	4.2	590 GHz
10	0.25	1	3.2	660 GHz

Table 6.1 Predicted 3 dB bandwidth for some monolithical devices.

As mentioned in Section 5.1, the equivalent circuit model is not valid for such high frequencies. Nevertheless, previous research in LTG GaAs (see section 3.2.1, Figure 3.6) suggest that the intrinsic response times of devices with such sizes ensure performances at 100 GHz and 200 GHz.

The modelling of the chip structure was broken down into independent two port models and simulated in HFSS:

- Transmission line
- Low pass Filters
- Microstrip-waveguide transition.

The results obtained for different sizes of grounded microstrip on different thickness of semiconductor are shown in Table 6.2:

GaAs Thickness (μm)	Microstrip Width (μm)	Impedance (Ω)	Loss (dB/mm)	Effective Dielectric constant
20	50	25.5	0.65	9.6
20	100	15.5	0.56	10.5
20	150	11.2	0.54	11.1
50	50	43.5	0.36	8.96
50	100	29.6	0.28	9.75
50	150	22.7	0.26	10.3
120	50	66	0.23	9
120	100	50.2	0.17	9.6
120	150	41.2	0.14	10

Table 6.2 Parameters for grounded microstrips in GaAs at 100 GHz.

The *stepped-impedance* low pass filter blocks the high frequency signal by alternating very-high and very-low characteristic impedances lines. Lumped element modelling was performed using Serenade, alternating capacitive sections with inductive sections. The transmission line modeled is shown in Figure 6.2:

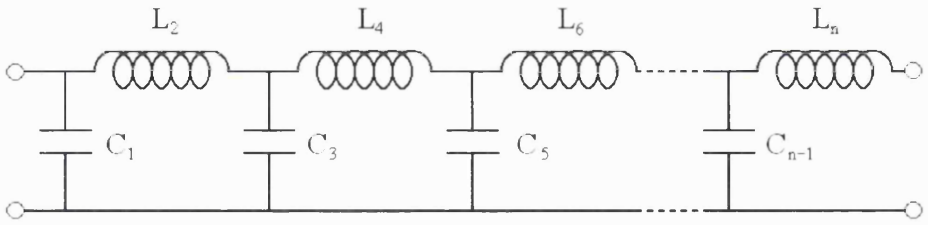

Figure 6.2 Equivalent circuit model of the stepped impedance low pass filter.

Note that the higher the number of elements (n) the sharper the filtering action. In order to validate the modelling, the results obtained by the equivalent circuit were correlated with the distributed element modelling of the stepped impedances filters. 5-element filters were found to give the required performance at 100 GHz (see Figure 6.3):

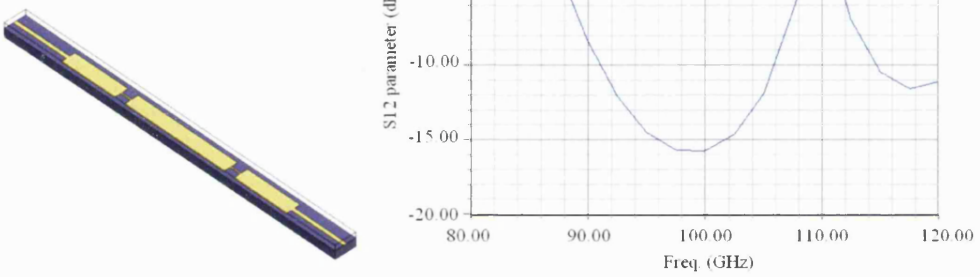

Figure 6.3 a) Diagram of a 100 GHz blocking filter on 120 μm thick LTG GaAs chip.
b) S12 parameters obtained by HFSS modelling.

Due to the configuration of the existing housing, the microstrip-waveguide transition was modelled as shown in Figure 6.4. Different sizes of transmission line were studied, a 50 μm microstrip yielding the best power coupling into the ¼ height WR-10 waveguide. The electric field is shown for the optimum backshort position (Figure 6.4 a) and the S parameters are shown (Figure 6.4 b) for a sweep in frequencies.

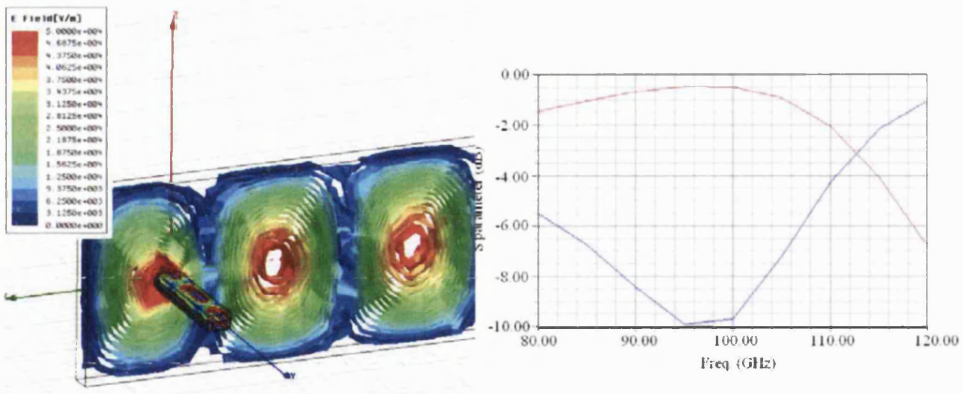

Figure 6.4 Microstrip-waveguide transition a) Electric field for optimum backshort position b) S_{12} (red) and S_{11}(blue) parameters obtained by HFSS modelling.

For the 200 GHz, a 9-element step impedance filter was found suited. In the existing mount there is not enough length of the groove to accommodate it. Therefore another mount would be required for realising these prototypes having a longer channel.

For the modelling of the 200 GHz microstrip-waveguide transition, the mounting was assumed to be identical but the groove where the chip sits was perpendicular to the position in the existing housing for allowing illumination through the 100 GHz waveguide.

6.3 Fabrication process

The fabrication process developed for monolithic prototypes include a system for the selection of the most suitable MSMs fabricated to improve the yield. The mask designed is shown in Figure 6.5:

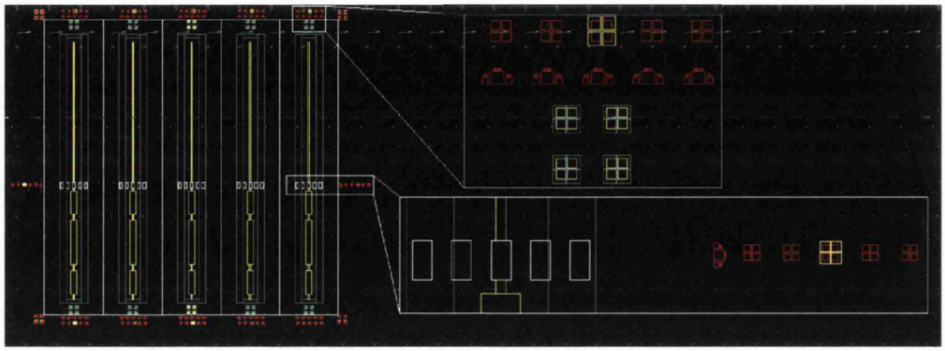

Figure 6.5 Photolithography mask design for monolithically integrated 100 GHz prototypes

The fabrication process for these devices is shown in Table 6.3:

Step	Process	Layer
1	Chip cutting (15 mm x 15 mm) and SiO_2 wet etch	
2	Spin, bake and hardening S1813	
3	UV frame exposure and development	Layer 0, White
4	UV Exposure of alignment marks, development, evaporation and lift off	Layer 1,red
5	Ebeam exposure of 25 devices, development and evaporation	
6	Repeat steps 2 and 3	
7	UV exposure of filters and antennas, selecting the MSM in best condition, note that the filters must be exposed one by one covering the rest of the mask in each step, development and evaporation	Layer 2, yellow
8	Repeat steps 2 and 3	
9	UV exposure of separation grid aligned with respect to the marks. They must be exposed one by one as done with filters	Layer 3, Green
10	Wet etch of separation grid	
11	Back mounting on Si chip with high temperature wax	
12	Mount in a glass plate with low temperature wax	
13	Mechanical lapping	
14	Acetone and IPA for chip separation	

Table 6.3 Fabrication process for monolithically integrated prototypes

Note that the mask was designed for the filters to be aligned with the crystallographic orientation [011], as the grid in the photolithographic mask for chip separation is thinner in the direction in which the wet etch profile undercuts the semiconductor.

Processing tests showed the potentially problematic fabrication of thin and long GaAs chips as they tend to bend after mechanical lapping. Furthermore, this design requires a large amount of GaAs and this fact together with the need for fabricating another mount made the prototypes difficult to develop within the budget and time constraints of the project. Overcoming such problems was the main motivation for the choice of the non-monolithical prototypes described in next chapter.

Chapter 7

Non-Monolithic prototypes

This chapter covers the design, modelling, fabrication and testing of the non-monolithic prototypes for operation at 100 GHz and 200 GHz carried out in the David Bullett Nanofabrication Laboratory and the Terahertz Technology Laboratory at the University of Bath.

7.1 Modelling and Design

Non-monolithical prototypes operate in an equivalent manner to the monolithic prototypes. The design consists of an MSM, a blocking filter, a microstrip and the two crossing waveguides. Individual GaAs MSM chips are mounted on a quartz substrate that is suspended in the cavity and connected with the transmission line. The main advantages of this design are the lower losses due to the lower dielectric constant and the quartz chip being more robust than on GaAs chips. Nevertheless the need for soldering between the photomixer and the microstrip adds inductance (L_{MOUNT}). Table 7.1 shows the bandwidth limitation predicted by equivalent circuit modelling:

$(AA)^{1/2}$ (μm)	Width (μm)	Spacing (μm)	C_F (fF)	Mounted (0.1pH) 3dB BW	Mounted(0.2 pH) 3dB BW
5	0.25	0.25	3.2	170 GHz	82.5 GHz
5	0.25	0.5	1.4	170 GHz	82.5 GHz
5	0.25	0.75	0.9	170 GHz	82.5 GHz
5	0.25	1	0.7	170 GHz	82.5 GHz
10	0.25	0.25	12.6	147 GHz	82.5 GHz
10	0.25	0.5	6.4	160 GHz	82.5 GHz
10	0.25	0.75	4.2	165 GHz	82.5 GHz
10	0.25	1	3.2	170 GHz	82.5 GHz

Table 7.1 RC limited bandwidths modeled by equivalent circuit model showing the limitation of the inductance of the connection.

In order to ensure the operation of the prototypes at high frequencies, the soldering must be done with the minimum amount of silver paint possible to keep the inductance under 100 fH. In spite of the limitation shown by the modelling, this

connecting technique has been successfully used in the past by THz Research Group for the connection of microwave mixers operating at frequencies as high as 300 GHz. Nevertheless an alternative low inductance soldering method was envisaged and it is described in Section 7.2.3.

The modelling of the 100 GHz and 200 GHz non-monolithic prototypes was performed in a similar fashion to the monolithic prototypes, assessing independently the performance of the suspended microstrip, filters and microstrip-waveguide transition.

7.1.1 100 GHz prototypes

The modelled characteristics of suspended microstrips (90 μm over the ground plane and metallizations 0.2 μm thick) onto 40 μm thick quartz substrates of different widths obtained with the suspended microstrip calculator [1] for 100 GHz are shown in Table 7.2. These results were validated by HFSS modelling of the suspended lines.

Quartz Thickness (μm)	Width (μm)	Impedance (Ω)	Eff. Dielectric constant
40	50	142	1.64
40	100	113.7	1.55
40	200	84	1.46
70	50	140.4	1.93
70	100	114.3	1.8
70	200	87.4	1.7

Table 7.2 Parameters of suspended microstrips on quartz substrate at 100 GHz.

The microstrip-waveguide transition characteristics were modelled for the quartz prototype in HFSS for microstrips ranging 50 μm – 200 μm in width. The relative position of the microstrip with respect to the output waveguide is shown in Figure 7.1:

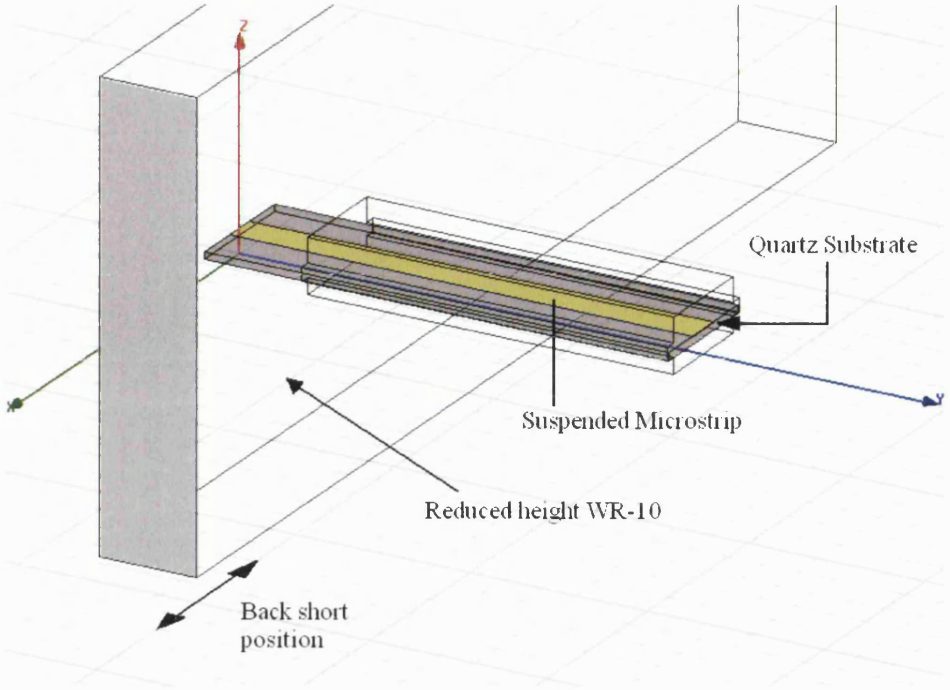

Figure 7.1 Schematic of the modelled microstrip-waveguide transition.

The sweep of the back short position for evaluating the maximum power transmission to the output waveguide was modelled for different microstrip sizes and various quartz thicknesses. The obtained S_{12} parameters for a 100 μm microstrip over a 40 μm quartz substrate are shown in Figure 7.2:

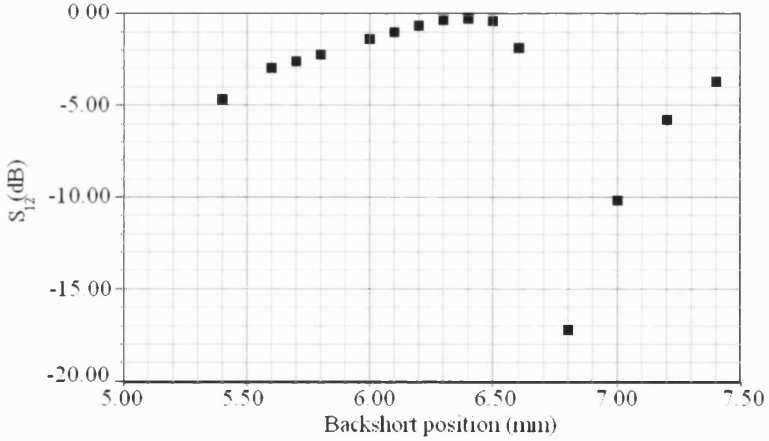

Figure 7.2 S_{12} parameters versus back short position at 100 GHz for the microstrip-waveguide transition.

The maximum power transmission occurs at a back short position 6.4 mm; for this value the bandwidth obtained is shown in Figure 7.3:

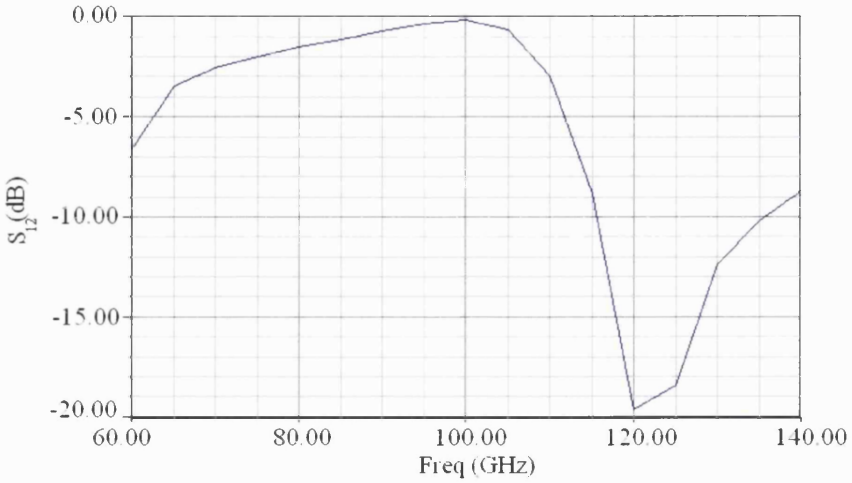

Figure 7.3 S_{12} for the microstrip-waveguide transition
for the optimum back short position.

The results shown in Figure 7.3 suggest that the designed prototypes have less than 3 dB attenuation between 70 GHz and 110 GHz.

For the design of the filters, an existing hammerhead filter [2] on 70 μm thick quartz was modelled in order to correlate the distributed element model with the actual performance. The schematic of a generic hammerhead filter is shown in Figure 7.4; the dimensions of the existing filter are shown in Table 7.3:

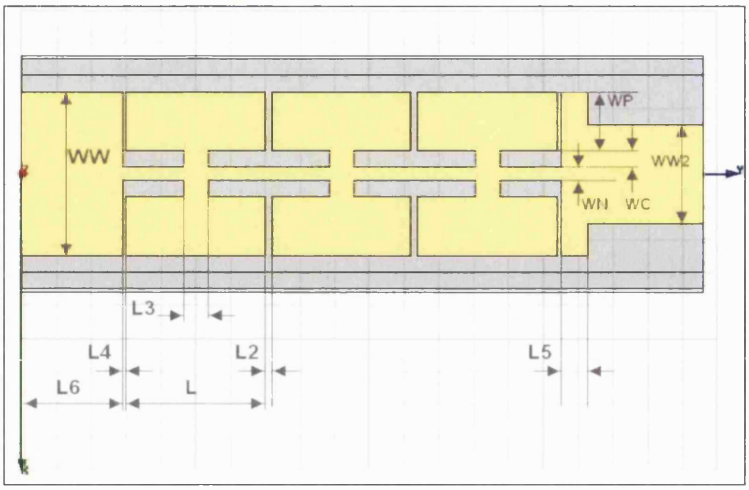

Figure 7.4 Schematic of a 3-element hammerhead filter.

L=330	L2=20	L3=70	L4=10	L5=75	L6=290
WW=500	WW2=300	WN=40	WC=50	WP=180	

Table 7.3 Dimensions of the existing filter expressed in μm.

The hammerhead filter with dimensions shown in Table 7.3 was modelled in HFSS, yielding the S_{12} parameters shown in Figure 7.5. The known performance of the filter agreed very well with the obtained results of the modelling, suggesting that the modelling technique was well suited for the design of new filters.

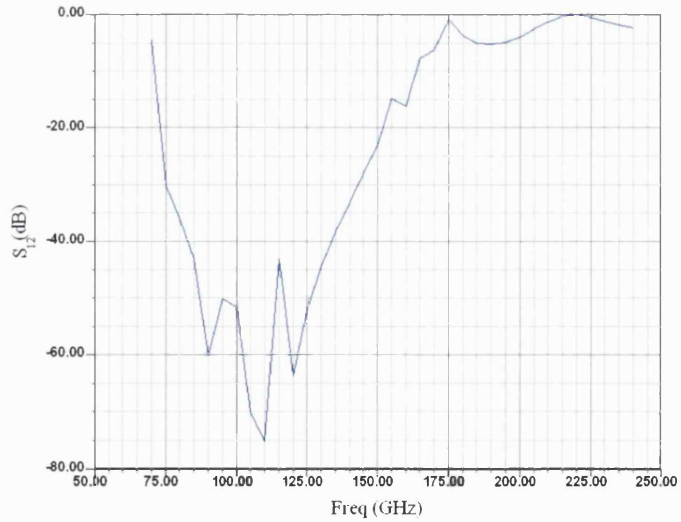

Figure 7.5 S_{12} parameters result for the existing filter onto a 70 μm quartz substrate.

The same existing filter was modelled for a 40 μm thick quartz substrate for evaluating the influence of the thickness of the quartz in the filter performance. The S_{12} parameters obtained by modelling are shown in Figure 7.6:

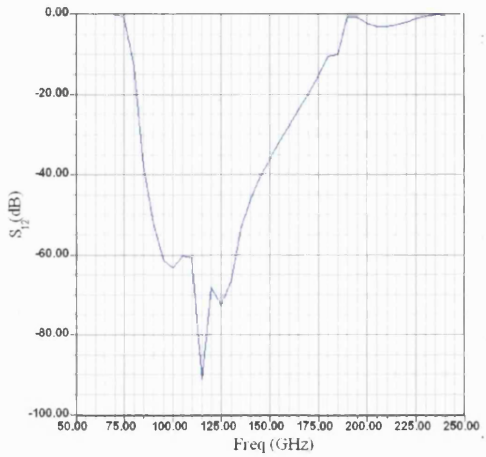

Figure 7.6 S_{12} parameters result for the existing filter onto a 40 μm quartz substrate.

A sweep of the different dimensions of the filter was done in order to optimise the performance for our particular application. S_{12} parameters for a sweep of L are shown in Figure 7.7; the S_{12} parameters obtained for L=400 μm are shown in Figure 7.8:

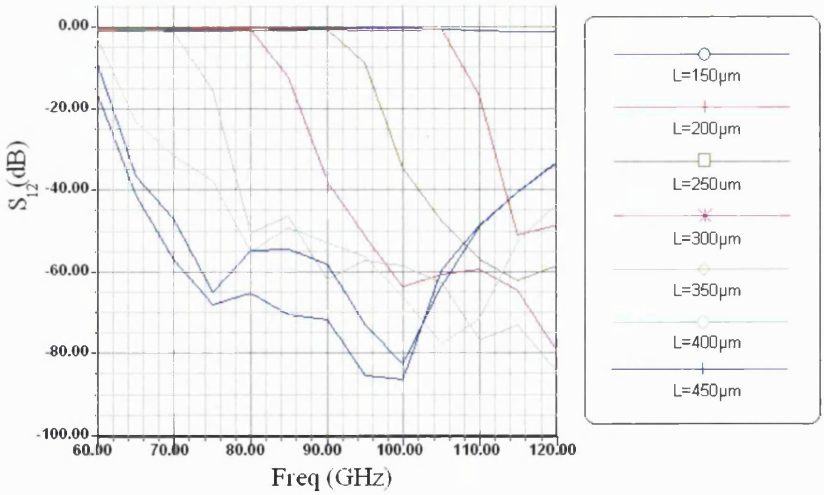

Figure 7.7 S_{12} Parameters of the hammerhead filter for a sweep of the L dimension.

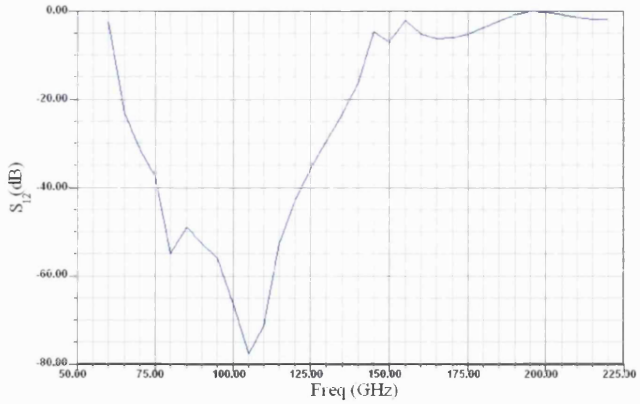

Figure 7.8 S_{12} parameters of the hammerhead filter for L=400 μm.

Modelling showed little dependence of the performance of a filter on L3. The final dimensions of the low pass filter for 40 μm quartz substrate blocking 100 GHz are shown in Table 7.4:

L=400	L2=20	L3=70	L4=10	L5=75	L6=290
WW=500	WW2=300	WN=40	WC=50	WP=180	

Table 7.4 Dimensions for 100 GHz block hammerhead filter

(all dimensions expressed in μm).

7.1.2 200 GHz prototypes

The parameters for suspended microstrips on quartz at 200 GHz, obtained in similar fashion to those in section 7.1.1, are shown in Table 7.5:

Quartz Thickness (μm)	Width (μm)	Impedance (Ω)	Eff. Dielectric constant
40	50	142.3	1.64
40	100	113.7	1.55
40	150	96.7	1.5
40	200	84.8	1.46

Table 7.5 Parameters of suspended microstrips on quartz substrate at 200 GHz.

The microstrip-waveguide transmission modelling resulted in a maximum power coupling for 100 μm microstrip at a back short position 5.8mm. The S_{12} parameters obtained are shown in Figure 7.9:

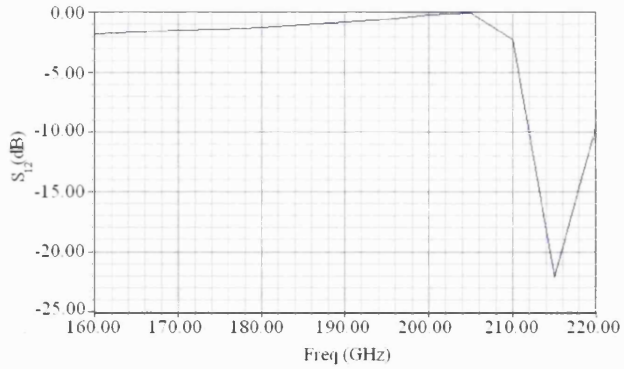

Figure 7.9 S_{12} parameters for the microstrip-waveguide transition for the optimum back short position.

HFSS modelling showed that a 5-element hammerhead filter, as shown in Figure 7.10, has the minimum number of elements for effective blocking of 200 GHz. The initial values for the dimensions are shown in Table 7.6:

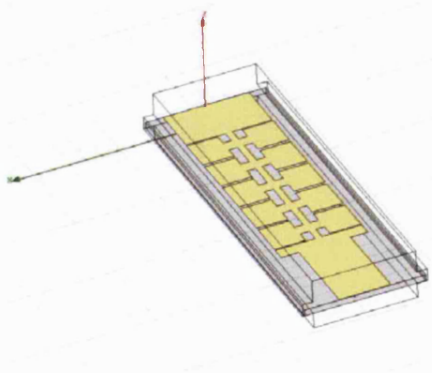

Figure 7.10 Schematic of a 5-element filter for blocking 200 GHz.

L=200	L2=20	L3=70	L4=10	L5=75	L6=290
WW=500	WW2=300	WN=40	WC=50	WP=180	

Table 7.6 Initial modelling dimensions for 5-element hammerhead filter (all dimensions expressed in μm)

In a similar way to that described in the previous section, a sweep of the dimension L was modelled for evaluating the stop band of the filter, the results being shown in Figure 7.11:

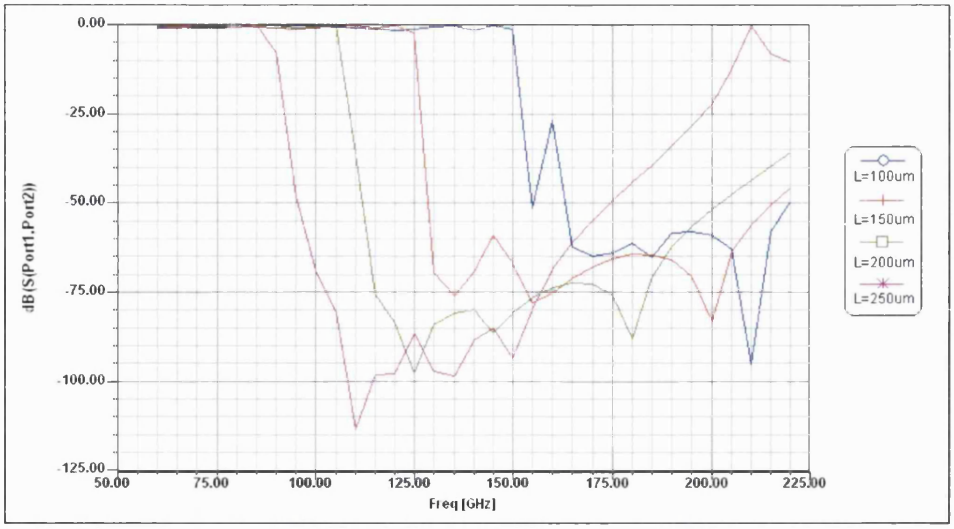

Figure 7.11 S_{12} Parameters of the 5-element hammerhead filter for a sweep of the L dimension.

As the initial dimensions for the 5-element hammerhead filter (L=200 μm) were found to block effectively the desired central frequency (200 GHz) as well as a wide bandwidth, such dimensions were the chosen ones for the actual design of the prototypes.

7.2 Fabrication of non monolithic prototypes

7.2.1 Fabrication of quartz filters and microstrips

The fabrication process developed for the production of quartz filters and microstrips on a 40 μm thick quartz chip is shown in Table 7.7:

Step	Process
1	Mounting the 12 mm x 12 mm chip on a silica carrier using high temperature wax, acetone spraying
2	Spin, bake and hardening S1813
3	UV frame exposure and development
4	UV Exposure of filters and development
5	Evaporation (30 nm Ti + 400 nm Au) and lift-off
6	Filter separation by mechanical sawing

Table 7.7 Fabrication process of quartz filters and microstrips

7.2.2 Fabrication of individual MSM chips

In this fabrication process 64 MSM chips (each 200 μm x 100 μm) distributed in four quadrants are evaporated on a 1 cm x 1 cm piece of semiconductor wafer. Figure 7.12 shows the main layers of the photolithographic mask designed:

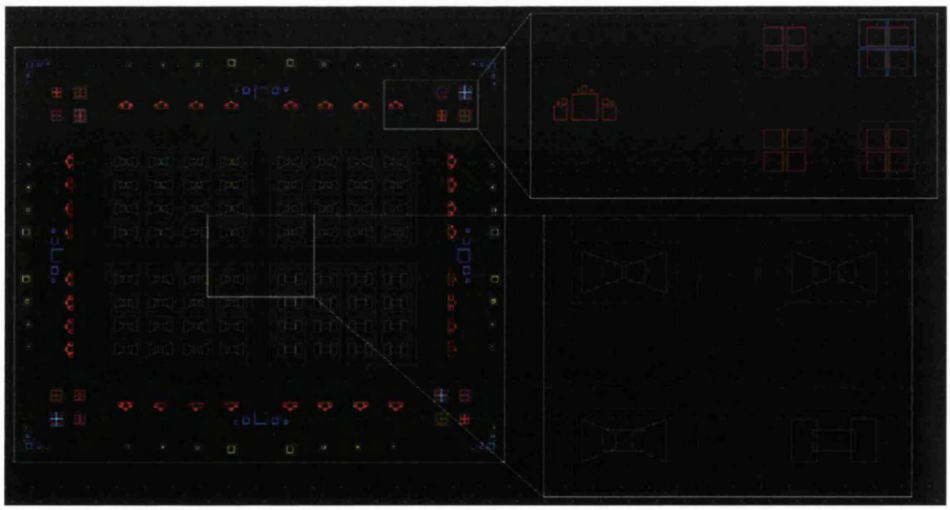

Figure 7.12 Layers in the photolithographic mask for the fabrication of individual MSM chips

The top inset in Figure 7.12 shows the local alignment marks and the alignment marks for accurate positioning of subsequent photolithography steps. The bottom inset shows the different spacings between the contacting pads in the four quadrants for accommodating various sizes of photodetectors.

Step	Process	Layer
1	Cutting chip 10 mm x 10 mm	
2	Silicon dioxide wet etch (HF)	
3	Acetone, IPA and trichloroethane cleaning	
4	Photoresist spin, bake and immersion in Chlorobenzene	
5	Frame exposure and development	Layer 0, white
6	Alignment marks exposure and development	Layer 1, red
7	Metal deposition (20 nm Ti + 250 nm Au) and lift off	
8	Repeat of step 3	
9	PMMA spin and bake	
10	E-beam exposure and development of MSM; note that the exposure is done in four stages (one for each quadrant) with a local alignment step previous to each of them	
11	Metal deposition (20 nm Ti + 180 nm Au) and lift off	
12	Repetition of steps 3, 4 and 5	
13	UV exposure and development of contacting pads	
14	Metal deposition (50 nm Ti + 450 nm Au)	
15a	Deposition of passivation layer of AR passivation coating SiO_2 over the whole chip	
15b	Repetition of steps 3, 4 and 5	
15c	UV exposure and development of windows over contacting pads	
15d	Wet etch of SiO_2 and rinse.	Layer not shown
16	Repetition of steps 3, 4 and 5	
17	Exposure of chip separation grid	Layer 2, purple
18	Wet etch of 30 μm of GaAs and rinse	

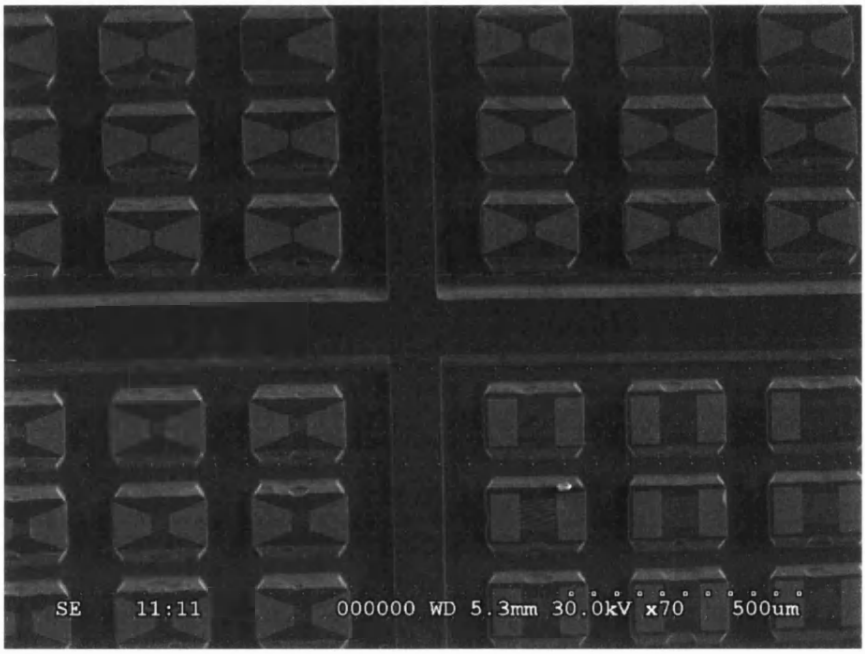

Figure 7.13 Photograph of MSMs chips after fabrication step 18

19	Back side mounting of the chip on a carrier (Silica) using 150°C wax soluble in acetone. Rough horizontal positioning digital caliper.	
20	400 μm GaAs wet Etch.	
21	Fine horizontal correction using Dektak	
22	Mounting of the carrier with the chip on a glass plate with low temperature wax, and horizontal correction with digital caliper.	
23	Mechanically lapping down the back of the chip till the grid is visible.	
24	Immersion in acetone and IPA with filter paper and recovery of devices.	

Table 7.8 Fabrication process of individual MSM chips

Note that the fabrication steps corresponding to the deposition and etch of the antireflection coating (steps 15a - 15d) were included in the fabrication process design and the mask, but were not actually used.

The typical batch fabricated using this fabrication method is shown in Table 7.9:

Quadrant	Number of devices	$(WA)^{1/2}$ (μm)	$(AA)^{1/2}$ (μm)	Finger width (μm)	Finger Spacing (μm)
Top Left	4	10	5	0.25	0.25
Top Left	4	10	5	0.25	0.50
Top Left	4	10	5	0.25	0.75
Top Left	4	10	5	0.25	1.00
Top Right	4	25	10	0.25	0.25
Top Right	4	25	10	0.25	0.50
Top Right	4	25	15	0.25	0.75
Top Right	4	25	15	0.25	1.00
Bottom Left	4	50	25	0.5	0.50
Bottom Left	4	50	25	0.5	0.75
Bottom Left	4	50	35	0.5	1.00
Bottom Left	4	50	35	0.5	1.50
Bottom Right	4	100	50	1	1.00
Bottom Right	4	100	50	1	1.25
Bottom Right	4	100	75	1	1.50
Bottom Right	4	100	75	1	1.75

Table 7.9 Typical individual MSM chip batch fabricated

As can be seen in Table 7.9, each quadrant corresponds to a different working area (WA) in the electron beam as the contacting pads are separated by a fixed distance in each of them. As was noted in Chapter 4, the maximum feature resolution that can be achieved in the electron beam exposure corresponds roughly to one hundredth of the working area. Therefore when exposing fingers in the bottom right quadrant (WA=100 μm x 100 μm) the minimum achievable finger size is 1 μm. As was discussed in Chapters 3 and 5, MSMs fabricated on LTG GaAs should not have finger spacing larger than 0.25 μm so as not to reduce the quantum efficiency. In consequence, only the top quadrants are desirable for the production of MSMs in such material. The motivation for including the bottom quadrants in the fabrication process was the possibility of using the designed mask for fabricating devices in other materials with longer carrier life time that allow high efficiencies for larger spacings.

The main advantage of this fabrication method is the possibility of using it for the fabrication of photomixers in different materials and sizes depending on the frequency response and quantum efficiency required by the particular application. The other advantage is the extremely high yields obtained, consequently saving material and processing time for a large amount of devices. During the course of the research more than 15 chips were successfully fabricated with over 70% of the devices in perfect working order.

7.2.3 Mounting

Once the quartz chip and the individual MSM chips were fabricated the next step is their connection and mounting in the housing block. For performing this fabrication step, a tool consisting of an optical fibre stripped of the cladding and attached to a wooden handle was fashioned for the manipulation of the chips. This step is very delicate as the fingers in the MSM are easily damaged if handled without extreme care. For moving the individual chips, the tip of the fibre was immersed in IPA and brought to contact with the side of the chip under an optical microscope. With the chip stuck to the fibre and the quartz filter under an optical microscope, the photomixer was placed in position. Then the chip was glued to the quartz carrier, and with another manipulation tool, the contacting pads were connected to the microstrip to one side and to the filter to the other, as shown in Figure 7.14. Once this operation was successfully performed, the chip was placed in the groove of the housing and the top and bottom of the chip connected for biasing. Figure 7.15 shows a quartz chip mounted in the housing and connected to the SMA connector. After connection, the housing was closed and the device ready for operation.

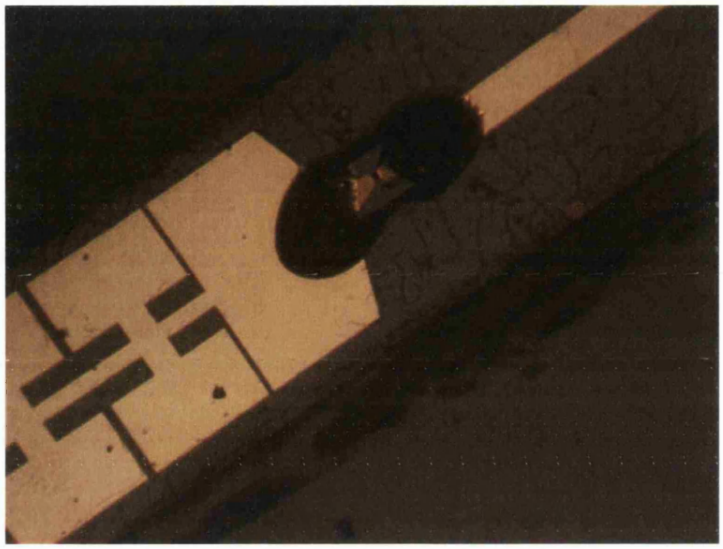

Figure 7.14 MSM chip glued and connected to the quartz filter

Figure 7.15 Chip placed and connected to the housing

An alternative fabrication method for low inductance connection between the GaAs chip and the quartz substrate was designed for ensuring high speed operation. This method relied in the fabrication of individual MSM chips in a perpendicular orientation to those shown in Figure 7.13. When chips are fabricated in such orientation the sides of the chip slope in a roughly 45 degree angle with respect to the quartz substrate that they are fixed to. Then the quartz is mounted on a silicon carrier

using high temperature wax for making it more robust and easier to handle during fabrication. A triple layer (approximately 3 μm thick) of photoresist consisting in bottom layer of LORB and a double layer of S1813 is spun over the whole chip and subsequently baked. A photolithographic step for opening the windows of the low inductance connecting pads is followed by development and evaporation of thick metallizations, Figure 7.16 shows a schematic after this step. The last step is the lift off and the separation of the quartz substrate from the silica carrier.

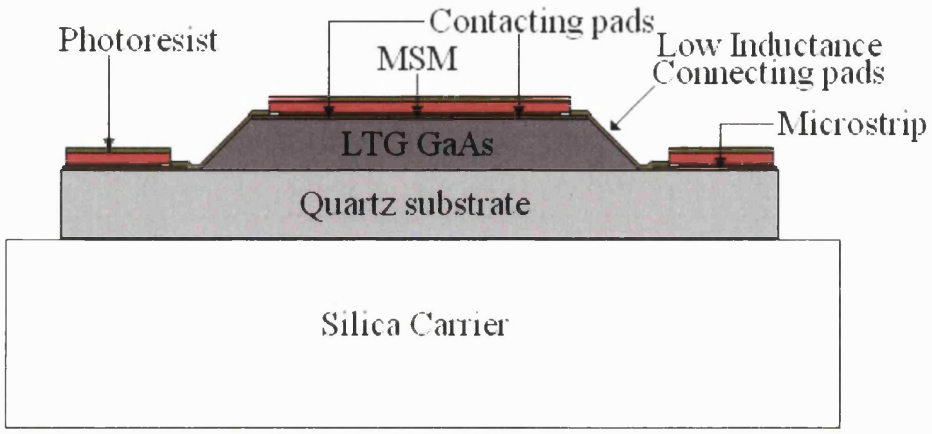

Figure 7.16 Schematic of the alternative low inductance contacting method designed after evaporation step.

7.3 Tests and results

The fabrication process described in the previous section allowed the characterisation of dark current, capacitance and resistance of a high number of MSM photomixers. The photolithographic mask was used for the fabrication of single fingers of different lengths contacted in both pads. The results obtained for the resistance of fingers of different thicknesses and widths were very similar to those shown in Table 5.9.

For these devices, DC tests with the same setup described in Section 5.3 were carried out, some of the results being shown in Table 7.10:

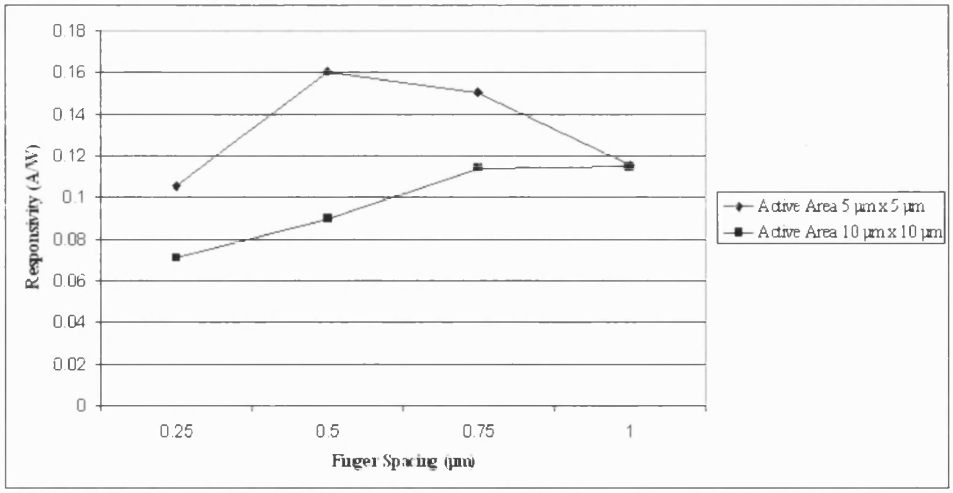

Table 7.10 Responsivity vs. finger spacing for MSMs with finger width 0.25 µm and active areas 5 µm x 5 µm and 10 µm x 10 µm

The dark current of these devices are of the order of tens of nanoamperes. Linear dependence of the photocurrent with optical power was consistently observed for these small devices as it was shown for bigger devices in Section 5.3. Characterisation of the capacitance was also carried out, but in the case of devices of active area 5 µm x 5 µm it is dominated by the capacitance between pads (C_{PP}=8 fF).

It was not possible to experimentally characterize the mixing properties of the 100 GHz and 200 GHz prototypes fabricated due the unavailability of necessary laser sources and optics.

References:

[1] Suspended microstrip calculator:
http://www1.sphere.ne.jp/i-lab/ilab/tool/sus_ms_e.htm

[2] Unpublished project by THz Research Group

Chapter 8

Membrane Supported and Thin-Film MSMs

This chapter covers the design, modelling, fabrication and testing of the membrane supported devices carried out in the David Bullett Nanofabrication Laboratory and the Terahertz Technology Laboratory at the University of Bath.

8.1 Design

To our knowledge, Lee et al [1] were the first to report the fabrication of an MSM on a membrane. Their design, see Figure 7.1, consisted in a 5 μm thick back textured membrane formed by reactive ion etching on a silicon substrate.

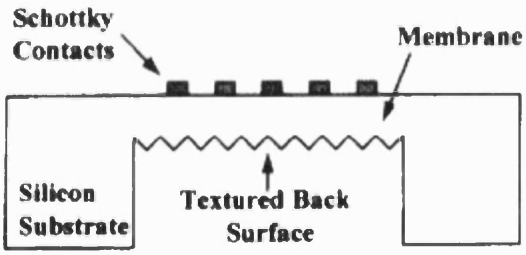

Figure 8.1 Membrane supported MSM reported by Lee *et al.* [1]

The main motivation for this design was the reduction of the long transit times due to the weak optical absorption of silicon. The texturing intended to achieve light trapping to counterbalance the reduction in quantum efficiency due to the low absorption in the thin membrane. The FWHM of the output pulse was reported to be 267 ps for a device prior to membrane formation, and 74 ps after membrane formation.

The fabrication of MSM on thin films provides further advantages. Firstly, it reduces the capacitance of the device, therefore improving the pulse response for RC limited devices [2]. Secondly it provides the possibility of back illumination by avoiding shadowing effects, therefore enhancing the quantum efficiency [3].

This advantageous design has motivated other workers to fabricate non-monolithic MSMs on thin membranes of GaAs [4], GaN [5] and InGaAs [6] among others.

8.2 Fabrication

The fabrication process for individual MSM chips described in the previous chapter was designed to allow the fabrication of both membrane supported (similar design to that shown in Figure 8.1) and thin film inverted MSMs (where individual MSM chips are 1 μm thick). Both designs, given the RC limited nature of the LTG-GaAs, improve the pulse response of the devices through a reduction in capacitance.

As noted in Section 5.1 the epilayered structure was an undoped LTG GaAs active layer 1 μm thick over a half a micron layer of AlGaAs grown over 400 μm layer of bulk GaAs. The role of the AlGaAs layer is to function as an etch stop layer for the thin-film and membrane formation.

The first fifteen steps in the fabrication process for membrane supported MSMs are the same as presented in Table 7.8. The following steps in this process are shown in Figure 8.2. Note that in the figure the thicknesses of the different layers are not to scale and that the anisotropy of the wet etch steps is not represented for clarity. The frame exposed and etched in steps a-c serves for the back-side alignment of the membranes with respect to each individual chip. In spite of the fabrication process being successfully completed using wet etching, the use of dry etching is recommended for the frame, as vertical walls ensure a more accurate alignment. The flip-chip step is achieved by using high temperature wax, the carrier being a silicon chip. In such a step, it is critical for the successful completion of the process that the GaAs chip and the carrier chip are as parallel as possible. In order to ensure that, a digital caliper was employed. In step l, the etchant used is a Citric Acid solution (see Table 4.2). Our tests showed that such solution provides a selectivity in etch rate between GaAs and AlGaAs of approximately 83:1. Such high selectivity prevents the active epilayer of LTG-GaAs from being damaged during the time taken for the separation trenches to be totally opened. The last step of chip separation consists of an immersion in acetone and IPA.

Note that the Dektak was used during this process for the monitoring the depths of the etched trenches.

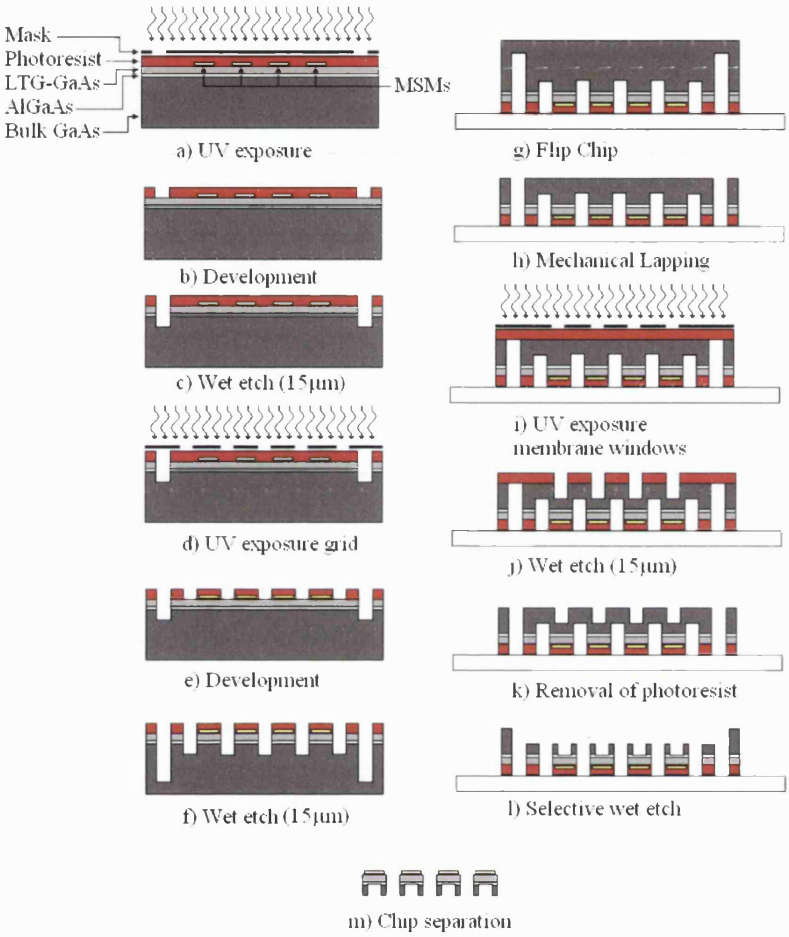

Figure 8.2 Fabrication steps for membrane supported MSMs

The first fifteen fabrication steps of thin-film MSM are the same as those presented in Table 7.8. The following steps consist of spinning and baking of photoresist and UV exposure of the separation grid followed by a wet etch step for opening trenches 2μm deep. Then the chip is flipped and mounted on a silica carrier for mechanical lapping. After the removal of most of the material (until the film is approximately 20 μm), the last step is a selective wet etch for reducing the thickness of the film to

1 μm. Finally immersion in acetone and IPA is performed for separation of individual thin-film chips.

Figure 8.3 shows a membrane supported MSM chip mounted and connected for back illumination.

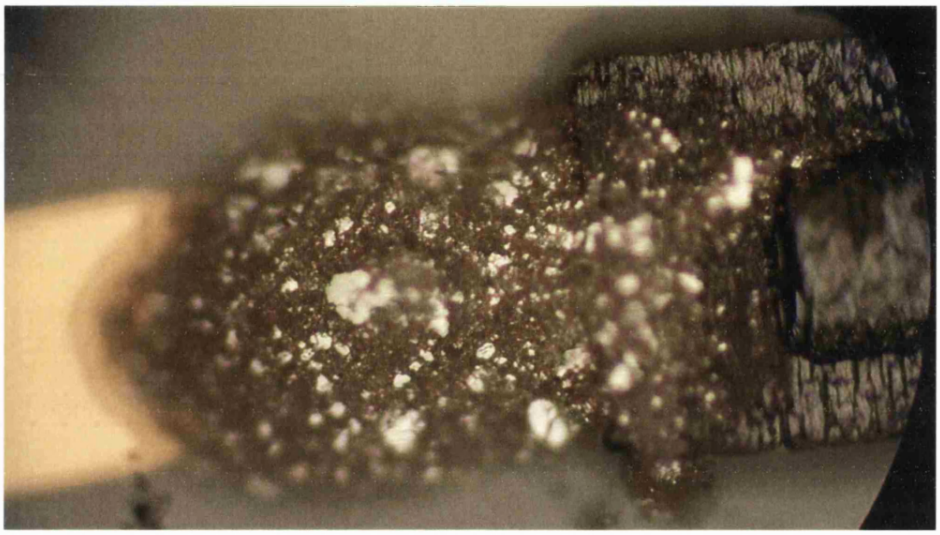

Figure 8.3 Detail of mounted membrane-supported MSM for back illumination

7.3 Test and Results

The dark current, responsivity and linear response with optical power of both thin-film and membrane supported MSM were characterised in the setup described in previous chapters. The results obtained were very similar to those obtained for conventional MSMs. The predicted increase in quantum efficiency could not be correlated with the data presented in previous sections due to the unknown size of the beam diameter.

Measurements of the capacitance for MSMs on 5 μm and 1 μm thick membranes are presented in Table 8.1.

Aperture (μm)	Finger Width (μm)	Finger Spacing (μm)	Cap. with substrate (fF)	Cap. 5μm membrane (fF)	Cap. 1μm membrane (fF)
75	1	2	92	81	63
75	1	3	61	48	39
75	1	4	47	36	27

Table 8.1 Capacitance measurements for membrane supported MSMs

The reduction in capacitance demonstrated for thin-film MSMs in LTG-GaAs allows the fabrication of devices of larger active areas without incurring a reduction of the instantaneous bandwidth.

References:

[1] H. C. Lee, B. Van Zeghbroeck, "A Novel high-speed Silicon MSM Photodetector operating at 830nm wavelength", IEEE Electron Device Letters, 16(5): 175-177, 1995

[2] F. Hieronymi, E. H. Bottcher, E. Drogue, D. Kuhl, S. Kollakowski and D. Bimberg, "Large-area low-capacitance InP/InGaAs MSM photodetectors for high speed operation under front and rear illumination", Electron letters, vol. 30, pp:1247-1248, 1994

[3] M.C. Hargis, S.E. Ralph, J. Woodall, A.J.Negri and P.O. Haugsjaa, "Temporal and Spectral characteristics of back illuminated InGaAs MSM photodetectors", IEEE Photonics technology letters, 8(1):110-112, 1996

[4] O. Vendier, N.M. Jokerst, R.P. Leavitt, "Thin-film inverted MSM photodetectors", IEEE Photonics Technology Letters, 8(2):266-268, 1996

[5] S.W. Seo, K.K. Lee, S. Kang,, S. Huang, W.A. Doolittle, N. M. Jokerst, A. S. Brown and M. A. Brooke, "The heterogeneous integration of GaN Thin-Film Metal-Semiconductor-Metal photodetectors onto silicon", IEEE Photonics Technology Letters, 14(2):185-187, 2002

[6] S.W. Seo, S.Y. Cho, S.Huang, J.J. Shin, N.M. Jokerst, A. S. Brown and M. A. Brooke, "High-speed Large-Area inverted InGaAs thin film MSM photodetectors", IEEE Journal of selected topics in Quantum Electronics, 10(4): 686-693, 2004

Chapter 9

Conclusions

CRESR is an optical spectroscopy technique that relies on an optical heterodyne detection system for the accurate estimation of the gyro-magnetic ratios of semiconductor and biological samples. As was demonstrated in Chapter 2, the use of higher frequencies leads to an enhancement in the resolution of the system. Due to the unavailability of commercial photodetectors at frequencies higher than 50 GHz, the aim of this project was to develop detectors for operation up to 200 GHz.

In this thesis the successful development of various families of MSM photomixers has been presented. Modelling for the estimation of the optimum dimensions of different MSMs for operation at frequencies up to 50 GHz was performed. Various fabrication processes were developed and optimised for improving the yield and the repeatability of the method, as well as reducing dramatically the amount of material required (and therefore the cost). Such prototypes were successfully used for the determination of the g-factors of a diluted ruby sample in the CRESR spectroscopy experiment.

Monolithic and non-monolithic prototypes for operation at 100 GHz and 200 GHz were modelled and fabrication processes successfully developed. It was not possible to use such prototypes in the CRESR system as it was not upgraded for operating at such frequencies due to funding shortage of the project. Two different lines of research for the optimisation of devices were presented: membrane-supported / thin-film device structures and buried metallic contacts. The advantages of membrane devices are lower capacitance and the possibility of back illumination (improvement of external quantum efficiency by avoiding shadowing effects). The buried contacts reduce the spread in the travelling distance of carriers generated at different depths and improve the quantum efficiency allowing collection of carriers generated deeper in the semiconductor. As it was demonstrated, such improvements are achieved without incurring a degradation of the dark current and the capacitance of the devices.

As a result of the research carried out, a concept prototype has been envisaged and it is proposed as subject for future work. The comparison of the estimated parameters for a conventional planar MSM, circular-aperture AR-coated MSM and circular-aperture buried-contacts membrane-supported AR-coated MSM is shown in Figure 9.1 and Table 9.1.

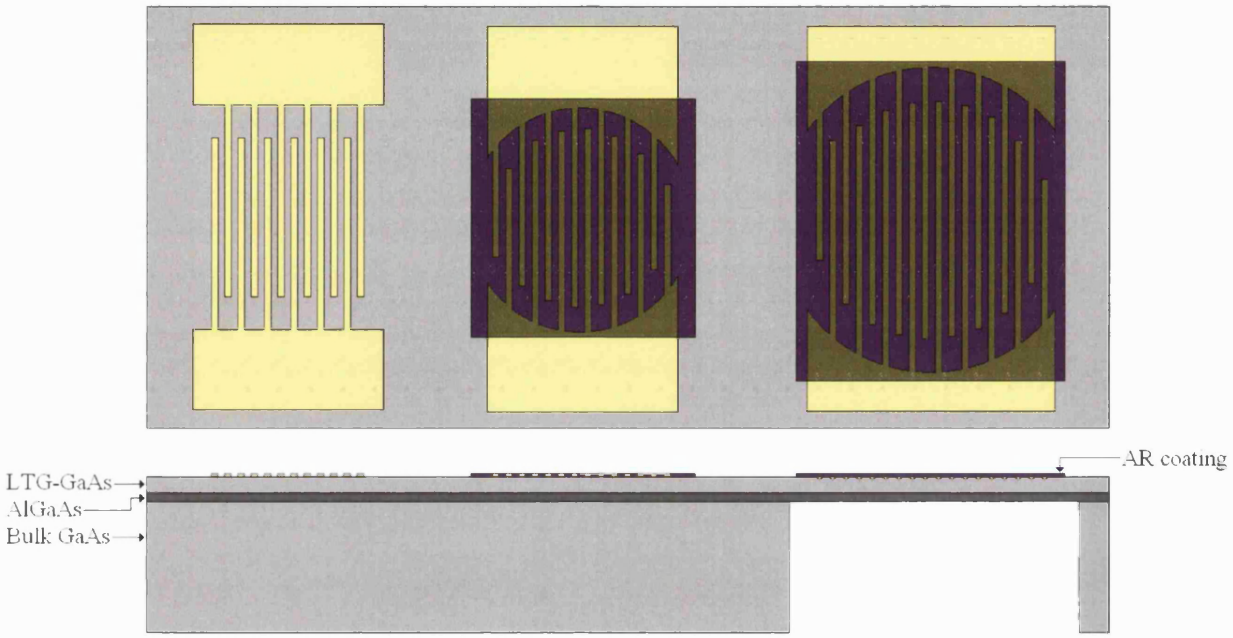

Figure 9.1 Schematic of a) Conventional MSM b) Circular-aperture AR-coated MSM c) Circular-aperture buried-contacts membrane-supported AR-coated MSM

	Normal MSM	Circular MSM	Concept MSM
Dimensions	w=s= 0.4 μm	w=s= 0.4 μm	w=s= 0.4 μm
Active Area	100 μm^2	100 μm^2	166 μm^2
Capacitance	8fF	8fF	8fF
Cap./Area	0.08 fF/ μm^2	0.08 fF/ μm^2	0.048 fF/ μm^2
Quantum eff.	0.08	0.1	0.22

Table 9.1 Parameter comparison for the three devices in Figure 9.1

As was described in Chapter 5 devices in LTG-GaAs are RC limited devices due to the sub-picosecond carrier recombination time. In the comparison, the three devices have the same capacitance and therefore identical instantaneous bandwidth (up to 600 GHz for 8 fF devices). The use of circular aperture reduces the capacitance for a given aperture due to the reduction in the effective capacitive area of the device (approximately 20% reduction). The main advantage of the circular shape with respect to the conventional MSM is that the active area accommodates better the circular shapes of the laser beams. The difference in the estimation of the quantum efficiency for such devices (calculated for wavelength 750 nm) is due to the reduction in Fresnel reflectivity incurred by the antireflection coating. The smaller value of capacitance per unit area of the Circular-aperture buried-contacts membrane-supported device allows a larger active area for the same instantaneous bandwidth.

The thin-film MSM discussed in the previous chapter benefits from the reduction in capacitance, as the membrane-supported device. A potential problem for both types of device is the low thermal conductivity of LTG GaAs that leads to thermal failure under high levels of illumination. Thin-Film MSM can avoid this problem by being mounted on a foreign substrate with better thermal conductivity. Crystalline quartz is a good candidate as a foreign substrate as it has better thermal conductivity (1.4 W/cm°C) and lower relative permittivity (4.4) than GaAs. Therefore, the presence of such substrate would increase slightly the capacitance but with the added advantage of the device being able to cope with higher optical powers.

In the case of thin-film devices mounted for back illumination, crystalline quartz and diamond are adequate candidates as a foreign substrate. An important consideration in this case is that due to the avoidance of the shadowing effects the finger width can be larger than the spacing. This is desirable as the buried contacts should be as close to the back of the membrane as possible in order to avoid carriers generated close to the back surface to recombine before collection. Therefore, due to the anisotropic wet etching, the fingers should be approximately 0.75 μm wide for achieving an approximate depth of 0.75 μm.

Appendix I

Bibliography

Chapter 2

Section 2.1:

Wenckerbach W.T. "Essentials of semiconductor Physics", Wiley (1999)

Holger T.G. "Introduction to Semiconductor Physics", World Scientific Publishing Company (1999)

Seeger K. "Semiconductor Physics: An introduction (Advanced Texts in Physics)", Springer (2004)

Section 2.2:

Singh J. "Optoelectronics, an introduction to materials and devices", McGraw-Hill (1996)

Singh J. "Semiconductor optoelectronics: Physics and technology" McGraw-Hill (1995)

Rieke G.H. "Detection of light: from ultraviolet to the submillimeter", Cambridge University Press (1994)

Rogers A. "Essential of optoelectronics with Applications", Chapman & Hall (1997)

Sze S.M. "Semiconductor devices, Physics and technology, 2nd edition", Wiley (2002)

Yariv A. "Optical electronics, 3rd edition" Holt-Saunders International editions (1995)

Wilson J., Hawkes J.F.B. "Optoelectronics: an introduction", Prentice Hall (1983)

Sharma B.L "Metal-Semiconductor Schottky barrier junctions and their applications", Plenum Press (1984)

Section 2.3

D.M Pozar, "Microwave engineering", John Wiley & Sons, (1998)

S. Maas "Microwave mixers", Artech House Publishers, (1993)

Chapter 4

G.S. May and S.M.Sze, "Fundamentals of semiconductor fabrication", Wiley and Sons, 2003

Hwaiyu Geng "Semiconductor Manufacturing Handbook", McGraw-Hill Handbooks, 2005

P. Van Zant "Microchip Fabrication: A Practical Guide to Semiconductor Processing", McGraw-Hill, 2004

M.S. Shur and M.E Levinshtein "Semiconductor Technology: Processing Fabrication Techniques" ,Wiley and Sons,1997

S.A. Campbell and H.J.Lewerenz "Semiconductor Micromachining: Fundamentals and Technology- Techniques and Industrial Applications", Wiley and Sons, 1998

A.G.Baca and C.I.H.Ashby "Fabrication of GaAs devices" IEE, EMIS Processing Series, 2005

P.Rai-Choudhury "Handbook of Microlithography, micromachining and micro fabrication", 2 vols SPIE Press (1997)

D.A. Neamen "Semiconductor Physics and Devices, Basic Principles", McGraw-Hill, 3rd Edition, (2003)

Elphy Plus, Advanced SEM/FIB Nanolithography System, Users Manual

Appendix II

The photographs presented in this section show a side of the research that was not apparent in the previous chapters of the thesis. During research to find out that something does not work is as valuable as finding out the things that do work.

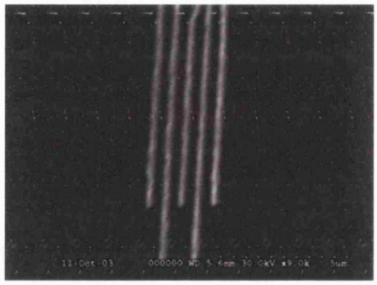

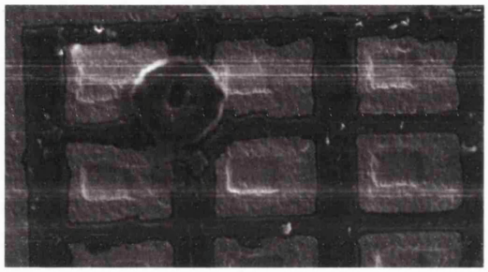

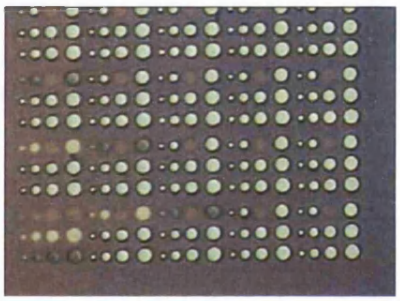

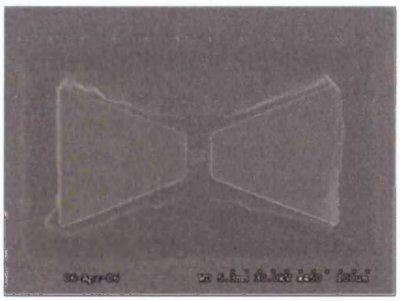

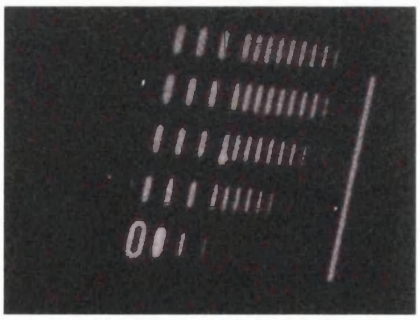

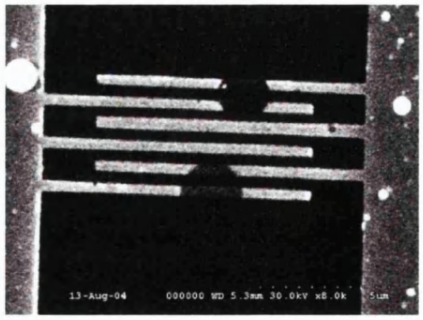

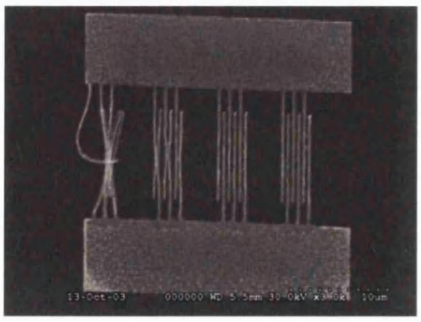

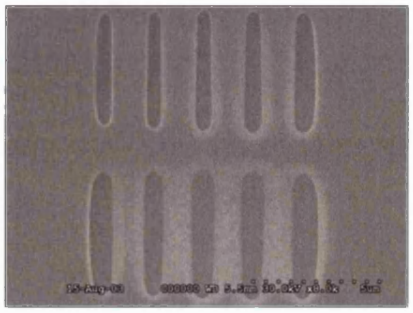

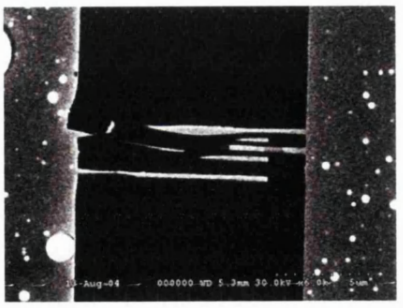

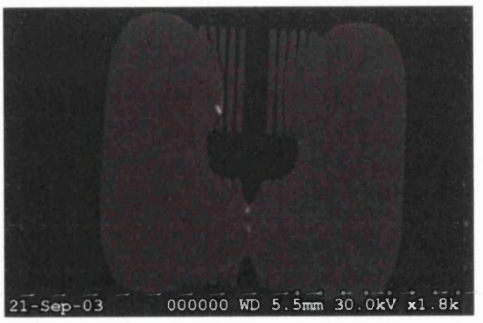
21-Sep-03 000000 WD 5.5mm 30.0kV x1.8k

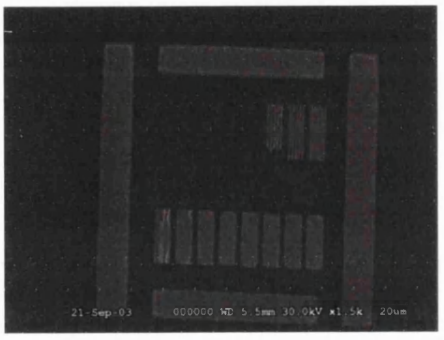
21-Sep-03 000000 WD 5.5mm 30.0kV x1.5k 20um

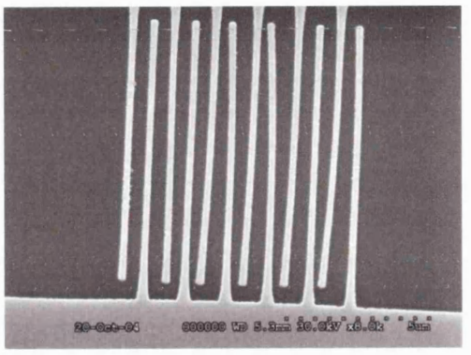

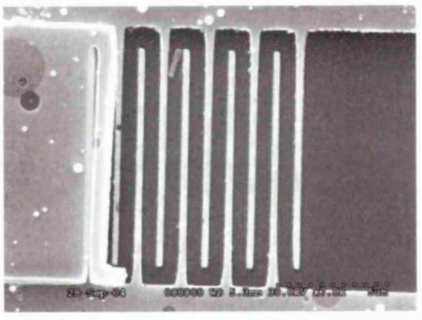

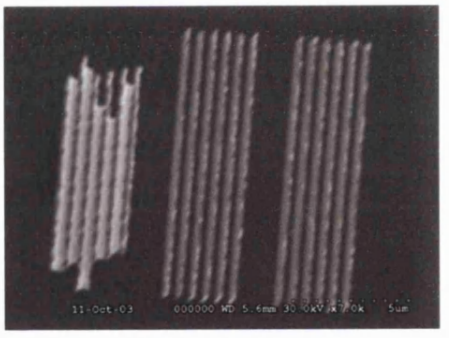
11-Oct-03 000000 WD 5.6mm 30.0kV x70k 5um

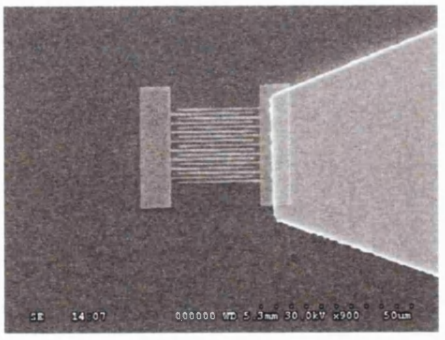
SE 14.07 000000 WD 5.3mm 30.0kV x900 50um

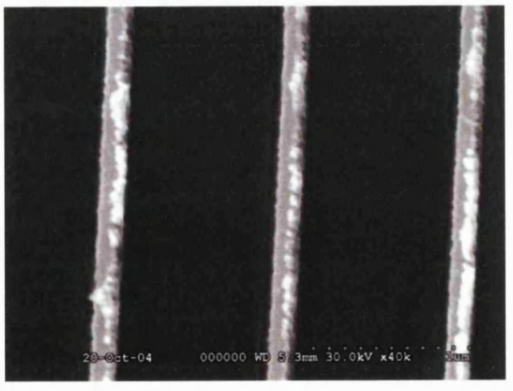
20-Oct-04 000000 WD 5.3mm 30.0kV x40k

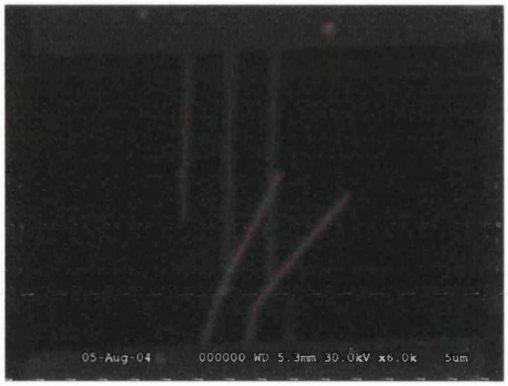
05-Aug-04 000000 WD 5.3mm 30.0kV x6.0k 5um

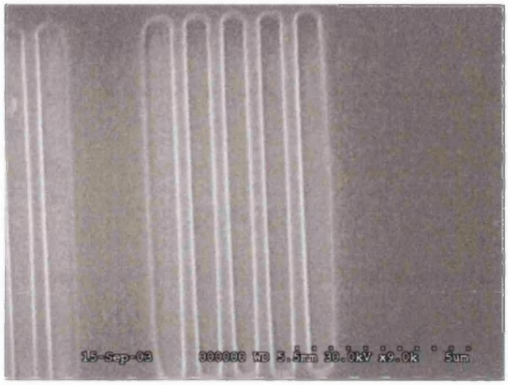
15-Sep-03

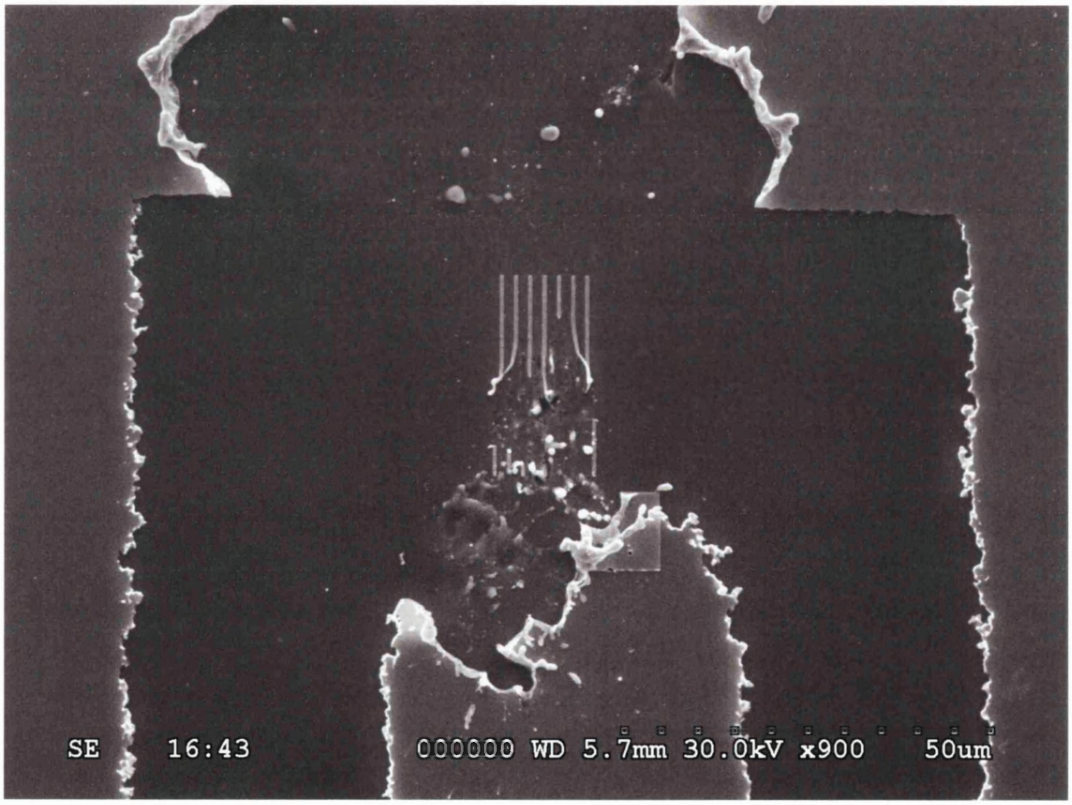
SE 16:43 000000 WD 5.7mm 30.0kV x900 50um